Copyright
by
Athena Ranice Stacy
2011

The Dissertation Committee for Athena Ranice Stacy
certifies that this is the approved version of the following dissertation:

New Insights into Primordial Star Formation

Committee:

Volker Bromm, Supervisor

Harriet Dinerstein

Neal J. Evans II

Milos Milosavljevic

J. Craig Wheeler

Abraham Loeb

New Insights into Primordial Star Formation

by

Athena Ranice Stacy, B.S.; M.A.

DISSERTATION

Presented to the Faculty of the Graduate School of
The University of Texas at Austin
in Partial Fulfillment
of the Requirements
for the Degree of

DOCTOR OF PHILOSOPHY

THE UNIVERSITY OF TEXAS AT AUSTIN
August 2011

Dedicated to my parents, Dr. J.W. and Nan Stacy.

New Insights into Primordial Star Formation

Publication No. ____________________

Athena Ranice Stacy, Ph.D.
The University of Texas at Austin, 2011

Supervisor: Volker Bromm

The formation of the first stars, also known as Population III (Pop III), marked a pivotal point in the universe's evolution from relative smoothness and homogeneity to its current highly structured state. In this dissertation we study key aspects of Pop III star formation. We utilize three-dimensional cosmological simulations to follow the evolution of gas and DM from $z \sim 100$ until the first minihalo forms. Once the gas infalls toward the center of the minihalo and condenses, we implement the 'sink particle' method to represent regions that will form a star, and we follow the evolution of the metal-free, star-forming gas for many free-fall times. A disk forms around the initial Pop III star and fragments to form secondary stars with a range of masses (1 - 50 $M_{\odot}$). This is markedly different from the previous paradigm of one single, massive star forming per minihalo. Using a ray-tracing technique, we also examine the effect of radiative feedback on protostellar growth and disk fragmentation. This feedback will not prevent the formation of secondary stars within the disk, but will reduce the final mass reached by the largest Pop III star. Measuring the angular momentum of the gas that falls onto the sink regions, we also find that the more massive Pop III stars accrete sufficient angular momentum to rotate at nearly break-up speeds, and can potentially end their lives as collapsar gamma-ray bursts or hypernovae. We furthermore numerically examine the recently discovered relative streaming motions between dark matter and baryons, originating from the era of recombination. Relative streaming will slightly delay the redshift at which Pop III stars first form, but will otherwise have little impact on Pop III star formation and the history of reionization. We finally evaluate the possible effect of a cosmic ray (CR) background generated by the supernova deaths of massive Pop III stars. A sufficiently large CR background could indirectly enhance the H_2 cooling within the affected minihalos. The resulting lower temperatures would lead to a reduced characteristic stellar mass ($\sim 10\,\mathrm{M}_{\odot}$), providing another possible pathway to form low-mass Pop III stars.

Table of Contents

Abstract **v**

List of Tables **xi**

List of Figures **xii**

Chapter 1. Introduction **1**

1.1 Motivation 1

1.2 Relation to Previous Work 3

1.3 Outline 5

Chapter 2. Formation of Binaries and Small Multiple Systems[1] **8**

2.1 Overview 8

2.2 Physical Ingredients 11

2.2.1 Protostellar accretion 11

2.2.2 Protostellar feedback effects 12

2.2.3 Chemistry, heating and cooling 14

2.3 Numerical Methodology 15

2.3.1 Initial setup 15

2.3.2 Sink particle creation 17

2.4 Results 21

2.4.1 Initial runaway collapse 21

2.4.2 Protostellar accretion 25

2.4.2.1 Disk formation 25

2.4.2.2 Angular momentum evolution 32

---

[1] This chapter has been published as Stacy A., Greif T. H., Bromm V., 2010, MNRAS, 403, 45

2.4.2.3 Binary and multiple formation 34
2.4.2.4 Accretion rate 36
2.4.2.5 Thermodynamics of accretion flow 39
2.4.2.6 Feedback 42
2.5 Parameter Sensitivity 46
2.6 Summary and Discussion 48

Chapter 3. The First Stars: Mass Growth Under Protostellar Feedback 54
3.1 Introduction 54
3.2 Numerical Methodology 57
3.2.1 Initial Setup 57
3.2.2 Chemistry, Heating, and Cooling 58
3.2.3 Sink Particle Method 59
3.2.4 Ray-tracing Scheme 61
3.2.5 Photoionization and Heating 63
3.2.6 Protostellar evolution model 64
3.3 Results 70
3.3.1 Disk Evolution 70
3.3.1.1 No-feedback case 70
3.3.1.2 With-feedback case 76
3.3.2 Fragmentation 77
3.3.3 Ionization Front Evolution 82
3.3.4 Protostellar Mass Growth 86
3.4 Summary and Discussion 89

Chapter 4. Rotation speed of the first stars[2] 94
4.1 Overview 94
4.2 Numerical Methodology 98
4.2.1 Initial Setup 98

---

[2] This chapter has been published as Stacy A., Bromm V., Loeb A., 2011, MNRAS, 413, 543

4.2.2 Chemistry, heating, and cooling 100
4.2.3 Sink Particle Method 100
4.3 Results 102
4.3.1 Sink Growth and Angular Momentum 102
4.3.1.1 Accretion Rate 102
4.3.1.2 Angular Momentum 104
4.3.2 Stellar Rotational Velocity 106
4.3.2.1 Thin Accretion Disk 106
4.3.2.2 Extrapolation to Stellar Surface 113
4.4 Implications of Rapid Rotation 119
4.4.1 Rotational Mixing 119
4.4.2 GRBs and Hypernovae 121
4.5 Sub-Sink Fragmentation 123
4.6 Summary and Discussion 126

Chapter 5. Effect of Streaming Motion of Baryons Relative to Dark Matter on the Formation of the First Stars[3] 130
5.1 Overview 130
5.2 Numerical Methodology 132
5.3 Results 133
5.3.1 Delay of Gas Collapse 133
5.3.2 Thermal Evolution and Star Formation 139
5.4 Summary and Discussion 142

Chapter 6. Impact of Cosmic Rays on Population III Star Formation[4] 144
6.1 Overview 144
6.2 Cosmic rays in the high-z Universe 145
6.2.1 Population III star formation 145
6.2.2 Cosmic ray production 147
6.2.3 High-redshift GZK cutoff 151

---

[3] This chapter has been published as Stacy A., Bromm V., Loeb A., 2011, ApJ, 730, L1

[4] This chapter has been published as Stacy A. & Bromm V., 2007, MNRAS, 382, 229

6.2.4 Magnetic fields 153
6.3 Evolution of Primordial Clouds 156
6.3.1 Idealized models 156
6.3.2 Thermal and chemical evolution 158
6.3.3 Local CR Feedback 168
6.3.4 Dependence on minimum CR energy 171
6.3.5 Fragmentation scale 173
6.4 Summary and Discussion 175

Chapter 7. Outlook **177**

Vita **208**

List of Tables

2.1 Formation times, final masses, and locations of the sinks. . . . 35

3.1 Formation times, final masses, and locations of sinks in 'no-feedback' case. . . . 80

3.2 Same as Table 3.1, but for sinks remaining at the end of the 'with-feedback' case. . . . 80

4.1 Final sink angular momenta, stellar masses, and stellar rotational velocities. . . . 119

List of Figures

2.1 Density projection of gas on various scales. 20
2.2 Physical state of the collapsing core just prior to sink formation. 23
2.3 Radial structure of gas just prior to sink formation. 24
2.4 Kinematics of gas around the main sink particle. 26
2.5 Density and temperature projections of the star-forming disk. 28
2.6 Velocity field of the central gas distribution. 29
2.7 Disk mass versus time. 31
2.8 Angular momentum structure of star-forming gas. 33
2.9 Sink mass and accretion rate versus time. 38
2.10 Evolution of gas thermodynamic properties. 40
2.11 Dominant cooling processes in the center of the minihalo. . . . 42
2.12 Impact of feedback on the accretion process. 45
2.13 Specific angular momentum profiles of gas for various cosmological simulations. 47

3.1 Evolution of various properties of the growing protostar according to our analytical model. 65
3.2 Evolution of various disk properties. 71
3.3 Evolution of disk mass over time. 73
3.4 Temperature versus number density for both cases at various times in the simulations. 75
3.5 Projected density and temperature structure of central 10,000 AU without protostellar feedback. 78
3.6 Projected density and temperature structure of gas under LW and ionization feedback. 79
3.7 Projected ionization structure of gas at 1700, 2300, and 4200 yr after initial sink formation. 82
3.8 Evolution of various H II region properties over time. 85
3.9 Effect of radiative feedback on protostellar accretion. 88

4.1 Growth of sink mass and rotational support over time. 104
4.2 Growth of sink angular momentum and rotational velocity over time. 107
4.3 Relative energy composition of sink-accreted particles 110
4.4 Torque acting within the stellar disk. 112
4.5 Cooling and angular angular momentum loss timesscale of gas surrounding the sinks. 114
4.6 Evolution of stellar rotational velocities. 117
4.7 Angular momentum versus distance from center of the stars. . 120

5.1 Redshift evolution of the minihalo and streaming gas. 135
5.2 Effect of relative streaming on redshift of primordial gas collapse. 137
5.3 Effect of relative streaming on evolution of gas temperature with density. 140
5.4 Effect of relative streaming on evolution of gas properties with halo mass. 141

6.1 Penetration depth as a function of cosmic ray energy. 160
6.2 Thermal evolution of primordial gas clouds at $z = 20$. 163
6.3 Minimum temperature reached by the minihalo gas versus cosmic ray energy density and spectral slope. 165
6.4 Thermal evolution of primordial gas clouds at $z = 15$. 167
6.5 Thermal evolution of primordial gas in a minihalo at various distances from a pair-instability supernova. 170
6.6 Bonnor-Ebert mass of gas within minihalos at $z = 20$. 174

Chapter 1

Introduction

1.1 Motivation

The last century has seen great strides in our understanding of the history of the universe. From Edwin Hubble's 1929 discovery that galaxies are receding from us (Hubble 1929), to Penzias and Wilson's initial detection of the Cosmic Microwave Background (CMB; Penzias and Wilson 1965; Dicke et al. 1965), much evidence has led us to believe that the universe began $\sim$ 14 billion years ago in a Big Bang and has been expanding ever since. Observations have also revealed that we likely live in a Λ Cold Dark Matter (ΛCDM) universe, where the majority of the universe's mass is composed of invisible dark matter (DM) instead of the baryonic matter with which we are familiar. Even more recently, we have found that matter itself is only a small portion of the total energy content of the universe, which is mostly comprised of a mysterious Dark Energy.

The universe we observe today bears little resemblance to the universe in its initial stages - stars, planets, and galaxies did not arise until long after the Big Bang. How was the homogeneous early universe transformed into the highly complex state that we observe today? One of the keys is to understand the formation and properties of the first stars, the so-called Population III (or Pop III), since they likely played a crucial role in driving early cosmic evolution (e.g. Barkana and Loeb 2001; Bromm and Larson 2004; Ciardi and Ferrara

2005; Glover 2005; Bromm et al. 2009; Loeb 2010).

After the emission of the CMB at $z \sim 1000$, the universe entered the 'Dark Ages,' the period when the distribution of matter was very uniform and no luminous objects had yet formed. During this time, cold dark matter (CDM) density perturbations grew and developed into gravitationally bound halos, inside of which the first stars formed at $z \lesssim 50$. These metal-free, Pop III stars are believed to have formed within $M \sim 10^6\,\mathrm{M}_\odot$ minihalos, where the infall of the baryons into the gravitational potential well of the DM-dominated minihalo heated the gas sufficiently to enable H_2-driven cooling and fragmentation (e.g. Haiman et al. 1996; Tegmark et al. 1997; Yoshida et al. 2003). Not only did the radiation from the first stars likely start the process of reionizing the intergalactic medium (IGM; e.g. Kitayama et al. 2004; Sokasian et al. 2004; Whalen et al. 2004; Alvarez et al. 2006; Johnson et al. 2007), but when some of these stars produced supernovae (SNe) explosions, they released the first heavy elements into the IGM, providing its initial metal enrichment before the formation of galaxies in higher-mass DM halos (e.g. Madau et al. 2001; Mori et al. 2002; Bromm et al. 2003; Wada and Venkatesan 2003; Norman et al. 2004; Tornatore et al. 2007; Greif et al. 2007, 2010; Wise and Abel 2008). At the same time, DM halos continued to grow in mass as Pop III stars set the stage for the first galaxies to arise.

The stellar luminosity and ionizing photon production primarily depend on mass, as does the end state of the star. For instance, stars with masses in the range of $40\ \mathrm{M}_\odot < M_* < 140\ \mathrm{M}_\odot$ are expected to collapse directly into black holes, while stars in the mass range of $140\ \mathrm{M}_\odot < M_* < 260\ \mathrm{M}_\odot$ will die as pair-instability supernovae (PISNe; Heger and Woosley 2002). Below $40\ \mathrm{M}_\odot$ but above $\sim 10\ \mathrm{M}_\odot$, stars are again expected to explode as core-collapse SNe, leaving behind a neutron star or black hole. Thus, the masses of the first stars are the main determinant of their cosmological impact, though other factors such as the typical rotation rate and the overall formation rate also play a vital role.

Improving our understanding of the formation of the first stars and their resulting initial mass function (IMF) is thus central to understanding this turning point in the universe and the environment in which the first galaxies formed. Such work is especially important now in order to prepare for upcoming observations of instruments such as the *James Webb Space Telescope* (*JWST*), the *Square Kilometer Array*, and *LISA*, as well as the future ground-based Extremely Large Telescopes such as the *E-ELT*, *GMT*, and *TMT* (e.g. Greif et al. 2009; Johnson et al. 2009). In particular, *JWST* is expected to detect $z \simeq 10$ galaxies and give constraints on the IMF of their constituent stars (Pawlik et al. 2011). It will also be exciting to match predictions from upcoming numerical work with spectroscopic observations of individual stars in nearby ultra-faint dwarfs ('dwarf archaeology'), as these stars may hold the SN abundance signatures of Pop III stars (Frebel and Bromm 2010).

1.2 Relation to Previous Work

Much numerical work has already been carried out in attempting to predict the typical mass of the first stars. The earliest simulations found that Pop III stars were very massive ($\gtrsim 100$ $\mathrm{M}_{\odot}$) due to a lack of metal and dust cooling, and that these stars formed in isolation (e.g. Abel et al. 2002; Bromm et al. 2002). Later simulations confirmed this (e.g. Yoshida et al. 2006). However, while these cosmological simulations could study the initial collapse of primordial gas to very high densities, near the point when a Pop

III protostar was expected to form, they were unable to follow the subsequent mass growth of this initial seed. The numerical study by Bromm and Loeb (2004) was able to follow the evolution of such a region for longer times, and also found that Pop III stars will be single and extremely massive, but this work was not performed on cosmological scales and did not include protostellar feedback. Analytical studies such as those by McKee and Tan (2008) found that feedback would still not prevent Pop III stars from growing to greater than 100 $M_{\odot}$. Nevertheless, further improved simulations, including work described in the following chapters, are now putting this picture of lone, massive Pop III stars into question (e.g. Clark et al. 2008, Clark et al. 2011a, Turk et al. 2009; Stacy et al. 2010; Greif et al. 2011).

Our picture of Pop III star formation continues to evolve, and simulations of Pop III growth that start from cosmological initial conditions are only just beginning to self-consistently include protostellar feedback processes (e.g. Smith et al. 2011). Meanwhile, there have been almost no studies of Pop III rotation. However, with a growing knowledge of Pop III stars, we will soon reach a point where we can answer important questions such as 'How effective is Pop III feedback in suppressing subsequent star formation?' We will also be able to estimate 'How massive were the Pop III.2 stars that formed within the radiation field of the earlier Pop III.1?' Up until now, most simulations of first galaxy formation have simply assumed some stellar mass (e.g., 100 or 200 $M_{\odot}$) inside the high-density region once the gas surpasses the density resolution limit (e.g. Johnson et al. 2007; Greif et al. 2009), but with recent new insights into Pop III star formation, simulations of the first galaxies are set to improve as well. With the ever-increasing power of supercomputers, the gap between theory and observation grows ever smaller, and the following chapters describe studies that have attempted to address this goal.

1.3 Outline

Chapters 2 and 3 comprise the first section of this dissertation. These chapters describe studies which aim to improve upon the ‘standard model’ of Pop III star formation. The standard model is the process of how the first stars are expected to form in a ΛCDM universe, where DM halos grow through hierarchical merging until they are massive enough to gravitationally draw in gas which will form stars. This model excludes any background radiation or metals produced by stars in other minihalos, and thus describes star formation in truly pristine gas. Chapters 2 and 3 utilize cosmological simulations to examine the typical mass reached by Pop III stars within this model. In particular, these chapters describe numerical modeling of the Pop III protostellar accretion process, since it is protostellar accretion, and in particular its termination, that governs the final masses that attained by the first stars.

In **Chapter 2**, we find that a small Pop III multiple system forms within a disk, dominated by a binary of 40 $M_\odot$ and 10 $M_\odot$. This is an important modification to the canonical picture of a single, highly massive star forming per minihalo.

In **Chapter 3**, we study the effect of radiative feedback on the the mass growth of Pop III stars and fragmentation of primordial gas. We find that radiative feedback does not prevent fragmentation, and a massive Pop III binary forms within a disk. The acccretion rate onto the most massive star, however, is significantly reduced, and feedback may sometimes prevent Pop III stars from growing to more than a few tens of solar masses.

Chapter 4 is the next section of this dissertaton. In this chapter we explore, for the first time in a cosmological context, the Pop III stellar rotation rate. Stellar rotation is a key parameter, second only to mass, which is necessary to fully describe Pop III stars. The rotation rate has important implications for the evolution of the star, the fate encountered at the end of its life, and the potential for triggering a gamma-ray burst (GRB). We find that Pop III stars are able to reach rapid rotation rates, and indeed may have resulted in hypernova explosions and GRBs.

Chapters 5 and 6 comprise the final section of the dissertation. This section describe studies of primordial star formation which go beyond the standard model. Therein, we evaluate how previously unconsidered modifications to the standard picture may change the typical mass and redshift of formation of Pop III stars.

In **Chapter 5**, we perform a numerical study of the collapse of primordial gas under modified cosmological initial conditions. In particular, we evaluate how the recently discovered supersonic relative velocity between the baryons and dark matter influences Pop III star formation. This relative velocity has not been included in previous numerical studies, and thus expands upon the usual ΛCDM model used to initialize simulations. We find that the typical streaming velocities will have little effect on the gas evolution and Pop III star formation.

In **Chapter 6**, we add cosmic rays (CRs) as a physical ingredient that affects the thermal and chemical evolution of primordial gas on its way to becoming a Pop III star. CRs are expected to propagate away from SNe much faster than the metals produced at the same site. We show that a CR background could have led to characteristic stellar masses as low as $\sim 10\,\mathrm{M}_{\odot}$.

CRs may therefore provide a pathway for the formation of low-mass, Pop III stars in minihalos.

In **Chapter 7**, we summarize the work described within this dissertation, and give a brief outlook for future studies.

Chapter 2

Formation of Binaries and Small Multiple Systems[1]

2.1 Overview

The extent to which the radiation and metal enrichment from the first stars influenced the early universe is largely determined by their mass. Currently, Pop III stars are believed to have first formed around $z \sim 20$ within minihalos of mass $M \sim 10^6\,\mathrm{M}_\odot$ (e.g. Haiman et al. 1996; Tegmark et al. 1997; Yoshida et al. 2003). The potential wells of these minihalos are provided by dark matter (DM), which serve to initially gather primordial gas into them. This is in contrast to present-day star-forming giant molecular clouds (GMCs), which are of similar mass to minihalos, but which form within much larger galaxies and are not DM dominated. Previous three-dimensional simulations (e.g. Abel et al. 2002; Bromm et al. 2002) have studied the formation of $M \sim 1000\,\mathrm{M}_\odot$ prestellar cores with sizes < 0.5 pc within such minihalos. The density in these cores is similar to those in present-day ones, but having considerably higher temperature ($\sim 200\,\mathrm{K}$ for primordial cores versus $10-15\,\mathrm{K}$ for those within GMCs).

The mass of the first stars depends on the further evolution of such cores. Similar to present-day star formation (e.g. McKee and Tan 2002), it is expected that some of the gas within these cores will gravitationally collapse into one or more protostars of initial mass $\sim 5 \times 10^{-3}$ $M_\odot$ (Omukai and Nishi 1998; Yoshida et al. 2008). A fraction of the core mass will be accreted onto the protostar(s), ultimately forming stars much more massive than the initial seeds. Three-dimensional simulations which studied the growth of a primordial protostar through accretion imply that the first stars were quite massive, finding an upper limit of $\sim 500\,M_\odot$ (Bromm and Loeb 2004). Some of the earliest studies of Pop III star formation, however, predicted that Pop III stellar masses might be quite low, < 1 $M_\odot$ (e.g. Kashlinsky and Rees 1983). These authors emphasized the importance of angular momentum in determining the mass of Pop III stars, predicting that rotational effects would cause the primordial gas clouds to collapse into a dense disk. Only after the disk cooled to $\sim 1000\,$K through H_2 line emission could fragmentation occur. Depending on the spin of the cloud, the fragments thus formed could have had masses as low as $\lesssim 0.2$ $M_\odot$. Later studies by Saigo et al. (2004) also found that high initial angular momentum would allow primordial clouds to form disks, and they further predicted that disk fragmention into binaries would be common. Similar calculations by Machida et al. (2008), which were initialized at much lower densities and therefore at an earlier point in the gas collapse, found fragmentation would occur even for primordial gas clouds with very modest initial angular momentum. Finally, the recent work by Clark et al. (2008) included a simulation of a 500 $M_\odot$ primordial gas cloud which fragmented into ~ 20 stellar objects.

---

[1] This chapter has been published as Stacy A., Greif T. H., Bromm V., 2010, MNRAS, 403, 45

However, none of the above-mentioned investigations were initialized on cosmological scales. Our goal in this study is to further improve our understanding of how a Pop III star is assembled through the process of accretion within the first minihalos. More specifically, we aim to determine the final masses reached by the first stars, and whether the gas within a host minihalo forms a single star or fragments into a binary or small multiple system. To this end we perform a three-dimensional cosmological simulation that follows the formation of a minihalo with very high numerical resolution, allowing us to trace the evolution of its gas up to densities of $10^{12}\,\mathrm{cm}^{-3}$. Unlike the study of Bromm and Loeb (2004), which employed a constrained initialization technique on scales of $\sim 150\,\mathrm{pc}$, our simulation is initialized on cosmological scales. This allows the angular momentum of the minihalo to be found self-consistently, eliminating the need for an assumed spin parameter. In a fashion similar to Bromm and Loeb (2004), we represent high-density peaks that are undergoing gravitational runaway collapse using the sink particle method first introduced by Bate et al. (1995), allowing us to follow the mass flow onto the sinks well beyond the onset of collapse.

The recent simulation by Turk et al. (2009), starting from cosmological initial conditions, has shown fragmentation and the formation of two high-density peaks, which are interpreted as seeds for a Pop III binary. These peaks are similar to the multiple sinks found in our simulation. Although Turk et al. employed even higher numerical resolution, they were able to follow the evolution of the high-density peaks for only $\sim$ 200 yr. Our sink particle method, on the other hand, enabled us to continue our calculation for several thousand years after initial runaway collapse. We could thus follow the subsequent disk evolution and further fragmentation in detail, rendering our study ideally complementary to their work.

The structure of our paper is as follows. In Chapter 2.2, we discuss the basic physical ingredients determining the accretion flow, whereas we describe our numerical methodology in Chapter 2.3. We proceed to present our results in Chapter 2.4, discuss the sensitivity of our results to variation in cosmological parameters (Chapter 2.5), and conclude in Chapter 2.6.

2.2 Physical Ingredients

2.2.1 Protostellar accretion

Unlike the gas from which present-day stars are formed, which can typically cool to ~ 10 K, primordial gas contained no metals and could only cool down to ~ 100 K through H_2 and HD line transitions. These elevated temperatures lead to a higher accretion rate, which can be estimated on dimensional grounds by assuming that the Jeans mass is infalling at the free-fall rate, resulting in

$$\dot{M} \simeq \frac{c_\mathrm{s}^3}{G} \propto T^{3/2} \ , \tag{2.1}$$

where $\mathrm{c_s}$ is the soundspeed. This is quite close to the Shu (1977) similarity solution for collapse of a singular isothermal sphere, which gives $\dot{M} = 0.975 c_\mathrm{s}^3/G$. The Shu solution begins with an isothermal cloud with $\rho \propto r^{-2}$ and initially negligible infall velocities. The solution then describes the subsequent 'inside-out' collapse of the cloud, which physically corresponds to accretion of mass onto the central protostar. The earlier similarity solution of Larson (1969) and Penston (1969) described the collapse of an initially uniform cloud into a peaked structure with an r^{-2} density profile. This solution was later expanded by Hunter (1977) to capture the evolution after the initial formation of a hydrostatic core when it grows via accretion of the envelope. At the point of initial protostar formation, corresponding to when the central density becomes infinite in the similarity solution, the infall velocity is already 3.3 times the sound speed, and the accretion rate grows to 48 times higher than that found in Shu collapse (Hunter 1977).

In our simulation, the collapse of the gas from initially more uniform densities can be expected to behave similarly to a Larson-Penston-type solution (e.g. Omukai and Nishi 1998). The following accretion of this gas onto the central hydrostatic core should proceed from the 'inside-out' at rates similar to those found in the Shu and Larson-Penston-Hunter solutions.

2.2.2 Protostellar feedback effects

As the protostellar mass grows through accretion, feedback from photoionization, heating, and radiation pressure will begin to have important effects on the accretion flow and may set the upper mass limit for both present-day and primordial stars. One important difference between feedback in primordial and present-day massive star formation is due to the existence of dust grains in the latter case. For instance, Ripamonti et al. (2002) found with their one-dimensional calculations that Pop III protostellar radiation pressure will not affect the initial collapse and early stages of accretion due to the low opacity of the infalling gas. In contrast, for present-day star formation the increased opacity from dust enhances the radiation pressure and can halt infall onto stars of more than a few tens of solar masses without further mechanisms to alleviate the radiative force (see summary in McKee and Ostriker 2007). On the other hand, later in the life of a present-day star, dust absorption of ionizing photons will alter the evolution of the H II region around the star, thus reducing the photoionization feedback.

Omukai and Palla (2003) performed a detailed study of spherical accretion of metal-free gas onto a growing hydrostatic core. In this case, electron scattering is the major source of opacity determining the Eddington luminosity $L_{\rm EDD}$ and the critical accretion rate $\dot{M}_{\rm crit}$, above which the protostellar luminosity exceeds $L_{\rm EDD}$ before the protostar reaches the zero-age main sequence (ZAMS), disrupting further accretion. As estimated in Bromm and Loeb (2004), if we assume the protostellar luminosity before the onset of hydrogen burning is approximately the accretion luminosity, $L_{\rm acc} \simeq GM_{*}\dot{M}/R_{*}$, and set this luminosity equal to $L_{\rm EDD}$, we find that

$$\dot{M}_{\rm crit} \simeq \frac{L_{\rm EDD}R_{*}}{GM_{*}} \sim 5 \times 10^{-3}\,{\rm M_{\odot}yr^{-1}}\ , \qquad (2.2)$$

where $R_{*} \sim 5\,{\rm R_{\odot}}$ (Bromm et al. 2001c). This approximation is quite close to that found in the calculations of Omukai and Palla (2003). It should be noted that initial accretion rates higher than $\dot{M}_{\rm crit}$ are possible since protostars begin with much larger radii and only gradually shrink during Kelvin-Helmholtz contraction.

Other types of feedback also have the potential to halt protostellar accretion and set the upper mass limit of Pop III stars. McKee and Tan (2008) consider several feedback mechanisms operating during Pop III star formation, including H_2 photodissociation and Lyα radiation pressure. They find, however, that the accretion rate is not significantly reduced through feedback until HII region breakout beyond the gravitational escape radius, generally occuring once the star has reached 50-100 $\rm M_{\odot}$. Omukai and Inutsuka (2002), on the other hand, find that for spherically symmetric accretion onto an ionizing star, the formation of an HII region in fact does not impose an upper mass limit to Pop III stars. As McKee and Tan (2008) determine, however, this does not remain the case for rotating inflow.

This previous work shows that further considerations such as a time-dependent accretion rate and a non-spherical, disk-like geometry around the protostar (see also Tan and McKee 2004) will be integral to fully determining the effects of protostellar feedback and will require study through three-dimensional calculations. We do not include any radiative feedback effects here, and thus our work represents a no-feedback limit of protostellar accretion onto a Pop III star. However, during the initial stages of protostellar growth, the feedback should be much weaker than in later stages when the star becomes more massive and luminous. As mentioned above, McKee and Tan (2008) estimate that the accretion rate is not significantly reduced until the Pop III star has gained $\sim 50\ \mathrm{M}_{\odot}$, and the rate of protostellar mass growth given by Bromm and Loeb (2004) indicates that such masses are not reached until $\sim 10^4$ yr after accretion begins. We thus end our calculation somewhat before this, after 5000 yr of accretion, before feedback effects have become too strong to ignore. Up until this point, our calculations should still give a good estimate of the geometry and possible fragmentation of the prestellar core as well as the early protostellar accretion rate and its time dependence.

2.2.3 Chemistry, heating and cooling

The chemistry, heating and cooling of the primordial gas is treated in a fashion very similar to previous studies (e.g. Bromm and Loeb 2004; Yoshida et al. 2006). We follow the abundance evolution of H, H^+, H^-, H_2, H_2^+, He, He^+, He^{++}, e^-, and the deuterium species D, D^+, D^-, HD, and HD^+. We use the same chemical network as used in Johnson and Bromm (2006) and include the same cooling terms.

At densities greater than $\simeq 10^8\ \mathrm{cm}^{-3}$, three-body processes gain importance. The reaction rates for

$$\mathrm{H} + \mathrm{H} + \mathrm{H} \rightarrow \mathrm{H}_2 + \mathrm{H} \tag{2.3}$$

and

$$\mathrm{H} + \mathrm{H} + \mathrm{H}_2 \rightarrow \mathrm{H}_2 + \mathrm{H}_2 \tag{2.4}$$

must be included (Palla et al. 1983). Because the gas is becoming fully molecular, in our cooling rates we furthermore account for enhanced cooling due to collisions between H_2 molecules. The heating rate due to H_2 formation heating is also included. Furthermore, the equation of state of the gas must be modified. More specifically, we adapt the adiabatic exponent γ_{ad} and the mean molecular weight μ to account for the increasing H_2 abundance f_{H_2}. These modifications for densities greater than 10^8 cm^{-3} are applied in the same way as described in Bromm and Loeb (2004), except for the modification of γ_{ad}, which is handled in the same way as decribed in Yoshida et al. (2006).

2.3 Numerical Methodology

2.3.1 Initial setup

We carry out our investigation using Gadget, a widely-tested three dimensional smoothed particle hydrodynamics (SPH) code (Springel et al. 2001; Springel and Hernquist 2002). Simulations are performed in a periodic box with size of 100 h^{-1} kpc (comoving) and initialized at $z = 99$ with both DM particles and SPH gas particles. This is done in accordance with a ΛCDM cosmology with $\Omega_\Lambda = 0.7$, $\Omega_{\mathrm{M}} = 0.3$, $\Omega_{\mathrm{B}} = 0.04$, and $h = 0.7$. We use an artificially large normalization of the power spectrum, $\sigma_8 = 1.4$, to accelerate structure formation in our relatively small box. As discussed in Chapter 2.5, our high value of σ_8 is expected to have little effect on our overall qualitative results, though this will be explored further in future work.

A preliminary run with a modest resolution of $N_{\rm SPH} = N_{\rm DM} = 128^3$ allows us to locate the formation site of the first minihalo. We then employ a standard hierarchical zoom-in procedure to achieve the necessary high-mass resolution in this region (e.g., Navarro and White 1994; Tormen et al. 1997; Gao et al. 2005). This method was also used in the work of Greif et al. (2008), in which they simulated the formation of a first galaxy beginning from cosmological initial conditions. Applying this method for our calculation involved beginning the simulation again at $z = 99$, but now with an additional three nested refinement levels of length 40, 30, and 20 kpc (comoving) centered on the site where the first minihalo will form. This high-resolution run is thus initialized at high redshift with the same initial fluctuations as in the preliminary low-resolution run, though the high-resolution region further includes fluctuations at smaller wavelength scales as allowed by the increased Nyquist frequency.

Particle positions are shifted so that the high resolution region will be in the center of the simulation box. Each level of higher refinement replaces particles from the lower level with eight child particles such that in the final simulation a parent particle is replaced by up to 512 child particles. The highest-resolution gas particles each have a mass $m_{\rm SPH} = 0.015$ M$_{\odot}$, so that the mass resolution of the refined simulation is: $M_{\rm res} \simeq 1.5 N_{\rm neigh} m_{\rm SPH} \lesssim 1$ M$_{\odot}$, where $N_{\rm neigh} \simeq 32$ is the typical number of particles in the SPH smoothing kernel (e.g. Bate and Burkert 1997).

The size of the refinement levels had to be chosen carefully. The level of highest refinement must be large enough to encompass all the mass that will eventually become the first minihalo. If this level of highest refinement is too small, lower-resolution particles will drift into the center of the collapsing region and disrupt the collapse of the high-resolution particles. Furthermore, there will be some artificial density enhancement for lower-resolution particles that are near the boundary of a higher-resolution region. This is because the particles of lower refinement levels have higher masses, and for a given density the corresponding smoothing length for lower-resolution particles should be larger than the smoothing length for higher-resolution particles. Smoothing lengths for particles of both resolutions will be very similar, however, if they are very close to each other. This causes low-resolution particles near a boundary to have artificially reduced smoothing lengths and overly enhanced densities. However, this will not pose a problem as long as the highest refinement level is large enough such that the low-resolution particles are well outside of the collapsing region of interest.

2.3.2 Sink particle creation

When the density of a gas particle becomes greater than $n_{\mathrm{max}} = 10^{12}\,\mathrm{cm}^{-3}$, this particle and the surrounding gas particles within a distance of less than the accretion radius r_{acc} are converted into a single sink particle. We set r_{acc} equal to the resolution length of the simulation, $r_{\mathrm{acc}} = L_{\mathrm{res}} \simeq 50\,\mathrm{AU}$, where:

$$L_{\mathrm{res}} \simeq 0.5 \left(\frac{M_{\mathrm{res}}}{\rho_{\mathrm{max}}} \right)^{1/3} ,$$

with $\rho_{\mathrm{max}} \simeq n_{\mathrm{max}} m_{\mathrm{H}}$. The sink particle's initial mass is close to the simulation's resolution mass, $M_{\mathrm{res}} \simeq 0.7\ \mathrm{M}_{\odot}$.

Our density criterion for sink particle formation is robust even though we do not explicitly check that the sink region satisfied further criteria such as being gravitationally bound and not having rotational support. As discussed in Bromm et al. (2002), crossing the $n_{\rm max}$ threshold is already equivalent to meeting these further criteria due to the runaway nature of the collapse. The average density of the disk (see Chapter 2.4.2.1) does not go above $\simeq 10^{10}$ cm^{-3}, and gas must collapse to densities two orders of magnitude higher before a sink is formed at the center of the infalling region. This along with our very small value for $r_{\rm acc}$ ensures that the particles that become sinks are indeed undergoing gravitational collapse. Furthermore, an examination of movies of the simulation shows that even the lowest-mass sinks are created only in pre-existing high-density clumps of gas that formed through gravitational instability, even though the clumps may no longer be clearly visible after the sink forms and accretes mass. During earlier test runs, however, using only the density criterion was problematic for other numerical reasons. This was because the larger sinks would contribute their high masses to the kernels of nearby gas particles, causing them to artificially jump to $n > 10^{12}\,{\rm cm}^{-3}$ and become sink particles themselves. These artificial sink particles had masses well below $M_{\rm res}$. However, once we corrected this problem by removing all sink particles from the density calculation, all sinks that were formed had initial masses $\geq M_{\rm res}$.

After a sink's formation, its density, temperature, and pressure are no longer evolved in time. Instead, their density is held constant at 10^{12} cm^{-3}. The temperature of the sinks is also held constant at 650 K, a typical temperature for gas reaching 10^{12} cm^{-3}, and the sinks are furthermore kept at the pressure which corresponds to the above temperature and density. Giving the sink a temperature and pressure makes it behave more like a gas particle, and it furthermore prevents the existence of a pressure vacuum around the sink that would make the sink accretion rate artificially high (see Bromm et al. 2002; Martel et al. 2006). Changes in the sink's position, velocity, and acceleration due to gravitational interaction are still evolved, however, and as the sink accretes mass its gravity becomes the dominant force, and it gradually begins to act more like a non-gaseous N-body particle.

Once a sink particle is formed, all gas particles or other sink particles that cross within $r_{\rm acc}$ of the sink particle are removed from the simulation, and their mass is added to that of the sink particle. After each subsequent accretion event, as well as when the sink is initially formed, the position and velocity of the sink are set to be the mass-weighted average of the sink particle and the gas particles that it has accreted. The sink approximately represents the growing hydrostatic core, though its size, of order $r_{\rm acc}$, is much larger than the true expected size of a core (e.g. Omukai and Nishi 1998).

The sink particle method has multiple advantages. It eliminates the need to include high density physics that becomes relevant only at $n > 10^{12}$ cm^{-3}. Furthermore, simulation timesteps become prohibitively small as the density increases, and representing a region of $n > 10^{12}$ cm^{-3} with a single sink particle allows the mass flow into protostellar regions to be followed for many dynamical times without continuing to increasingly high densities and small timesteps. Instead of estimating the accretion rate from the instantaneous density and velocity profiles at the end of the simulation, as done in Abel et al. (2002) and Yoshida et al. (2006), the sink particle method allows the accretion history to be directly followed. Furthermore, without the sink particle method, finding multiple fragments would require that they form at very nearly the

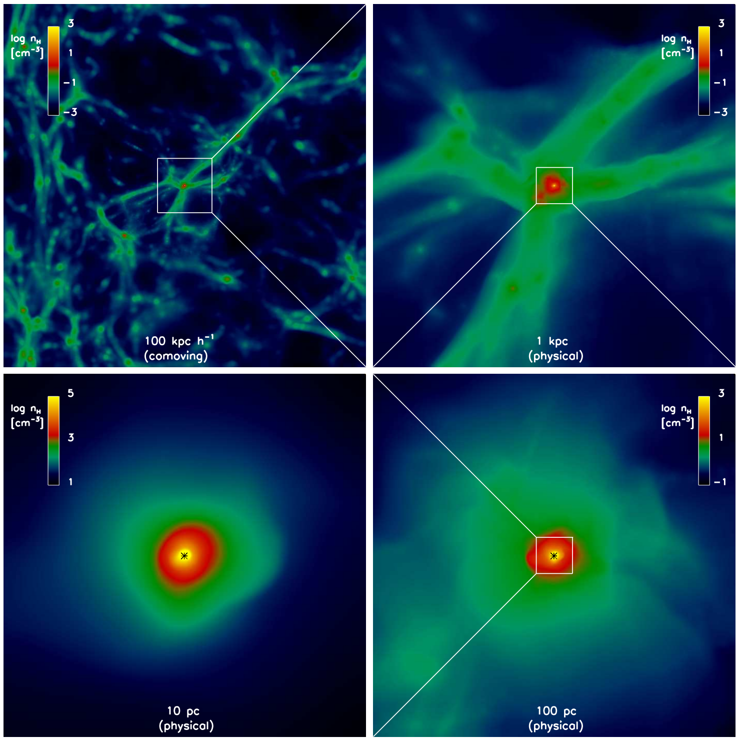

Figure 2.1: Final simulation output shown in density projection along the x-z plane on progressively smaller scales, as labeled on each panel. White boxes denote the region to be depicted in the next-smallest scale. In the bottom two panels, the asterisk denotes the location of the first sink formed. *Top left:* Entire simulation box. *Top right:* Minihalo and surrounding filamentary structure. *Bottom right:* Central 100 pc of minihalo. *Bottom left:* Central 10 pc of minihalo. Note how the morphology app roaches an increasinglysmooth, roughly spherical distribution on the smallest scales, where the gas is in quasi-hydrostatic equilibrium, just prior to the onset ofrunaway collapse.

same time, such as the fragments in Turk et al. (2009) which formed only 60 years apart. Using sink particles allows for the study of fragmentation that occurs on significantly longer timescales than this.

2.4 Results

2.4.1 Initial runaway collapse

Fig. 2.1 shows the final simulation output on various scales. The expected filamentary structure is apparent, and the first minihalo has formed in the central region where several filaments intersect by $z \simeq 20$. We measure the halo virialization radius $r_{\rm vir}$ as the point at which $\rho_{\rm DM} = \rho_{\rm vir} \equiv 200\rho_{\rm b}$, where $\rho_{\rm DM}$ is the average halo DM density, $\rho_{\rm vir}$ is the DM density at the point of virialization, and $\rho_{\rm b}$ is the average background matter density at the time of halo virialization. We then find that $r_{\rm vir} \simeq 90$ pc and $M_{\rm halo} \simeq 2.6 \times 10^5$ $\mathrm{M}_{\odot}$. The spin parameter $\lambda = J|E|^{1/2}/\mathrm{G}M^{5/2}$ is approximately 0.13 for our halo, where J is the total angular momentum, E is the binding energy, and M is the total halo mass. For our minihalo λ is higher than the typical value of 0.05 (e.g. Barnes and Efstathiou 1987; Jang-Condell and Hernquist 2001). This large spin may result from our enhanced value of σ_8. However, as discussed in Chapter 2.5, the angular momentum profile of the central gas in our simulation is still quite similar to that found from previous cosmological simulations initialized with a lower σ_8. Thus, our overall results concerning disk evolution and fragmentation are not expected to significantly change with a lower value of minihalo spin or σ_8.

After the DM in the minihalo virializes, the gas continues to collapse. As shown in Fig. 2.2, the results of our calculation up to the point of creation of the first sink particle agree well with previous studies (e.g. Bromm and

Larson 2004; Yoshida et al. 2006). As expected, the gas heats adiabatically until reaching $n \sim 1$ cm^{-3}, where it attains maximum temperatures of ~ 1000 K. After this point the gas begins to cool through H_2 rovibrational transitions, reaching a minimum temperature of $T \sim 200\,\mathrm{K}$ at a density of $n \sim 10^4\,\mathrm{cm}^{-3}$. This is the density at which the gas reaches a quasi-hydrostatic 'loitering phase' (Bromm et al. 2002). After this phase the gas temperature rises again due to compressional heating until $n \sim 10^8$ cm^{-3}, when three-body processes become important and cause the gas to turn fully molecular by $n \sim 10^{12}\,\mathrm{cm}^{-3}$ (see detailed discussion in Yoshida et al. 2006, 2008).

Fig. 2.3 shows the radial structure of the gas surrounding the density peak just before the first sink particle is created (compare with figure 2 in Bromm and Loeb 2004). The gas inside the central 100 AU has become almost fully molecular, and it evolves roughly isothermally due to the approximate balance between compressional and H_2 formation heating and enhanced H_2 cooling. The deviation from spherical symmetry of this central region is apparent in the 'thickness' of the radial profiles, particularly the profile of the H_2 fraction f_{H_2}. However, the gas density and velocity profiles still have the same general properties as those of the spherically symmetric Larson-Penston type similarity solutions, an example of which is shown in Fig. 2.3. The good agreement is evident, at least for the initial collapse phase. Omukai and Nishi (1998) used the same solution to describe their one-dimensional radiation-hydrodynamics simulations of primordial protostar formation. Though the velocities in the similarity solution are normalized to higher values, the velocites in our three-dimensional calculation exhibit very similar overall behavior, and the density profile matches the similarity solution especially well.

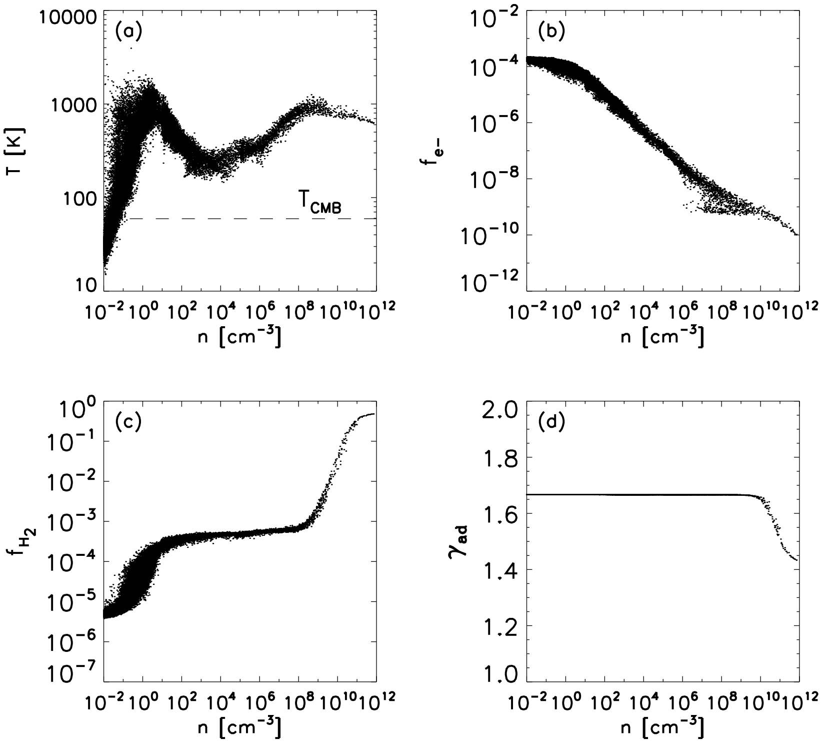

Figure 2.2: Physical state of the collapsing core. The situation is shown just prior to the formation of the first sink particle. *(a)* Temperature; *(b)* free electron fraction; *(c)* molecular hydrogen fraction; and *(d)* adiabatic exponent $\gamma_{\rm ad}$ vs. density.The gas that collapses into the minihalo is heated adiabatically to $\sim 1000\,$K as it reaches $n \sim 1$ cm^{-3} (panel a). At this point $f_{\rm H_2}$ becomes high enough (panel c) to allow the gas to cool through H$_2$ rovibrational transitions to a minimum of $T \sim 200\,$K, which is reached at $n \sim 10^4$ cm^{-3} (panel a). After the onset of gravitational instability, the gas reaches yet higher densities, and is heated to a maximum of $\sim 1000\,$K once it approaches a density of $\sim 10^8\,$cm^{-3}. At this density three-body reactions become important, and the gas is rapidly converted into fully molecular form (panel c). The increased H$_2$ cooling rate then roughly equals the adiabatic heating rate, and thus the highest density gas is nearly isothermal. As the gas is transformed into molecular form, the equation of state changes as well so that $\gamma_{\rm ad}$ evolves from 5/3 to approximately 7/5 (panel d).

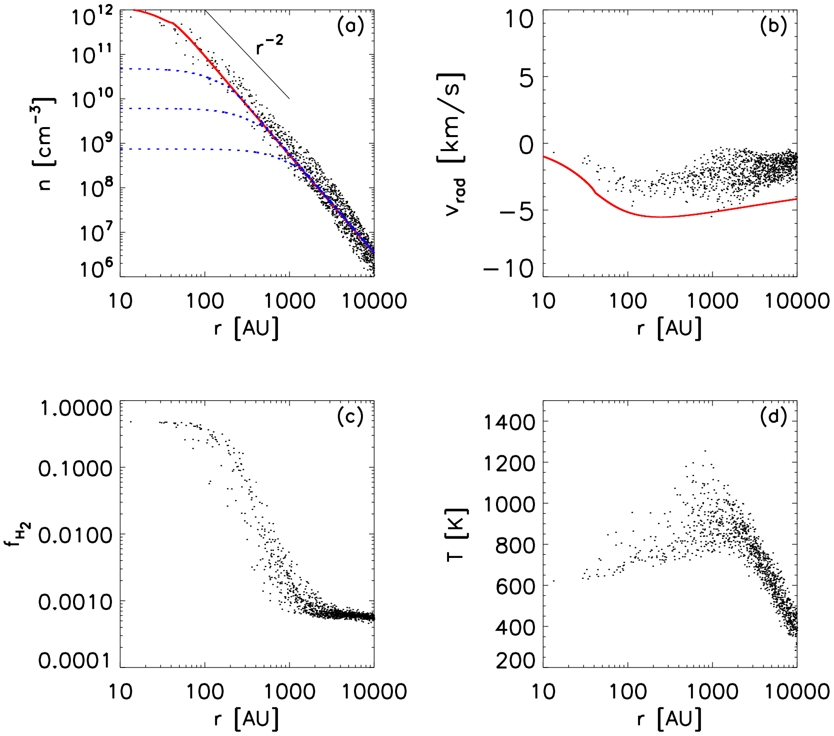

Figure 2.3: Initial collapse prior to the formation of the first sink particle. Shown are a number of variables as a function of radial distance from the density maximum. *(a)* Number density; *(b)* radial velocity; *(c)* molecule fraction; and *(d)* temperature vs. r. Also shown are the number density and radial velocity of a Larson-Penston type similarity solution for the equation of state $P = K\rho^{\gamma}$, where $\gamma = 1.09$ and $K = 4.2 \times 10^{11}$ (in cgs units), as in Omukai & Nishi (1998). The solid red lines (in panels a and b) represent the latest stage of collapse that was calculated, when the peak density is near $10^{12}\,\mathrm{cm}^{-3}$, while the dashed blue lines (in panel a) represent various earlier stages of collapse. Note that the analytical solution reproduces the density profile found in the numerical calculation very well. The velocity profile is also in reasonable agreement with the simulation, though, also as in Omukai & Nishi (1998), exhibiting a somewhat larger normalization due to differences in initial and boundary conditions.

2.4.2 Protostellar accretion

2.4.2.1 Disk formation

We next discuss the transition from the quasi-spherical initial collapse towards a disk-like configuration. This transition is clearly visible in the velocity structure of the central region, which changes dramatically over the last several thousand years of the simulation as the disk-like nature of the central region becomes more apparent over time. In Fig. 2.4, we illustrate the evolution of the radial (left panels) and rotational velocity (right panels), measured with respect to the most massive sink. In comparing to the free-fall velocity, we calculate $v_{\rm ff}$ using the enclosed mass $M_{\rm enc}$ within a radial distance r from the main sink. At both times shown, 250 and 5000 yr after initial sink formation, pressure support from the central gas leads to a deviation from pure free fall, but the overall behavior of the radial velocity of the outer particles is similar to that of the $v_{\rm ff}$ profile. This is not the case for the particles very near the sink, however. The average radial velocity of the central gas particles, particularly the cold ones (shown in blue), approaches zero as the gas begins to exhibit more rotational motion.

The central region is evolving into a Keplerian disk ($v_{\rm rot} \propto r^{-1/2}$) by just 250 yr after the first sink has formed. Note the comparison between the particle rotational velocities $v_{\rm rot}$ and the Keplerian velocity $v_{\rm Kep}$ (red line in Fig. 2.4), defined as

$$v_{\rm Kep} = \sqrt{\frac{GM_{\rm enc}}{r}} \ . \tag{2.5}$$

From Fig. 2.4 (panel b), it is apparent that the inner 100-200 AU of the disk are becoming rotationally supported ($v_{\rm rot} \gtrsim v_{\rm Kep}$) by 250 yr after sink formation.

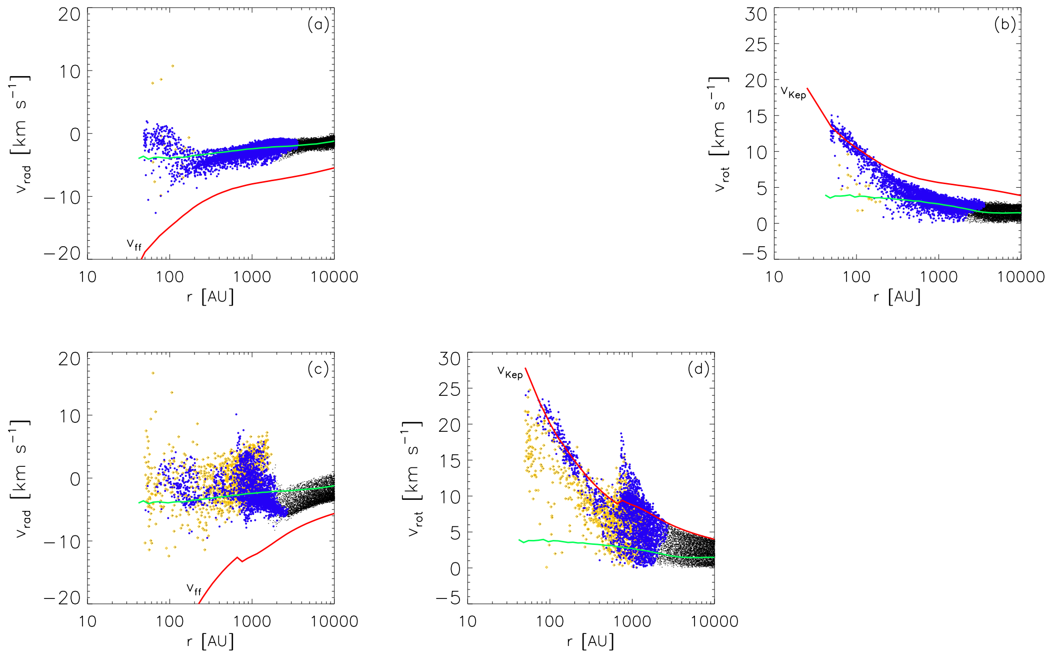

Figure 2.4: Kinematics around the main sink particle. *(a)* Radial velocity versus distance from the main sink at 250 yr after the initial sink formation. Colored particles are those with densities greater than 10^8 cm^{-3}. Yellow diamonds: high-density heated particles with temperatures > 2500 K. Blue circles: high-density cool particles with temperatures < 2500 K. Red line: gravitational free-fall velocity $v_{\rm ff}$, determined using the enclosed mass within the given radius. For comparison to the physical situation at earlier times, the green line is the radially averaged radial velocity around the main sink immediately after it first forms. *(b)* Rotational velocity versus distance from the main sink at 250 yr after sink formation. Blue and yellow particles have the same meaning as in panel (a). Red line: $v_{\rm Kep}$, calculated using the enclosed mass. Green line: radially averaged rotational velocity around the main sink immediately after it first forms. *(c)* Radial velocity versus distance from main sink at 5000 yr after initial sink formation. Notation is the same as in panel *(a)*. *(d)* Rotational velocity versus distance from main sink at 5000 yr after initial sink formation. We adopt the same convention as in panel (b). Towards later times, the cold gas settles into a nearly Keplerian configuration.

Despite some amount of rotational support, however, a fraction of the particles is still able to approach the sink, thus allowing continued accretion. After 5000 yr, the disk has grown to a radial size of slightly less than 2000 AU (panel c), while the cold disk particles exhibit nearly Keplerian motion (panel d). The spike at 700 AU (panel d) corresponds to a group of particles rotating around the second largest sink.

The assembly of the disk-like configuration around the first sink particle, and the subsequent fragmentation into additional sinks, are shown in Fig. 2.5. The growing disk is unstable and develops a pronounced spiral pattern, leading in turn to the formation of multiple high-density peaks. As is evident, regions of high density correlate with those of low temperature, due to the enhanced cooling there. The expanding, hour-glass shaped, bubble of hot gas (clearly visible in the bottom row) reflects the release of gravitational energy when particles fall into the deepening potential well around the central sink. The corresponding virial temperature is

$$T_{\rm vir} \simeq \frac{G M_{\rm sink} m_{\rm H}}{k_{\rm B} r_{\rm acc}} \simeq 10^4\,{\rm K},$$

where $M_{\rm sink} \sim 10\,{\rm M}_{\odot}$. This gravitational source of heating causes the emergence of a hot gas phase around the central sink ($T \simeq 7,000$ K), even in the absence of any direct radiative feedback from the protostar which is not included here. In Fig. 2.6, we illustrate the corresponding velocity field in two orthogonal planes at 5000 yr. The small infall velocities onto the disk and the high rotational, roughly Keplerian, velocites within the disk are apparent.

Fig. 2.7 shows the growth of the disk over time, where $t = 0$ yr marks the point at which the first sink forms. We estimate the disk mass by including all gas particles, sinks excluded, with a density greater than 10^8 cm^{-3} and a

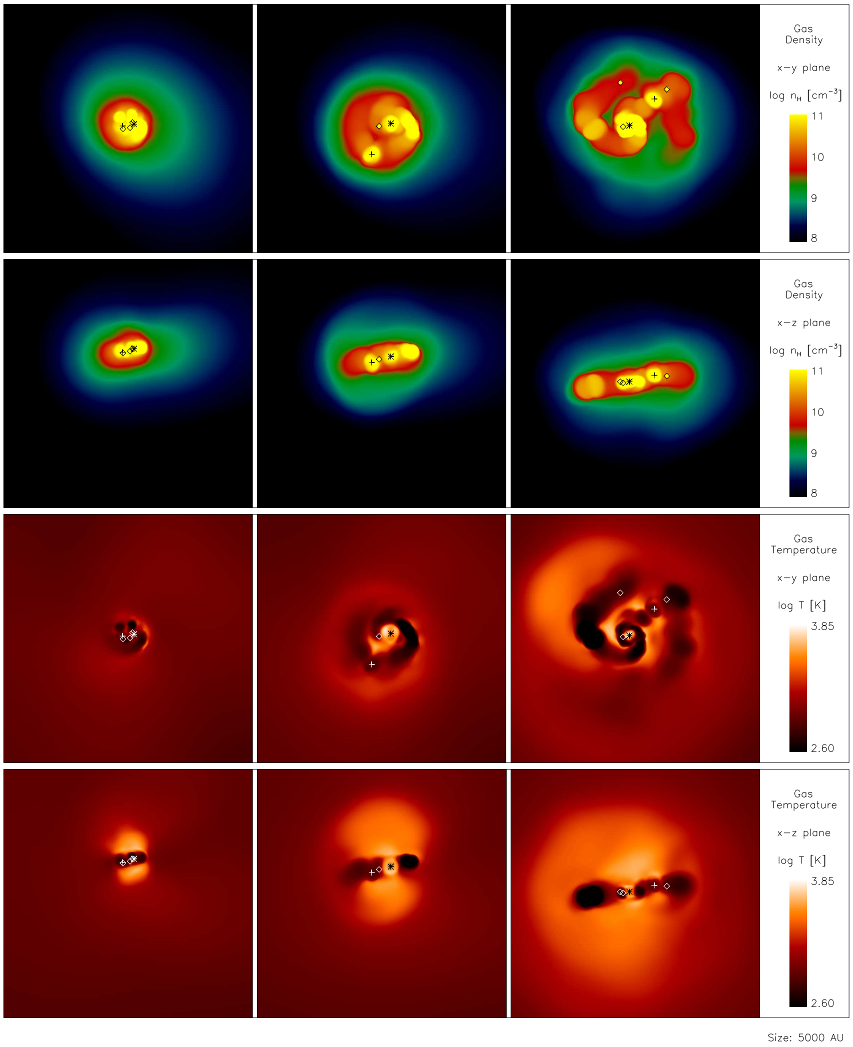

Figure 2.5: Density and temperature projections of the central 5000 AU. Each row shows the projections at 1000 yr (left), 2000 yr (center), and 5000 yr (right) after the initial sink formation. Asterisks denote the location of the most massive sink. Crosses show the location of the second most massive sink. Diamonds are the locations of the other sinks. *Top row* : Density structure of the central region in the x-y plane. *Second row* : Density structure of the central region in the x-z plane. *Third row* : Temperature structure of the central region in the x-y plane. *Bottom row* : Temperature structure of the central region in the x-z plane.

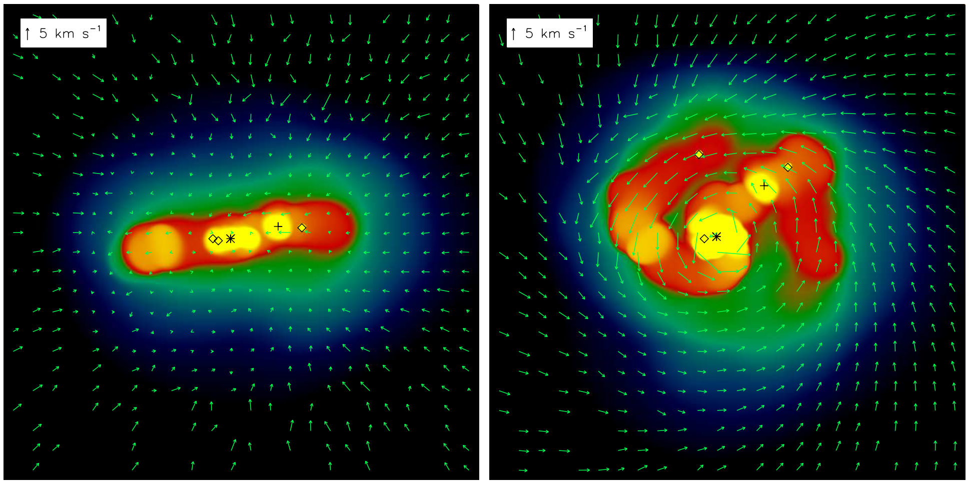

Figure 2.6: Velocity field of the central gas distribution. Sinks are denoted as in Fig. 2.5. *Top* : Density projection in the x-z plane after 5000 yr, shown together with the velocity field. Velocities are measured with respect to the center of mass of all $n > 10^8$ cm^{-3} particles. *Bottom* : Same as what is shown in the top panel except in the orthogonal (x-y) plane. It is evident how an ordered, nearly Keplerian velocity structure has been established within the disk.

specific angular momentum within 50% of $j_{\rm Kep}$, the specific angular momentum expected for a centrifugally supported disk, where $j_{\rm Kep} = v_{\rm Kep} r$. We here refer all velocities to the center of mass of the high-density ($n > 10^8$ cm^{-3}) particles. In addition, we track the evolution of the mass in the ‘cool’ (dotted line) and ‘hot’ gas phase (dashed line), corresponding to temperatures less than 2500 K and greater than 2500 K, respectively. The mass of heated particles grows soon after the first sink is in place, whereas the cold component decreases as its mass is incorporated into the sinks or becomes part of the hot phase. Eventually what remains of the cold component is confined to the disk itself (see bottom two rows of Fig. 2.5).

The characteristics of the star-disk system in our simulation can be compared to the analytic predictions of Tan and McKee (2004). At a density and temperature of 10^8 cm^{-3} and 1000 K, respectively, we find a value of K' ~ 1.33 from their equation (7), where K' is the entropy parameter, defined by

$$K' = \frac{P/\rho^{\gamma}}{1.88 \times 10^{12}\mathrm{cgs}} = \left(\frac{T}{300\,\mathrm{K}}\right)\left(\frac{n_{\mathrm{H}}}{10^4\mathrm{cm}^{-3}}\right)^{-0.1} . \tag{2.6}$$

We estimate that the total star-disk system mass (red line in Fig. 2.7) is ~ 100 M$_{\odot}$ at the end of our simulation and set ϵ_{*d} equal to 1 for the no feedback case, where ϵ_{*d} is the fraction of infalling mass that is able to reach the star-disk system without being diverted by protostellar outflows, again in the terminology of Tan & McKee. From their equation (8), we then calculate an expected accretion rate onto the star-disk system of $\lesssim 10^{-2}$ M$_{\odot}$ yr^{-1}. In our simulation we find that over the 5000 yr of sink accretion, mass flows onto the star-disk system very steadily at approximately the same rate of $\sim 10^{-2}$ M$_{\odot}$ yr^{-1}, which is also near the value for the average accretion rate onto the main sink particle (see Chapter 2.4.2.4). Fig. 2.7 further shows that once the first sink forms, the disk mass stays fairly constant at ~ 35 M$_{\odot}$ as mass falling from the outer regions onto the disk replaces the material accreted onto the sinks at similar rates.

Tan and McKee (2004) furthermore predict the time needed to build up a given stellar mass in their equation (9). If we assume a value of 1 for f_{d}, the ratio of disk to stellar mass, then the time to build up a 43 M$_{\odot}$ star (the final mass of the main sink - see Chapter 2.4.2.4) is roughly 9000 yr. The simulation yields a similar though smaller value of 5000 yr, which reflects the slightly higher accretion rate of our simulation. Finally, if we estimate a value of 1 for f_{Kep}, the ratio of rotational to Keplerian velocity at the sonic point, then from equation (15) of Tan and McKee (2004) we find a predicted disk

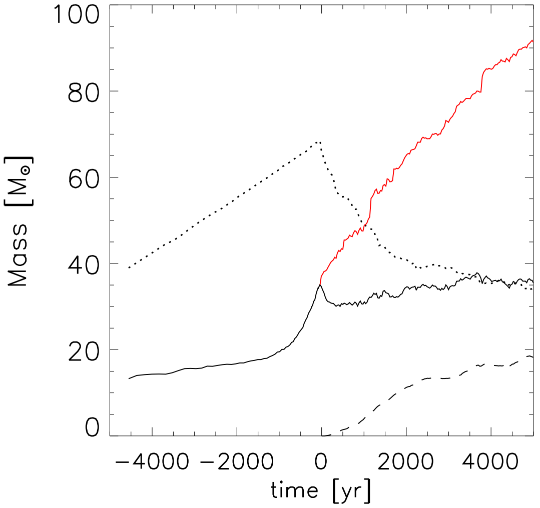

Figure 2.7: Disk mass vs. time since the creation of the first sink particle (solid line). Disk particles are considered to be all gas particles, excluding sinks, with density greater than 10^8 cm^{-3} and a specific angular momentum within 50% of $j_{\rm Kep}$. Once the first sink forms at $t = 0$ yr, the red line shows the total mass of the star-disk system. Also shown is the total mass of $n > 10^8$ cm^{-3} particles (sinks excluded) with temperatures less than 2500 K (dotted line) and temperatures greater than 2500 K (dashed line).

radius of $\sim$ 3000 AU. This value is also similar to the value of $\sim$ 2000 AU found from the simulation.

2.4.2.2 Angular momentum evolution

How does the distribution of angular momentum change during the simulation? In Fig. 2.8, we demonstrate the increase in rotational support of the central region over time. Shown are the evolution of the enclosed mass (top panel), the specific angular momentum along the z-axis, j_z (middle panel), and the degree of rotational support (bottom panel). Here, rotational support is defined as

$$f_{\rm rot} = \frac{j_z}{j_{\rm Kep}} \ . \tag{2.7}$$

We determine j_z by averaging over all cool ($T < 2500\,{\rm K}$) particles within small radial bins covering a total distance of 10^5 AU. Note how the inner $200\,{\rm M}_\odot$, corresponding to the central 10^4 AU, have spun up significantly in the process of disk formation. This occurs as the inner mass shells fall towards the center, leading to the increase in rotational support. The inner 200 AU of cool gas are fully rotationally supported by the end of the simulation (bottom panel).

To confirm that numerical viscosity is not a dominant factor in determining our results, we have compared the torque due to numerical viscosity ($\vec{\tau}_{\rm visc}$) to those exerted by gravity and pressure ($\vec{\tau}_{\rm grav}$ and $\vec{\tau}_{\rm pres}$). The total torque on a given particle within a gas cloud is given by

$$\begin{aligned} \vec{\tau}_{\rm tot} &= \vec{\tau}_{\rm grav} + \vec{\tau}_{\rm pres} + \vec{\tau}_{\rm visc} \\ &= m_{\rm part}\vec{r}_{\rm part} \times \left(\vec{a}_{\rm grav} + \vec{a}_{\rm pres} + \vec{a}_{\rm visc}\right) \ , \end{aligned} \tag{2.8}$$

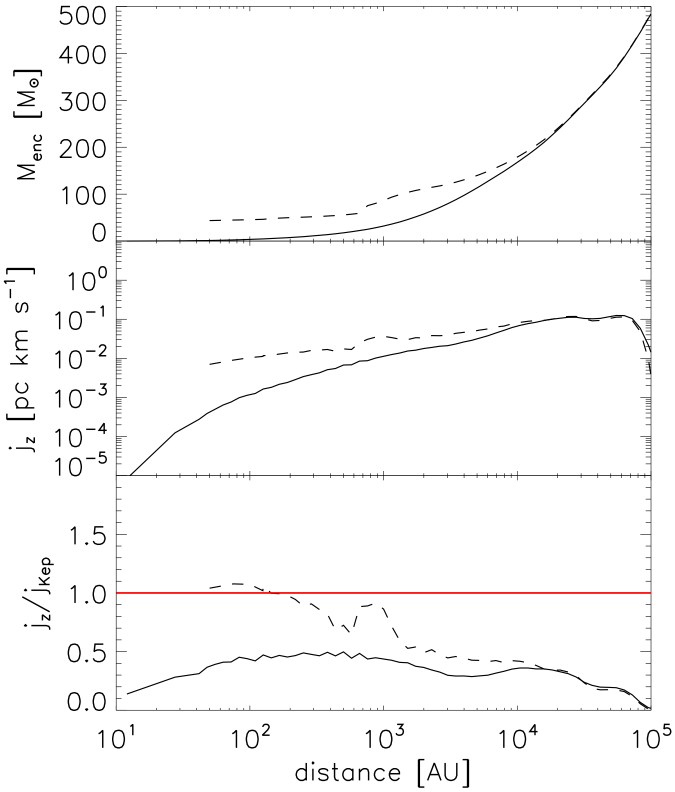

Figure 2.8: Angular momentum structure. *Top* : Enclosed mass versus distance from main sink particle at last simulation output before sink formation (solid line) and after 5000 yr of sink accretion (dashed line). *Middle* : Specific angular momentum j_z of the cool (T < 2500 K) gas with respect to distance from the main sink at the same corresponding times. *Bottom* : Degree of rotational support of the cool gas. The solid red line shows where $j/j_{\rm Kep} = 1$, the requirement for complete rotational support.

where $\vec{r}_{\rm part}$ is the distance of the particle from the center of the cloud, $m_{\rm part}$ the particle mass, and $\vec{a}_{\rm grav}$, $\vec{a}_{\rm pres}$ and $\vec{a}_{\rm visc}$ are the accelerations due to gravity, pressure and viscosity, respectively. Similar to Yoshida et al. (2006), we store these accelerations for each particle and every timestep. We find that torques from gravity and pressure are dominant by an order of magnitude except in regions near the sinks. The viscous torques within ~ 100 AU of the sinks may exceed the gravitational and pressure torques at any given instant. However, unlike $\vec{\tau}_{\rm grav}$ and $\vec{\tau}_{\rm pres}$, $\vec{\tau}_{\rm visc}$ near the sinks does not tend to continuously act in any preferred direction and thus averages out to be much smaller than the gravitational and pressure torques.

2.4.2.3 Binary and multiple formation

Around 300 yr after the first sink has formed, the disk becomes unstable to fragmentation and a second sink is created. We can estimate the value of Q in the Toomre criterion for disk gravitational instability,

$$Q = \frac{c_{\rm s}\kappa}{\pi G \Sigma} < 1 \ . \tag{2.9}$$

Here, Σ is the disk surface density and κ is the epicyclic frequency, which is equal to the angular velocity for Keplerian rotation. At this point in the simulation, the soundspeed $c_{\rm s}$ is approximately 3 km s^{-1} for a $\simeq 1000$ K disk, and $\kappa \simeq 3 \times 10^{-11}$ s^{-1} for a disk with Keplerian rotation at the disk outer radius, which we take to be $R_{\rm disk} \simeq 1000$ AU. The disk mass is close to 30 M$_{\odot}$, and $\Sigma \simeq {\rm M}_{\rm disk}/\pi R^2_{\rm disk} \sim 100$ g/cm^2. This gives $Q \sim 0.4$, well-satisfying the fragmentation criterion.

Soon after the disk instability sets in, a pronounced spiral structure develops, as is evident in Fig. 2.5. The spiral perturbation serves to transport

sink	t_{form} [yr]	M_{final} [$M_\odot$]	r_{init} [AU]	r_{final} [AU]
1	0	43	0	0
2	300	13	60	700
3	3700	1.3	930	1110
4	3750	0.8	740	890
5	4400	1.1	270	240

Table 2.1: Formation times, final masses, and distances from the main sink. We include all sinks still present at the end of the simulation.

angular momentum outward through gravitational torques, allowing some of the inner gas to accrete onto the sinks (see Krumholz et al. 2007). By 1000 yr after initial sink formation, several new fragments have formed, represented by new sink particles (shown in Fig. 2.5). Some of these fragments eventually merge with other more massive sinks, but by the end of our simulation we have 5 sink particles throughout the disk, described in Table 1. The two largest sinks are 700 AU apart, have a mass ratio of $\sim 1/3$, and form 300 yr apart (see Chapter 2.4.2.4 and Fig. 2.9). This is not unsimilar to the two fragments found in Turk et al. (2009), which had a separation of 800 AU, a mass ratio of $\sim 3/5$, and formed $\sim$ 60 yr apart. The three smallest sinks in our calculation are all around 1 $M_\odot$ and formed after approximately 4000 yr. Compared to the two largest sinks, these smaller sinks are quite low-mass and have been present in the simulation for only a short time. The two largest sinks seem to be the only long-term sinks in the simulation.

Analytical estimates concerning massive disk fragmentation by Kratter and Matzner (2006) showed interesting similarity to our results. They find that protostellar disks hosting massive stars (O and B stars) are prone to fragmenation for disk radii larger than 150 AU, and they predict that many low-mass companions will form in the disks around these stars at initial separations of 100-200 AU (compare with our Table 2.1). Though their estimate is based on optically thick disks undergoing viscous heating as well as stellar irradiation, the stabilizing effect of those heat sources is counteracted by rapid stellar accretion and high disk angular momentum. If protostellar feedback were included in our work, this could reduce the number of fragments that form, since the initial protostar could heat the disk and inhibit further fragmentation, perhaps leaving a binary instead of a mutiple system. This effect is shown in Krumholz et al. (2007), where the evolution of high-mass prestellar cores in the present-day universe is simulated. They find that protostellar radiative feedback inhibits fragmentation and that the majority ($\gtrsim$ 90 percent) of accreted stellar mass goes onto one protostar, though a small number of lower-mass stars can form at sufficiently large distances from the main protostar or in disk fragments formed through Toomre instability. It will thus be important to include protostellar feedback in future simulations to fully ascertain the multiplicity of Pop III star formation.

2.4.2.4 Accretion rate

How do the initial hydrostatic cores develop into fully formed Pop III stars? Fig. 2.9 shows the growth of the two most massive sink particles over time. We find that the main sink approximately grows as $M \propto t^{0.55}$ (red line). By 5000 yr after sink formation, the main sink has grown to 43 $\mathrm{M}_{\odot}$, only slightly higher than the corresponding result from Bromm and Loeb (2004). The jumps in mass are instances where smaller sinks merged with the largest sink. One caveat to keep in mind is that we did not explicitly check that these smaller sinks were not centrifugally supported against infall towards the main sink before they were merged. However, we examined the largest secondary sink ($\sim 4\,\mathrm{M}_\odot$) that merged with the main sink. This merger occured at 3700 yr after initial sink formation. We checked the secondary sink's specific angular momentum at the last simulation output before it merged with the main sink. At this time it was $\sim 100\,\mathrm{AU}$ away from the main sink, and its specific angular momentum with respect to the main sink was $2{\times}10^{21}$ cm^2 s^{-1}. This is less than the specific angular momentum required at this distance for centrifugal support against infall, $2.6{\times}10^{21}$ cm^2 s^{-1}. It is thus plausible that this was indeed a true merger.

In Fig. 2.9, we also show the corresponding accretion rate onto the most massive sink particle over time (panel b). The accretion rate is highly variable and initially very large: $\dot{M} \sim 7\mathrm{c}_s^3/G$, if we evaluate the sound speed at 700 K, and $\sim 50\mathrm{c}_s^3/G$ at 200 K. These rates are similar to those predicted in analytic solutions (Larson 1969; Penston 1969; Shu 1977), and to the result found in Bromm and Loeb (2004). Note that the accretion rate does generally decline over time approximately as $\dot{M} \propto t^{-0.45}$, except for a few 'spikes' in accretion when the main sink merges with other smaller sinks. For comparison the accretion rate onto the second largest sink (dotted line) is also shown, whose powerlaw fit goes as $\dot{M} \propto t^{-0.39}$ (fit not shown) and is normalized to a value of about 1/5 that of the main sink. The lower rate is expected since the second largest sink accretes significantly cooler gas.

As accretion onto the main sink continues, the overall average accretion rate will drop to a much lower value, closer to the average value found in Bromm and Loeb (2004). If accretion were to continue for the entire lifetime of the star, 3×10^6 Myr, and if the accretion rate continued to decrease as approximately $\dot{M} \propto \mathrm{t}^{-0.45}$, the final Pop III star would reach $M_* \lesssim 1000\ \mathrm{M}_\odot$. However, our fit likely overestimates the accretion rate at late times, and the

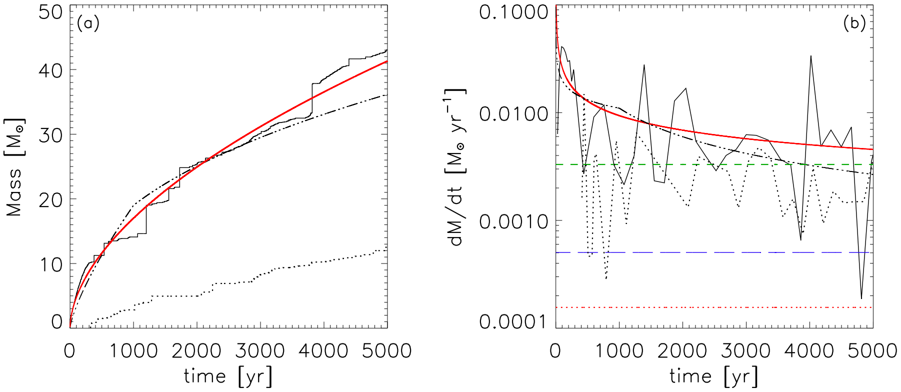

Figure 2.9: *(a)* Sink mass versus time since initial sink formation. The solid line shows the mass of the first sink particle over time in our calculation. The red line is the least-squares powerlaw fit to the sink mass over time, which goes as $M \propto t^{0.55}$. The dash-dotted line shows the result obtained by Bromm & Loeb (2004). The dotted line is the mass growth of the second largest sink. *(b)* Accretion rate versus time since initial sink formation. The solid line shows the accretion rate of the first sink particle throughout our calculation. The red line is the powerlaw fit to the mass accretion rate ($\dot{M} \propto t^{-0.45}$). The black dash-dotted line shows the instantaneous accretion rate found by Bromm & Loeb (2004), while the red dotted line is their average accretion rate over the lifetime of a Pop III star, determined by extrapolating their rate to 3×10^6 yr. The dotted line is the accretion rate of the second largest sink. Also shown are the Shu accretion rates for isothermal gas at 700 K (green short-dash line) and 200 K (blue long-dash line).

actual final mass of the star is likely to be significantly lower. Furthermore, feedback effects will likely slow accretion, or even halt it entirely, before the star dies. Thus, our extrapolation serves as a robust upper limit to the final Pop III stellar mass.

2.4.2.5 Thermodynamics of accretion flow

After the initial sink particle has grown in mass, the surrounding gas divides into two phases - a hot and cold one. In Fig. 2.10, we illustrate this bifurcation with a temperature-density phase diagram at various stages of the simulation. Heating becomes significant once the initial sink grows beyond 10 $M_{\odot}$. At this mass the gravitational force of the sink particle is strong enough to pull gas towards it with velocites sufficiently high to heat the gas to a maximum temperature of $\sim$ 7,000 K (see discussion in Chapter 2.4.2.1). This is the temperature where the collisional excitation cooling of atomic hydrogen begins to dominate over the adiabatic and viscous heating. The increasing mass of the sink causes a pressure wave to propagate outward from the sink and heat particles at progressively larger radii and lower density, as is visible in Fig. 2.5 and Fig. 2.10. The heated region extends out to $\sim$ 2,000 AU at 5000 yr. The pressure wave thus propagates at a subsonic speed of ~ 2 km s^{-1}.

The main sink is able to accrete a fraction of these heated particles (e.g. the yellow particle in Fig. 2.10), while it continues to accrete cold particles from the disk as well. We record the temperatures of the SPH particles accreted onto the sink, so that we can track the relative contributions from the two phases. When the main sink has grown to $\sim$ 30 $M_{\odot}$, accretion from the hot phase begins to occur, such that heated particles contribute slightly over 50% to the total rate towards the end of the simulation. By this time,

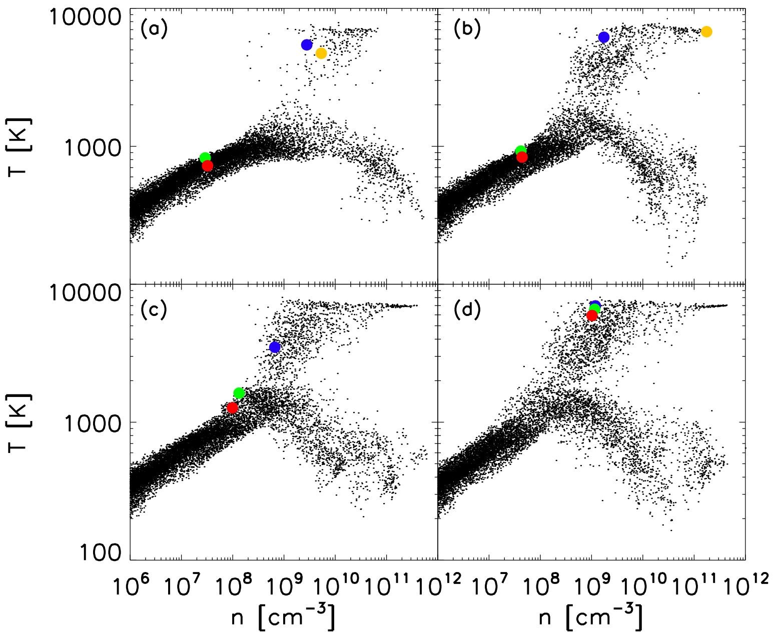

Figure 2.10: Evolution of thermodynamic properties. We plot temperature vs. number density at various times during the simulation. The colored dots trace the position of four representative particles, illustrating how the hot phase is populated. Note the hot particle that is accreted by the main sink $\sim 2000\,\mathrm{yr}$ after the sink's creation (yellow dot). The times are as follows: *(a)* 1000 yr. *(b)* 2000 yr. *(c)* 3000 yr. *(d)* 5000 yr.

the average temperature of all particles accreted onto the main sink is close to 3000 K, a value indicative of significant contributions from the hot phase. The second-most massive sink, on the other hand, accretes particles from only the cool phase as it has not yet reached a sufficiently high mass to capture heated particles. It has, however, just become massive enough to begin heating its surrounding particles. Fig. 2.11 reveals the location of the two different gas phases in a complementary way by showing where cooling due to H_2 (left panel) and atomic hydrogen line cooling dominate (right panel). H_2 cooling is important in the cold, dense gas of the disk-like structure, whereas atomic cooling occurs in the hot, nearly spherical region around the largest sink particle. This region grows in size as the sink itself gains mass. By the end of the simulation, a similar heated region is also beginning to expand around the second-most massive sink.

Since the heated region is created by the sink particle's potential well, we can estimate its extent by evaluating the Bondi radius, which marks the distance out to where the gravitational energy of the sink will be greater than the thermal energy of the gas. If we use the final mass of the main sink, $M_{\rm sink} \simeq 40\ {\rm M}_{\odot}$, and the maximum soundspeed of the gas particles, $c_{\rm s} \simeq 7$ km s^{-1} for temperatures of 7000 K, we find

$$R_{\rm B} \simeq \frac{G M_{\rm sink}}{c_{\rm s}^2} \simeq 750 {\rm AU} \ . \tag{2.10}$$

This is close to the size of the heated region seen in both Fig. 2.5 and Fig. 2.11. We should further note that, except for sink masses lower than $\sim 2\ {\rm M}_{\odot}$, $R_{\rm B}$ will be larger than $r_{\rm acc}$, which is held constant at 50 AU. When the main sink reaches larger masses and begins to accrete heated particles, $R_{\rm B}$ is in fact over an order of magnitude larger than $r_{\rm acc}$, indicating that our treatment of

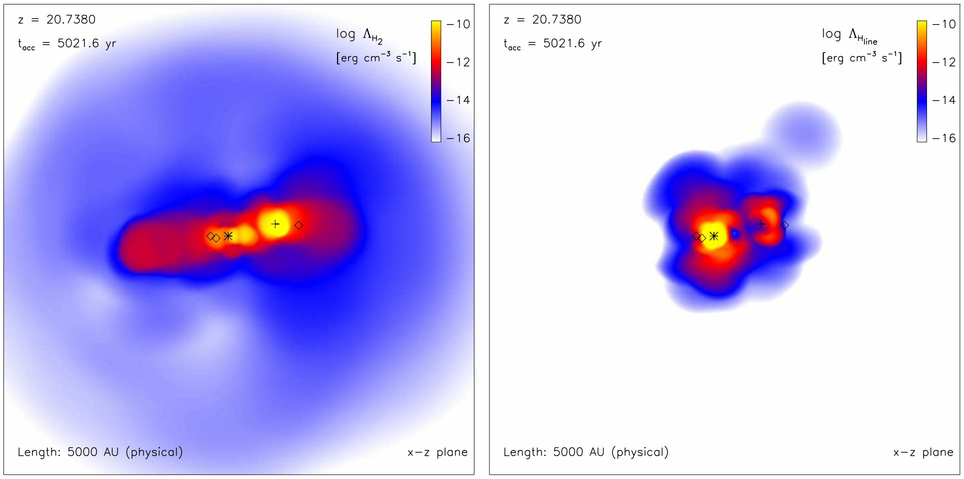

Figure 2.11: Dominant cooling processes in the center of the minihalo. Sinks are denoted as in Fig. 2.5. *Left* : H_2 cooling rate within the central 5000 AU, shown in projection along the x-z plane, after $\sim$ 5000 yr of accretion. *Right* : H line cooling rate in the same region and at the same time, again shown in projection along the x-z plane.

accretion is indeed conservative and that there is little un-physical accretion of heated particles.

2.4.2.6 Feedback

As noted earlier, the formation of a disk-like configuration around the protostar will have important implications for feedback effects. As demonstrated by McKee and Tan (2008), the disk structure will mitigate the impact of protostellar feedback. Radiation will be able to escape along the polar directions, and although the innermost, optically thick, part of the accretion disk is not resolved in our simulation, it would shield a portion of the outer accretion flow from direct feedback. Future three-dimensional simulations that include radiative feedback will yield a better understanding of how and when disk accretion onto a primordial protostar may be terminated. We now wish to assess how important this neglected feedback would be up to the stage simulated here.

In Fig. 2.12, we compare the accretion luminosity, L_{acc}, with the Eddington luminosity due to electron scattering and due to H^- opacity. Determining L_{acc} requires an estimate of the protostellar radius R_*. In the initial adiabatic accretion phase, before Kelvin-Helmholtz contraction has commenced, the photospheric opacity of the protostar is dominated by H^- bound-free absorption (i.e., 'Phase I' of Omukai and Palla 2003). The extremely strong sensitivity of the H^- bound-free opacity to temperature ($\kappa_{\mathrm{H}^-} \propto T^{14.5}$) locks the photospheric temperature to ~ 6000 K. We estimate that the protostar emits as a blackbody at this temperature and furthermore assume that the protostellar luminosity during this phase is dominated by L_{acc}. This is justified as long as $t_{\mathrm{acc}} \lesssim t_{\mathrm{KH}}$, where t_{acc} is the accretion timescale and t_{KH} the Kelvin-Helmholtz time. We then have

$$L_{*I} \simeq L_{\mathrm{acc}} = \frac{GM_*\dot{M}}{R_*} = 4\pi R_*^2 \sigma_{\mathrm{SB}} T^4 \ , \tag{2.11}$$

where L_{*I} is the protostellar luminosity during the adiabatic accretion phase, σ_{SB} is the Stefan-Boltzmann constant, and $T = 6000\,\mathrm{K}$. This results in

$$R_{*I} \simeq 50\mathrm{R}_{\odot} \left(\frac{M_*}{\mathrm{M}_{\odot}}\right)^{1/3} \left(\frac{\dot{M}}{\dot{M}_{\mathrm{fid}}}\right)^{1/3} \ , \tag{2.12}$$

where R_{*I} is the protostellar radius during the adiabatic accretion phase, and $\dot{M}_{\mathrm{fid}} \simeq 4.4 \times 10^{-3}\ \mathrm{M}_{\odot}\,\mathrm{yr}^{-1}$, the fiducial accretion rate used by Stahler et al. (1986) and Omukai and Palla (2003). Our simple estimate of how R_{*I} varies with mass and accretion rate is quite similar to the results of these more detailed previous studies, and here serves to highlight the relevant physics.

During the next phase, the protostellar radius begins to shrink due to Kelvin-Helmholtz contraction. The major source of opacity in the interior of the protostar is electron scattering, which is independent of density and temperature. This along with hydrostatic equilibrium yields the mass-luminosity relation $L_* \propto M_*^3$. Using figure 4 of Omukai and Palla (2003), we normalize this relation as follows:

$$L_{*II} \simeq 10^4 \mathrm{L}_\odot \left(\frac{M_*}{10\ \mathrm{M}_\odot} \right)^3 \ , \tag{2.13}$$

where L_{*II} is the protostellar luminosity during the Kelvin-Helmholtz contraction phase. If we further assume that $t_{\mathrm{KH}} \simeq t_{\mathrm{acc}}$, we arrive at

$$\frac{GM_*^2}{R_* L_*} \simeq \frac{M_*}{\dot{M}} \ . \tag{2.14}$$

Using $L_* \simeq L_{*II}$, we now find a relation for R_{*II}, the protostellar radius during the Kelvin-Helmholtz contraction phase:

$$R_{*II} \simeq 140 \mathrm{R}_\odot \left(\frac{\dot{M}}{\dot{M}_{\mathrm{fid}}} \right) \left(\frac{M_*}{10 \mathrm{M}_\odot} \right)^{-2} \ . \tag{2.15}$$

In determining the evolution of L_{acc}, we set $R_* = R_{*I}$ at early times when the protostar is still experiencing adiabatic accretion. When $M_* \sim 10\,\mathrm{M}_\odot$, after approximately 800 yr of accretion, the value of R_{*II} falls below that of R_{*I}. At this point, we estimate that Kelvin-Helmholtz contraction has commenced and switch to setting $R_* = R_{*II}$. The resulting transition in the

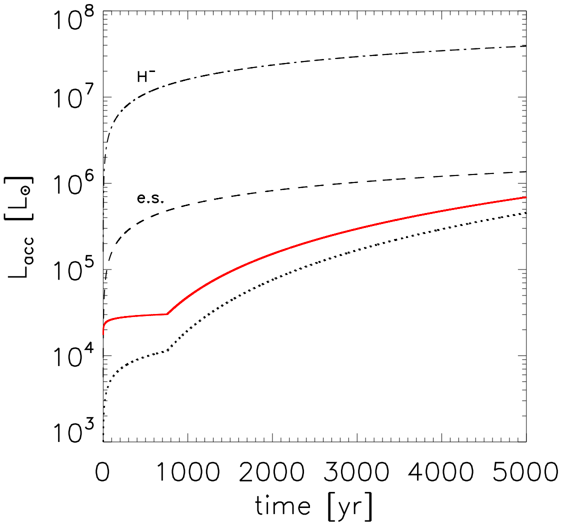

Figure 2.12: Impact of feedback on the accretion process. Solid red line is the accretion luminosity L_{acc} of the most massive sink versus time, calculated using $R_* = R_{*I}$ at early times and $R_* = R_{*II}$ at later times, as described in the text. In determining L_{acc} we use the power-law fit to the accretion rate ($\dot{M} \propto t^{-0.45}$). Dotted line is the prediction of L_{acc} by Tan & Mckee (2004) given $f_{\mathrm{d}} = 1$ and $K' = 1.33$. Dashed line is the Eddington luminosity L_{Edd} due to electron scattering, calculated using the sink mass. The dash - doted line is L_{Edd} due to H$^-$ bound-free opacity, calculated at a temperature of 6000 K. Note that the kink in the curves for the accretion luminosity is an artefact of our idealized modelling of protostellar structure.

growth of L_{acc} can be seen in Fig. 2.12. The discontinuous slope in the accretion luminosity is an artefact of our approximate modelling of protostellar structure.

Since the accretion luminosity does not exceed either Eddington luminosity, we conclude that for the duration of our simulation, radiation pressure is not likely to significantly change the early accretion rates we have found. At later times, when the protostar reaches higher masses, however, and in particular when it reaches the ZAMS and hydrogen burning turns on, such feedback effects will become more important, and can no longer be neglected.

2.5 Parameter Sensitivity

How commonly do Pop III stars form in multiples? To what extent does this result depend on the initial cosmological parameter values, particularly the value for σ_8? Is there a relation between the spin of a minihalo and the probability that it will host a Pop III multiple (see section 4.1)? To address this uncertainty, we make an initial estimate of the sensitivity of our results to differing values of σ_8 by comparing the specific angular momentum profile of the central 1000 $\mathrm{M}_\odot$ of our simulation with that of Abel et al. (2002) and Yoshida et al. (2006) (Fig. 2.13). The angular momentum profile for our work is taken at the point immediately before the first sink forms. Abel et al. (2002) initialized their simulation using h=0.5, $\Omega_\Lambda = 0$, $\Omega_\mathrm{B} = 0.06$ and $\sigma_8 = 0.7$. Yoshida et al. (2006) used h=0.7, $\Omega_\Lambda = 0.7$, $\Omega_\mathrm{B} = 0.04$ and $\sigma_8 = 0.9$. If the particular parameter values used in initializing our calculation made the central gas more prone to develop a flattened disk-like structure that would later fragment, this would first be apparent in an enhanced angular momentum profile. However, despite the varying initial conditions used for each of these

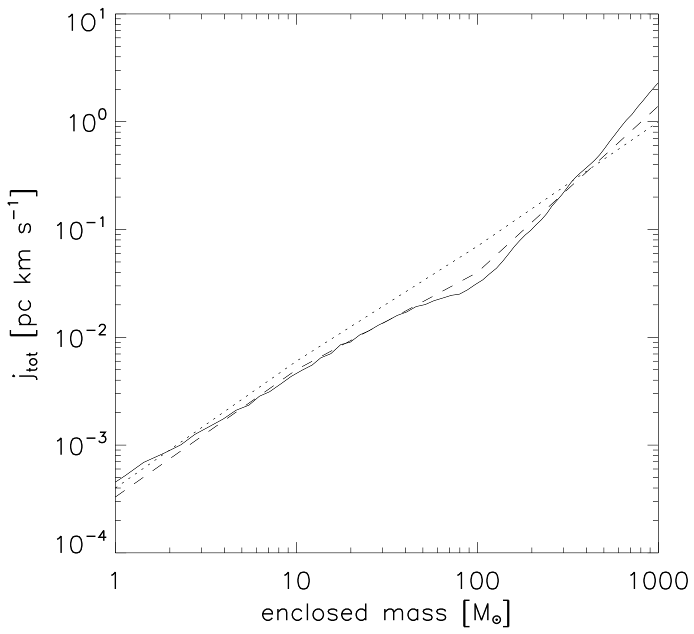

Figure 2.13: Comparison of specific angular momentum profiles for three different cosmological simulations: this work at the point immediately before initial sink formation (solid line), Yoshida et al. (2006, dotted line), and Abel et al. (2002, dashed line). Despite the differing initial conditions for each simulation, the initial angular momentum distributions are quite similar, particularly at the smallest enclosed mass scales from which most of the mass of the sinks are accreted.

calculations, the angular momentum profiles are all quite similar in shape and amplitude, especially in the innermost region. The central 100 $M_\odot$ that will later become the star-disk system in our calculation does not differ in angular momentum from the other two calculations by more than a factor of 2 to 3. In fact, in this mass range the simulation of Yoshida et al. (2006) tends to have the highest angular momentum. The initial angular momentum distribution of the star-forming gas thus seems fairly robust within the range of cosmological parameter values sampled with these three simulations, and our overall result should be correspondingly robust. We further note that Clark et al. (2008) find that their non-cosmological simulation of a primordial gas cloud also resulted in a profile very similar to the same two cosmological simulations, and upon extending their calculation through the sink particle method they also found extensive fragmentation.

However, the generality of our result will be best determined through a more comprehensive set of simulations, aiming at studying fragmentation over a range of minihalo spins. We will report on the results in a future work. Finally, we expect that the effects from protostellar feedback, neglected here, will likely dominate over those arising from variations in the initial conditions. Again, this needs to be addressed with improved simulations.

2.6 Summary and Discussion

We have evolved a cosmological simulation until a primordial minihalo has formed at $z \simeq 20$, and follow the subsequent collapse of the gas in its center up to densities of $n = 10^{12}\,\mathrm{cm}^{-3}$. We find that the initial collapse, leading to the formation of a small hydrostatic core, is very similar to previous high-resolution work. Subsequently, a disk-like structure grows around the central core, eventually comprising a mass of ~ 40 M$_{\odot}$. We use the sink particle method to study the mass flow onto the central protostar for 5000 yr after its formation. Similar to the fragmentation found in Turk et al. (2009), we find that a second protostar forms soon after the first one. Upon further evolution, the disk exhibits spiral structure and undergoes further fragmentation, resulting in several more sink particles by the end of the simulation. Most of the mass of the smaller, secondary sinks is accreted through the disk, which consists mostly of cold gas. Once the main sink grows beyond $10\,\mathrm{M}_{\odot}$, its strong gravity is able to heat the surrounding particles to several thousand Kelvin, such that a two-phase medium emerges. The main sink is able to accrete these heated particles as well. After 5000 yr of accretion, the most massive sink has reached ~ 40 M$_{\odot}$, at which point we terminate our simulation. Beyond this time, protostellar feedback effects, which are not included here, could no longer be neglected. The Pop III star, however, is expected to accumulate more mass. Even in the no-feedback case, however, the finite time available for accretion limits the Pop III mass to $\lesssim 1000\,\mathrm{M}_{\odot}$, where it is evident that in realistic settings, masses will not reach such extreme values. The accretion rate and the number of stars that form will be affected by protostellar feedback, with the likely outcome that both individual masses and the number of stars will be reduced (see Krumholz et al. 2007).

The recent radiation-hydrodynamical simulation by Krumholz et al. (2009), which studies the collapse of a massive pre-stellar core in a present-day GMC, shows interesting similarity to our investigation of the primordial case. They followed the collapse of a $100\,\mathrm{M}_{\odot}$ gas cloud, the formation of several protostellar seeds and their subsequent growth by accretion. Like our simulation, their system also evolved into a disk with a radius of order 1000 AU which fragmented due to gravitational instability. Similar to the sink mergers seen in our calculation, in their simulation the secondary stars that formed in the disk collided with the most massive star. By the end of their simulation, which was halted after $\sim$ 60,000 yr, the system had evolved into a binary with stars of mass $\sim$ 30 and 40 $M_{\odot}$, masses fairly close to those of the two largest sinks in our simulation. Their calculation, however, included dust opacity as well as radiation pressure from the stars, and their initial conditions were typical of present-day star formation. Their accretion and fragmentation timescales were also much longer than those found in our calculation, but the overall qualitative results were alike.

Thus, the formation of binary and multiple systems within disk structures is likely not limited to modern-day star formation and can be found even in the primordial case, arising from cosmological initial conditions. Binary and multiple systems may be much more common in the Pop III case than previously thought. As similarly argued in Clark et al. (2008), this is because most cosmological simulations do not follow the gas evolution for many years after the first protostar has formed, and fragmentation may not typically occur until after the simulations are stopped. For instance, the second protostar in our calculation did not form until 300 yr after the first, while the calculation of Turk et al. (2009) was stopped only 200 yr after the first protostar formed.

If Pop III binaries and multiples are actually common, then this has important implications for the final fate and observational signature of Pop III.1 stars, those zero-metallicity stars that have not yet been influenced by any previous stellar generation (e.g. Bromm et al. 2009). The presence of multiple accretors in our simulation did not seem to affect the accretion rate onto the largest sink as compared to previous work (Bromm & Loeb 2004). However, extending our simulation to later times might show that the most massive star would ultimately have to compete with its secondary companion for mass. As pointed out in Turk et al. (2009), if this in the end prevents the largest star from reaching very high masses ($\gtrsim 100$ M$_\odot$), this would also affect its resulting chemical signature. If multiple star formation were common in Pop III, then the occurrence of pair-instability supernovae (PISNe) might be significantly reduced, since stars that explode as PISNe must be in the higher mass range (140 M$_\odot$ $< M_* <$ 260 M$_\odot$, Heger and Woosley 2002). Extremely metal-poor Galactic halo stars are believed to preserve the nucleosynthetic pattern of the first SNe, so this may help to explain the lack of PISNe chemical signatures found in halo stars (e.g. Christlieb et al. 2002; Beers and Christlieb 2005; Frebel et al. 2005; Tumlinson 2006; Karlsson et al. 2008). Turk et al. (2009) also note that if multiple high-mass Pop III stars can form within a minihalo at similar times, the ionizing flux on neighboring minihalos could be increased, possibly leading to more efficient molecular cooling and ultimately lower-mass (Pop III.2) stars in the neighboring halos (e.g. O'Shea et al. 2005). This again would influence the chemical signature of extremely metal-poor Galactic halo stars.

It should be mentioned that tight binaries on scales smaller than the resolution of our simulation could also form. Though a higher resolution study would be necessary to confirm this, the formation of a fragmenting disk of steadily increasing angular momentum in our cosmological simulation makes this a reasonable possibility. This could also limit the mass of Pop III stars, yielding similar effects on their resulting chemical signature as discussed above. The possible binary nature of Pop III stars, provided that they would not grow to become very massive, may also yield a direct primordial formation pathway to carbon-enhanced metal-poor (CEMP) stars, those metal-poor halo stars with unusually high carbon abundance (e.g. Frebel et al. 2007; Tumlinson 2007). If one of the members of a Pop III binary was an intermediate-mass star ($1\ \mathrm{M}_\odot \lesssim M_* \lesssim 8\ \mathrm{M}_\odot$), then the companion might undergo carbon enhancement through binary mass-transfer (e.g. Suda et al. 2004. This would occur when the intermediate-mass star enters an asymptotic giant branch (AGB) phase during which its C-rich ejecta can be captured by the companion. Furthermore, another type of Pop III signature would arise if gamma-ray bursts (GRBs) were able to form from very tight Pop III binaries. These may be detectable by *Swift* (see Bromm and Loeb 2006; Belczynski et al. 2007).

On the other hand, if both members of a typical Pop III binary were in the mass range to collapse directly into a black hole ($M_* \gtrsim 260\ \mathrm{M}_\odot$), then they could become massive black hole (MBH) binaries. Such a population of MBH binaries may emit a gravitational wave (GW) signature detectable by the future space-born *Laser Interferometer Space Antenna (LISA)*. Previous studies have already explored the possibility of GW detection of MBH binaries formed through halo mergers during early structure formation (e.g. Wyithe and Loeb 2003; Sesana et al. 2005). Sesana et al. (2005) find that high redshift ($z \gtrsim 10$) MBH binaries with masses $\lesssim 10^3\ \mathrm{M}_\odot$ will be detectable by $LISA$. MBH binaries formed from Pop III progenitors thus approach the range of detectability by $LISA$, especially if the BHs continue to grow in mass through accretion. Furthermore, Belczynski et al. (2004) predict that advanced $LIGO$ could also detect the GWs from Pop III MBH binary mergers. Madau and Rees (2001) suggested a different type of Pop III MBH signal when they discussed how an accreting primordial MBH could tidally capture a star and become a detectable off-nuclear ultraluminous X-ray source. They conclude, however, that such a non-primordial origin to Pop III binaries is extremely inefficient.

A modified picture of Pop III star formation is thus emerging in which disk formation, fragmentation, and the resulting binary and mutiple systems will play an important role in determining the mass of Pop III stars and their influence on later star and galaxy formation. Further studies, particularly ones which include protostellar feedback, will continue to add to this developing picture.

Chapter 3

The First Stars: Mass Growth Under Protostellar Feedback

3.1 Introduction

Previous work has found that Pop III stars begin as very small protostars of initial mass $\sim 5 \times 10^{-3}$ $M_{\odot}$ (Omukai and Nishi 1998; Yoshida et al. 2008). Continued accretion onto the protostar over time ultimately leads to stars significantly larger than the initial seeds (e.g. Omukai and Palla 2003; Bromm and Loeb 2004). The final mass reached by Pop III stars therefore depends on the rate and duration of the accretion. Early numerical studies found that Pop III stars are likely to reach very high masses ($\gtrsim 100$ $M_{\odot}$; e.g. Abel et al. 2002; Bromm et al. 2002). The lack of metal and dust cooling in primordial gas leads to higher temperatures and greater accretion rates as compared to current star-forming regions such as the giant molecular clouds within the Milky Way.

The accretion history of Pop III stars depends critically on the radiative feedback exerted during their growth phase, an effect not included in the earliest three-dimensional simulations. The strength of protostellar feedback in turn hinges upon the three-dimensional structure of the surrounding gas. For instance, Omukai and Inutsuka (2002) find that for spherically symmetric accretion onto an ionizing star, the formation of an H II region in fact does not impose an upper mass limit to Pop III stars. Similarly, the analytical study by McKee and Tan (2008) found that Pop III stars can grow to greater than 100 $M_\odot$ even as a protostar's own radiation ionizes its surroundings. Although the ionization front will expand along the polar regions perpendicular to the disk, mass from the disk itself can continue to accrete onto the star until this is halted through photoevaporation. Recent studies of present-day star formation also support the picture that stars can reach very high masses through disk accretion. For instance, numerical studies by Krumholz et al. (2009) and Kuiper et al. (2011) both find that strong feedback from radiation pressure will not halt mass flow through the stellar disk before the star has reached $\gtrsim 10$ $M_\odot$. The final stellar masses are likely even greater, though the simulations were not followed for sufficiently long to determine this. There is also growing observational evidence that massive star-forming regions exhibit disk structure and rotational motion (e.g. Cesaroni et al. 2007; Beuther et al. 2009).

Meanwhile, the picture of a single massive Pop III star forming in a minihalo has been complicated by more recent work. Simulations by Clark et al. (2008, 2011a) employing idealized initial conditions found that primordial star-forming gas can undergo fragmentation to form Pop III multiple systems, while the simulations of Turk et al. (2009) and Stacy et al. (2010) established such fragmentation also when initialized on cosmological scales. Further work revealed that gas fragmentation can occur even on very small scales (~ 10 AU) and in the majority of minihalos, if not nearly all (Clark et al. 2011b, Greif et al. 2011). These studies tentatively imply that the typical Pop III mass may be somewhat lower than ~ 100 $M_\odot$. Smith et al. (2011) recently found that, even under feedback from protostellar accretion luminosity, such fragmentation may be reduced but not halted. While Smith et al. (2011) included a heating term derived from the accretion luminosity, they did not explicitly account for molecular photodissocation by Lyman-Werner (LW) radiation from the protostar, and they did not include the effects of ionizing radiation that will become important once the stars have grown to larger masses ($\gtrsim 10\,\mathrm{M}_{\odot}$).

Whether Pop III stars can attain very large masses under feedback and while within a multiple system is pivotal to understanding their potential for large-scale feedback effects, such as the suppresion or enhancement of the star-formation rate in neighboring minihalos. It also determines whether they may be observed as gamma-ray bursts (GRBs) or extremely energetic PISNe (e.g. Bromm and Loeb 2002, 2006; Gou et al. 2004; Belczynski et al. 2007; Stacy et al. 2011). Furthermore, the fragmentation seen in recent work, along with the possible ejection of low-mass Pop III stars from their host star-forming disks (e.g. Greif et al. 2011; Smith et al. 2011), opens the possibility that small, long-lived Pop III stars may still be observed today. This depends, however, on uncertain factors such as the final masses reached by the ejected stars and the amount of metal-enriched material accreted at later times while being incorporated into larger galaxies, which could mask the stars as Pop II (e.g. Frebel et al. 2009; Johnson and Khochfar 2011).

To further explore the range of masses possible for Pop III stars, we perform a cosmological simulation to study the feedback effects of a protostar on its own accretion and on further fragmentation within its host minihalo. We initialize the simulation with sufficient resolution to follow the evolution of the star-forming gas up to densities of 10^{12} cm^{-3}. At this density we employ the sink particle method, allowing us to study the subsequent disk formation and fragmentation of the gas over the following $\sim$ 5000 yr. We include H_2 dissociating LW feedback from the most massive star in the simulation, and we use a ray-tracing scheme to follow the growth of the star's H II region once it has become massive enough to ionize the surrounding gas. We compare this to a simulation with the same initialization but no radiative feedback. This allows for a direct evaluation of how radiative feedback alters the mass growth of Pop III stars, the rate of disk fragmentation, and the formation of additional stars within the disk. We describe our numerical methodology in Chapter 3.2, while in Chapter 3.3 we present our results. We conclude in Chapter 3.4.

3.2 Numerical Methodology

3.2.1 Initial Setup

We ran our simulation using GADGET 2, a widely-tested three-dimensional N-body and SPH code (Springel 2005). We initialized our simulation using a snapshot from the previous simulation of Stacy et al. (2010). In particular, we chose the snapshot in which the dense gas in the center of the minihalo has first reached 10^8 cm^{-3}. This simulation was originally initialized at $z = 100$ in a periodic box of length 140 kpc (comoving) using both SPH and DM particles. This was done in accordance with a ΛCDM cosmology with $\Omega_\Lambda = 0.7$, $\Omega_\mathrm{M} = 0.3$, $\Omega_\mathrm{B} = 0.04$, and $H_0 = 70$ km s^{-1} Mpc^{-1}. To accelerate structure formation, we used an artificially enhanced normalization of the power spectrum, $\sigma_8 = 1.4$. As discussed in Stacy et al. (2010), we verified that the density and velocity fields in the center of the minihalo closely resembled those in previous simulations. We furthermore found that the angular momentum profile of the minihalo gas immediately before initial sink formation was very similar to the cosmological simulations of Abel et al. (2002) and Yoshida et al. (2006), despite their lower values of σ_8 (0.7 and 0.9, respectively).

The high resolution of our simulation was achieved through a standard hierarchical zoom-in procedure (see Stacy et al. 2010 for more details). We added three additional nested refinement levels of 40, 30, and 20 kpc (comoving), centered on the location where the first minihalo will form. At each level of refinement, we replaced every 'parent' particle with eight 'child' particles, such that at the highest refinement level each parent particle has been replaced with 512 child particles. The highest-resolution gas particles have a mass $m_{\rm SPH} = 0.015$ $\mathrm{M}_{\odot}$, so that the mass resolution is $M_{\rm res} \simeq 1.5 N_{\rm neigh} m_{\rm SPH} \lesssim 1$ $\mathrm{M}_{\odot}$, where $N_{\rm neigh} \simeq 32$ is the typical number of particles in the SPH smoothing kernel (e.g. Bate and Burkert 1997).

3.2.2 Chemistry, Heating, and Cooling

We use the same chemistry and cooling network as described in Greif et al. (2009). The code follows the abundance evolution of H, H^{+}, H^{-}, H_2, H_2^{+}, He, He^{+}, He^{++}, and e^{-}, as well as the three deuterium species D, D^{+}, and HD. All relevant cooling mechanisms are accounted for, including H_2 cooling through collisions with He and H atoms and other H_2 molecules. Also included are cooling through H and He collisional excitation and ionization, recombination, bremsstrahlung, and inverse Compton scattering. We finally note that H_2 cooling through collisions with protons and electrons is included, as they play an important role within H II regions (Glover and Abel 2008).

One important difference we note between the high density ($n \gtrsim 10^9$ cm^{-3}) evolution in the current simulation and that of Stacy et al. (2010) is that we here account for the optical thickness of the H_2 ro-vibrational lines, which reduces the effectiveness of these lines in cooling the gas. We include this effect using the Sobolev approximation (see Yoshida et al. 2006; Greif et al. 2011 for more details).

3.2.3 Sink Particle Method

When an SPH particle reaches a density of $n_{\rm max} = 10^{12}$ cm^{-3}, we convert it to a sink particle. If a gas particle is within the accretion radius $r_{\rm acc}$ of the sink, and if it is not rotationally supported against infall onto the sink, the sink accretes the particle. The sink thus accretes the particles within its smoothing kernel immediately after it first forms. We check for rotational support by comparing the angular momentum of the nearby gas particle, $j_{\rm SPH} = v_{\rm rot}d$, with the angular momentum required for centrifugal support, $j_{\rm cent} = \sqrt{GM_{\rm sink}r_{\rm acc}}$, where $v_{\rm rot}$ and d are the rotational velocity and distance of the particle relative to the sink. If a gas particle satisfies both $d < r_{\rm acc}$ and $j_{\rm SPH} < j_{\rm cent}$, it is removed from the simulation, and the mass of the accreted particle is added to that of the sink.

Our sink accretion algorithm furthermore allows for the merging of two sink particles. We use similar criteria for sink particle merging as for sink accretion. If the smaller, secondary sink is within $r_{\rm acc}$ of the more massive sink and has specific angular momentum less than $j_{\rm cent}$ of the larger sink, the sinks are merged. After an accretion or merger event, the position of the sink is set to the mass-weighted average of the sink's former position and that of the accreted gas or secondary sink. The same is done for the sink velocity. We note that, as discussed in Greif et al. (2011), modifications to the sink merging alogorithm can significantly alter the sink accretion history. Future work will include studies of how a different technique for sink merging would modify our results.

We set the accretion radius equal to the resolution length of the simulation, $r_{\rm acc} = L_{\rm res} \simeq 50$ AU, where

$$L_{\rm res} \simeq 0.5 \left(\frac{M_{\rm res}}{\rho_{\rm max}} \right)^{1/3} \quad ,$$

with $\rho_{\rm max} \simeq n_{\rm max} m_{\rm H}$ and $m_{\rm H}$ being the proton mass. The sink particle's mass, $M_{\rm sink}$, is initially close to the resolution mass of the simulation, $M_{\rm res} \simeq 0.7$ $\mathrm{M}_{\odot}$. Sink particles are held at a constant density and temperature of $n_{\rm max} = 10^{12}$ cm^{-3} and 650 K, such that their pressure is also kept to the corresponding value. Providing the sink with a temperature and pressure prevents the existence of a pressure deficit around the sink, which would otherwise lead to artificially high accretion rates (e.g. Bate et al. 1995; Bromm et al. 2002; Martel et al. 2006). The sink particles do continue to evolve in position and velocity, however, through gravitational and hydrodynamic interactions.

As discussed in Bromm et al. (2002) and Stacy et al. (2010), our sink formation criteria well represent regions that will truly collapse to stellar densities. Before crossing the density threshold to become a sink, a gas particle must collapse two orders of magnitude above the average disk density, $\simeq 10^{10}$ cm^{-3}. Our high density threshold and small value for $r_{\rm acc}$ ensure that sinks are formed only from gravitationally collapsing gas.

Following the long-term evolution of the star-forming gas would not be feasible without the sink particle method. By preventing gas evolution to ever higher densities, we avoid the problem of increasingly small numerical timesteps, a problem also known as 'Courant myopia.' We thus are able to see how the surrounding region of interest evolves over many dynamical times. With sink particles, we can furthermore bypass the need to incorporate the chemistry, hydrodynamics and radiative transfer that comes into play at extremely high densities ($n > 10^{12}$ cm^{-3}). Finally, sink particles provide a convenient way to directly measure the accretion rate onto the protostellar region.

3.2.4 Ray-tracing Scheme

Once the first sink is formed, this particle is used as the source of protostellar LW and ionizing radiation. While the protostar is less massive than 10 $M_\odot$, LW radiation is the only source of feedback. After the protostar is massive enough to emit ionizing radiation, however, a compact H II region develops. We model the growth of the surrounding I-front using a ray-tracing scheme which closely follows that of Greif et al. (2009). A spherical grid with $\sim 10^5$ rays and 200 radial bins is then created around the sink particle. The minimum radius is determined by the distance between the sink and its closest neighboring SPH particle, and we update this structure each time the ray-tracing is performed. Because the sink accretes most particles within $r_{\rm acc} = 50$ AU, the minimum radius is usually $\gtrsim 50$ AU. The maximum radius is chosen as 14 kpc (physical), a value that easily encompasses the entire H II region in our simulation. The radial bins within 75 AU of the minimum radius are spaced at intervals of 1.5 AU. Outside this distance the bins are logarithmically spaced. The location of each particle is then mapped onto the corresponding bin within the spherical grid, and each particle contributes its density and chemical abundances to the bin proportional to its density squared.

Next, the ionization front equation is solved along each ray:

$$n_n r_{\rm I}^2 \frac{{\rm d}r_{\rm I}}{{\rm d}t} = \frac{\dot{N}_{\rm ion}}{4\pi} - \alpha_{\rm B} \int_0^{r_{\rm I}} n_e n_+ r^2 {\rm d}r \ , \tag{3.1}$$

where n_n, n_e, and n_+ are the number densities of neutral particles, electrons, and positively charged ions, respectively. The location of the ionization front with respect to the sink is denoted by $r_{\rm I}$. $\dot{N}_{\rm ion}$ is the number of ionizing photons emitted per second, and $\alpha_{\rm B}$ is the case B recombination coefficient. We use $\alpha_{\rm B} = 1.3 \times 10^{-12}$ cm^3 s^{-1} for He III recombinations to He II, and $\alpha_{\rm B} = 2.6 \times 10^{-13}$ cm^3 s^{-1} for He II and H II recombinations to the ground state (Osterbrock and Ferland 2006).

The emission rate of H I, He I and He II ionizing photons is given by

$$\dot{N}_{\rm ion} = \frac{\pi L_*}{\sigma_{\rm SB} T_{\rm eff}^4} \int_{\nu_{\rm min}}^{\infty} \frac{B_\nu}{h\nu} {\rm d}\nu \ , \tag{3.2}$$

where h is Planck's constant, $\sigma_{\rm SB}$ the Stefan-Boltzmann constant, and $\nu_{\rm min}$ the minimum frequency required for ionization of the relevant species (H I or He II). For simplicity we do not distinguish between the H II and He II regions. We assume the sink emits a blackbody spectrum B_ν with an effective temperature $T_{\rm eff}$, which depends upon the evolving stellar radius and luminosity.

As described in Greif et al. (2009), the integral on the right-hand side of the ionization front equation is discretized by the following sum:

$$\int_0^{r_{\rm I}} n_e n_+ r^2 {\rm d}r \simeq \sum_i n_{e,i} n_{+,i} r_i^2 \Delta r_i \ , \tag{3.3}$$

where Δr_i is the radial extent of each bin i, and the sum ranges from the sink particle to the current position of the I-front. The left hand side of the ionization front equation is similarly discretized by:

$$n_n r_{\rm I}^2 \frac{{\rm d}r_{\rm I}}{{\rm d}t} \simeq \frac{1}{\Delta t} \sum_i n_{n,i} r_i^2 \Delta r_i \ , \tag{3.4}$$

where the sum now extends from the I-front position at the previous timestep t_0 to its position at the current timestep $t_0 + \Delta t$. The above-described ray-tracing is performed separately for the H II and He III regions.

3.2.5 Photoionization and Heating

Particles determined to be within the extent of the H II and He III regions are given additional ionization and heating rates in the chemistry solver:

$$k_{\rm ion} = \int_{\nu_{\rm min}}^{\infty} \frac{F_\nu \sigma_\nu}{h\nu} {\rm d}\nu \tag{3.5}$$

and

$$\Gamma = n_n \int_{\nu_{\rm min}}^{\infty} F_\nu \sigma_\nu \left(1 - \frac{\nu_{\rm min}}{\nu}\right) {\rm d}\nu \ , \tag{3.6}$$

where F_ν is the incoming specific flux and σ_ν the photo-ionization cross section. For a blackbody, we have

$$F_\nu = \frac{L_*}{4\sigma T_{\rm eff}^4 r^2} B_\nu \ , \tag{3.7}$$

where r is the distance from the sink.

Finally, H_2 dissociation by LW radiation (11.2 to 13.6 eV) is described by

$$k_{\rm H_2} = 1.1 \times 10^8 \, f_{\rm shield} \, F_{\rm LW} \ {\rm s}^{-1} \tag{3.8}$$

(Abel et al. 1997), where $F_{\rm LW}$ denotes the radiation flux, in units of erg s^{-1} cm^{-2} Hz^{-1}, at $h\overline{\nu} = 12.87$eV, and $f_{\rm shield}$ is the factor by which H_2 self-shielding reduces the LW dissociation rate. This self-shielding factor depends upon the H_2 column density N_{H_2}. With the above ray-tracing scheme, we determine N_{H_2} along each ray by summing the contribution from each bin. We then use results from Draine and Bertoldi (1996) to determine the value for $f_{\rm shield}$. We note a recent update to their $f_{\rm shield}$ fitting formula (Wolcott-Green et al. 2011; Wolcott-Green and Haiman 2011), but do not expect this to significantly affect the results for our particular case. Because of the unusually high column densities within the molecular disk ($N_{H_2} \gtrsim 10^{26}$ cm^{-2}), we calculate $f_{\rm shield}$ using equation 37 from Draine and Bertoldi (1996), which is more accurate for large N_{H_2} than their simple power-law expression in their equation 36.

These heating, ionization, and dissociation rates are accounted for at every timestep, while the ray-tracing procedure is performed every fifth timestep. The rates are updated every 10 yr as they evolve with the protostellar mass and accretion rate, because these determine the values of L_* and $T_{\rm eff}$.

3.2.6 Protostellar evolution model

Our ray-tracing algorithm requires an input of protostellar effective temperature $T_{\rm eff}$ and luminosity L_*. This is the sum of $L_{\rm acc}$, the accretion luminosity, and $L_{\rm photo}$, the luminosity generated at the protostellar surface:

$$L_* = L_{\rm acc} + L_{\rm photo} = \frac{GM_*\dot{M}}{R_*} + L_{\rm photo}, \tag{3.9}$$

where M_* is the protostellar mass, $\dot{M}$ the accretion rate, and R_* the protostellar radius. The photospheric luminosity is either due to Kelvin Helmholtz

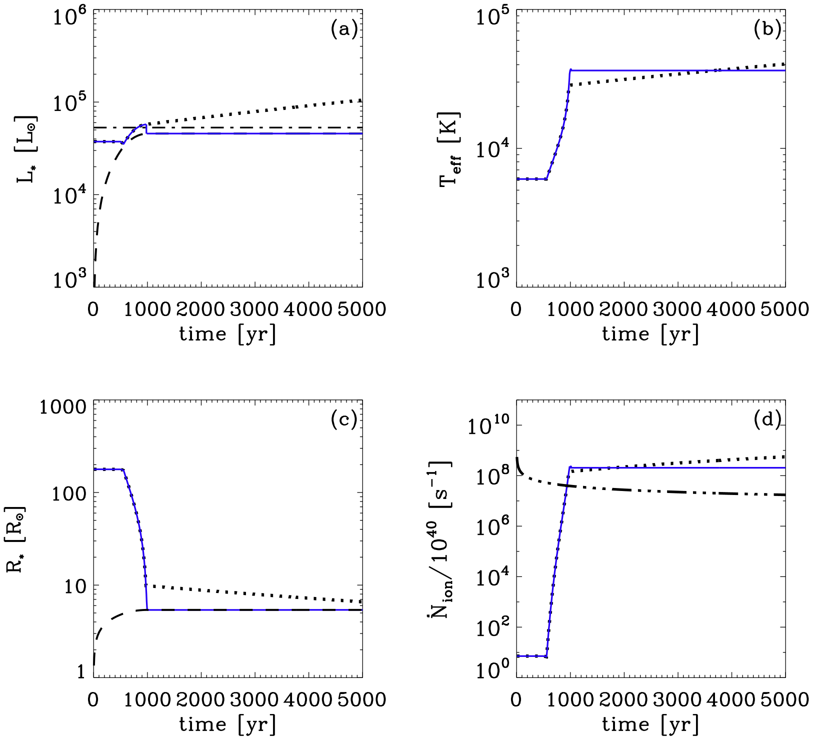

Figure 3.1: Evolution of various properties of the growing protostar according to our analytical model. Solid blue lines represent the protostellar values used in our 'with-feedback' simulation. Dashed lines represent the ZAMS stellar values for the current sink mass. Dotted lines represent the 'slow contraction' case in which the accretion rate initially evolves in the same fashion as in the 'with-feedback' simulation, but then holds steady at 10^{-3} $\mathrm{M}_\odot$. *(a):* Protostellar luminosity. Dash-dotted line is the estimate for L_{KH} of a 15 $\mathrm{M}_\odot$ star of radius 10 $\mathrm{R}_\odot$. *(b):* Effective temperature. *(c):* Protostellar radius. *(d):* Ionizing luminosity, $\dot{N}_{\mathrm{ion}}$. Dashed-triple-dotted line represents the accretion rate of neutral particles onto the sink, extrapolated from the powerlaw fit to sink accretion rate over the first 500 years ($\dot{M} \propto t_{\mathrm{acc}}^{0.56}$, see Chapter 3.3.4). Note how the ZAMS values used after 1000 years in our simulation yield a good approximation to the more physically realistic 'slow-contraction' case. Both also predict a break-out of ionizing radiation beyond the sink just before 1000 yr, when $\dot{N}_{\mathrm{ion}}$ exceeds the influx of neutral particles.

(KH) contraction, or due to hydrogen burning which begins once the protostar has reached the zero-age main sequence (ZAMS). For simplicity, we set $L_{\rm photo} \simeq L_{\rm ZAMS}$, thus assuming a robust upper limit in the luminosity at later phases in the protostellar evolution. Initially, however, we assume no contribution from $L_{\rm photo}$ until R_* reaches the ZAMS radius. This is a reasonable assumption, particularly given the values of $L_{\rm photo}$ as determined by, e.g., Hosokawa et al. (2010). We find that $L_{\rm acc}$ should be much greater or similar in magnitude to $L_{\rm photo}$ until the ZAMS is reached in our model (see Fig. 3.1). Our assumption is also robust in view of uncertainties regarding how rapidly KH contraction proceeds. While Hosokawa et al. (2010) find that a massive (~ 10 M$_{\odot}$) accreting protostar will typically contract to the ZAMS radius on timescales of $\sim 10^4$ yr, in our model we set our protostar to the ZAMS values much earlier. However, the luminosity during KH contraction is indeed similar in magnitude to $L_{\rm ZAMS}$ for a star of the same mass (Hosokawa et al. 2010). Nevertheless, it is important that future simulations self-consistently couple protostellar evolution and accretion flow under feedback.

As in Schaller et al. (1992) and Hosokawa et al. (2010), we determine $L_{\rm ZAMS}$ using a simple fit to the stellar mass:

$$L_{\rm ZAMS} = 1.4 \times 10^4 {\rm L}_{\odot} \left(\frac{M_*}{10 {\rm M}_{\odot}} \right)^2 \ . \tag{3.10}$$

Each time L_* is updated, we assume M_* is equal to the sink mass. Due to the discrete nature of sink accretion in an SPH simulation, instead of calculating $\dot{M}$ at each timestep, we determine $\dot{M}$ by averaging the sink mass growth over the previous 100 yr, updating $\dot{M}$ every 10 yr.

We estimate R_* in the same fashion as in Stacy et al. (2010), which was based on the prescription of Omukai and Palla (2003). We find that during the adiabatic accretion phase, R_* grows as

$$R_{*I} \simeq 50\mathrm{R}_\odot \left(\frac{M_*}{\mathrm{M}_\odot}\right)^{1/3} \left(\frac{\dot{M}}{\dot{M}_{\mathrm{fid}}}\right)^{1/3} , \tag{3.11}$$

where $\dot{M}_{\mathrm{fid}} \simeq 4.4 \times 10^{-3} \mathrm{M}_\odot\,\mathrm{yr}^{-1}$ is a fiducial rate, typical for Pop III accretion. Throughout this phase, we assume there is not yet any contribution from L_{photo}. During the subsequent phase of KH contraction, the radius will shrink according to

$$R_{*II} \simeq 140\mathrm{R}_\odot \left(\frac{\dot{M}}{\dot{M}_{\mathrm{fid}}}\right) \left(\frac{M_*}{10\mathrm{M}_\odot}\right)^{-2} . \tag{3.12}$$

We estimate that the transition from adiabatic accretion to KH contraction occurs when the value of R_{*II} falls below that of R_{*I}. During this phase, our model again assumes no luminosity contribution from L_{photo}, and that L_{acc} is the main contribution to the luminosity. KH contraction will halt once the star has reached the ZAMS, at which point we set R_* equal to the ZAMS radius,

$$R_{\mathrm{ZAMS}} = 3.9\mathrm{R}_\odot \left(\frac{M_*}{10\mathrm{M}_\odot}\right)^{0.55} \tag{3.13}$$

(e.g. Hosokawa et al. 2010). We set R_* equal to R_{ZAMS} when the value for R_{*II} falls below R_{ZAMS}.

If the calculated accretion rate drops to near zero, then the radial values for the adiabatic and KH contraction phases will become vanishingly small. If this occurs before the sink has been accreting for a KH time and reached the ZAMS, the accretion rate is set to the previous non-zero value in order to get more realistic values for R_{*I} and R_{*II}. This allows us to avoid setting $R_* = R_{\rm ZAMS}$ too early in the protostar's evolution. If, however, the accretion slows after the sink has been in place for more than its KH time, we assume the star has reached its ZAMS radius, and we set $L_{\rm acc} = 0$, $R_* = R_{\rm ZAMS}$, and $L_* = L_{\rm ZAMS}$. Note that typical KH times, where $t_{\rm KH} = GM_*^2/R_*L_*$, range from 1000 yr for a large and rapidly accreting 10 $\mathrm{M}_\odot$ protostar (see e.g. Hosokawa et al. 2010) to $\sim 4 \times 10^4$ yr for a 15 $\mathrm{M}_\odot$ main sequence star. The typical KH luminosity for a 15 $\mathrm{M}_\odot$ star is $L_{\rm KH} \sim 5 \times 10^4$ $\mathrm{L}_\odot$ (see Fig. 3.1).

Given our averaging scheme in which a minimum of one 0.015 $\mathrm{M}_\odot$ gas particle can be accreted over 100 years, this gives an effective minimum measurable accretion rate of 1.5×10^{-4} $\mathrm{M}_\odot$ yr^{-1}. However, for $M_* \gtrsim 10$ $\mathrm{M}_\odot$, this minimum accretion rate still yields a value of R_{*II} that is smaller than $R_{\rm ZAMS}$. In this case, we again set the protostellar luminosity and radius to its ZAMS values once the accretion rate has dropped to near-zero. In our case, the measured accretion rate drops very quickly after 500 yr. At this point the star has reached 15 $\mathrm{M}_\odot$, is still undergoing adiabatic expansion, and has $t_{\rm KH} \sim 1000$ yr. The star then begins rapid KH contraction until the measured accretion rate becomes zero at 1000 yr. Though within the simulation we set $L_* = L_{\rm ZAMS}$ as soon as the averaged accretion rate is zero, in reality the protostar is better described by a more gradual approach to $R_{\rm ZAMS}$. In Figure 3.1 we show the protostellar values used in the simulation along with a more realistic 'slow-contraction' model which follows the same accretion history as the 'with-feedback' case until reaching an asymptotic growth rate of 10^{-3} $\mathrm{M}_\odot$ yr^{-1}. The 'slow-contraction' model is then held at this rate, which is similar to the fiducial value used in Equation 11, and is also the typical accretion rate found at late times in our ‘no-feedback case’ as well as the simulations of, e.g., Greif et al. (2011); Smith et al. (2011). This model well-matches the prescription used in the simulation, particularly in effective temperature and ionizing luminosity, and both predict that ionizing radiation will exceed the influx of neutral particles, and that break-out beyond the sink occurs at $\lesssim$ 1000 yr. Though the protostar most likely does not reach the ZAMS within the time of our simulation, our simple model serves as a reasonable approximation for any unresolved accretion luminosity. We also note that Hosokawa et al. (2010) find that, for a given accretion rate, primordial protostars undergoing disk accretion will have considerably smaller radii than those accreting mass in a spherical geometry. The rapid contraction of the protostar between 500 and 1000 years therefore serves as an idealized representation of the sub-sink material evolving from a spherical to a disk geometry as it gains angular momentum.

As discussed in Smith et al. (2011), the sink particle method requires several simplifying assumptions when constructing the protostellar model. By setting the protostellar mass equal to the sink mass, we are assuming that the small-scale disk which likely exists within the sink region has low mass compared to the protostar. We also assume that the accretion rate at the sink edge is the same as the accretion rate onto the star, when in reality after gas enters within $r_{\rm acc}$ it must likely be processed through a small-scale disk before being incorporated onto the star. However, our assumption may still be a good approximation of physical reality, given that the primordial protostellar disk study of Clark et al. (2011b) implies that the thin disk approximation would probably not be valid on sub-sink scales (e.g. Pringle 1981), and that strong gravitational torques can quickly drive mass onto the star. Furthermore, as also pointed out in Smith et al. (2011), our averaging of the accretion rate over a number of timesteps serves to mimic the buffering of accreted material by the sub-sink disk. The inputs to our protostellar model are thus necessarily approximate, as is the protostellar model itself. Nevertheless, it is sufficient to provide an exploratory picture of how ionizing feedback will affect Pop III accretion within a cosmological setup.

3.3 Results

3.3.1 Disk Evolution

The gas in both the 'no-feedback' and 'with-feedback' cases underwent disk formation, fragmentation, and the emergence of several sinks. We show the evolution of various disk properties in Figure 3.2. Because of the imprecision involved in determining which gas particles comprise the disk, for simplicity we define the disk as consisting of particles with number density greater than 10^9 cm^{-3} and with an H_2 fraction greater than 10^{-3}. This way the disk only contains cool and dense gas that has not been subject to ionization or significant H_2 destruction. From Figure 3.3 we see that the disk structure is growing in mass well before the first sink forms. This central gas is already rotationally dominated, as indicated by the low values of $\chi_{\rm rad}$ in Figure 3.2, which is the average radial velocity of the gas particles divided by their average rotational velocity, $\chi_{\rm rad} = v_{\rm rad}/v_{\rm rot}$. Velocities are measured with respect to the center of mass of the disk.

3.3.1.1 No-feedback case

After sink formation, the 'no-feedback' disk steadily grows in mass (Fig. 3.3) as angular momentum causes it to expand in radius and become somewhat

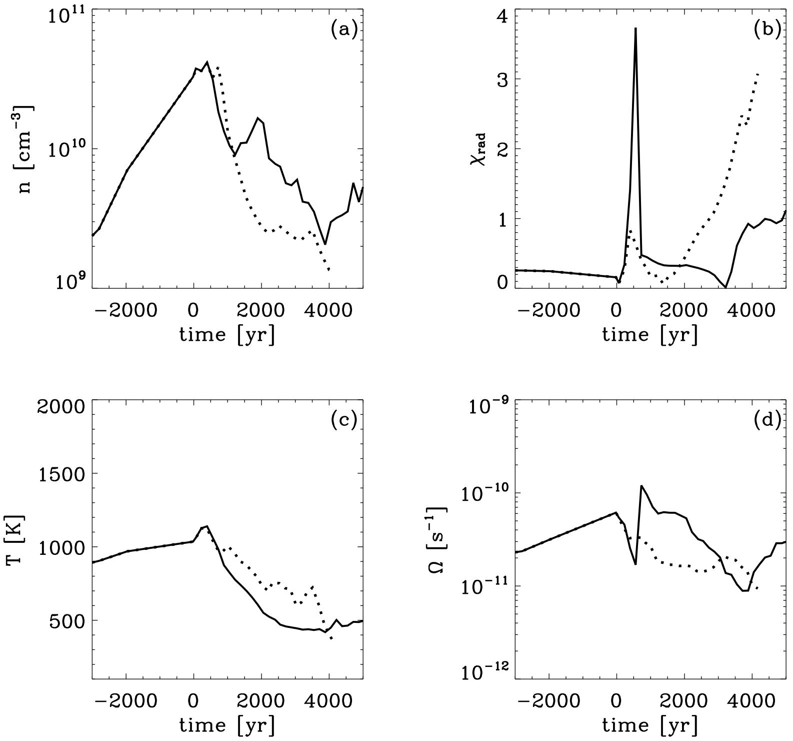

Figure 3.2: Evolution of various disk properties. Time is measured from the point at which the first sink particle forms. In each case, solid lines represent the 'no-feedback' case while the dotted lines denote the 'with-feedback' case. *(a):* The average density of the gas within the disk. *(b):* The average ratio of radial to rotational velocity of the disk particles, χ_{rad}. *(c):* The average temperature of the disk particles. *(d):* The average angular velocity of the disk gas with respect to the disk center of mass, Ω. Note how the 'with-feedback' and 'no-feedback' cases diverge after 1000 yr.

lower in average density (panel *a* in Fig. 3.2). The disk growth is halted at nearly 2000 yr due to its gradual disruption through N-body dynamics of the sinks. One of the sinks is ejected at $\sim$ 500 yr, after growing to only ~ 1 M$_\odot$. The ejection occurs immediately following the merger of the two other sinks, at a time when the three sinks are close together in the center of the disk and subject to N-body dynamics. The sink accretes no more mass after its ejection. It initially moves in a direction perpendicular to the disk plane at $\sim$ 5 km s^{-1} with respect to the disk center of mass, and the maximum distance between the two sinks approaches 3000 AU at approximately 2500 yr. This increase in distance between the two sinks is mostly due to the motion of the main sink, however. In this N-body interaction, the main sink gains a larger velocity, initially moving with respect to the disk center of mass at $\sim$ 10 km s^{-1}. It travels parallel to the disk plane and pulls the disk along with it. The rapid motion of the main sink disrupts the high-density gas, which transforms from a disk structure to a more diffuse tidal tail, eventually causing the total measured disk mass to slightly decrease (Fig. 3.3). The rotational structure is also disturbed, as indicated by a peak in $\chi_{\rm rad}$ when the sink is ejected. After approximately 3000 yr, the tidal tail begins to recompress, causing the dense gas to be more dominated by radially inward motion. This is indicated by the increase of $\chi_{\rm rad}$ to ~ 1 as well as an increase in the average disk density (Fig. 3.2).

From the solid red line in Figure 3.3, we also note a smooth early growth of hot dense gas over the first 1000 yr. This begins almost as soon as the first sink is formed, and the main sink thus provides an early source of heating. This occurs as the gravitational potential of the sink, which grows to > 10 M$_\odot$ in only 200 yr, heats the surrounding gas up to $\sim$ 7000 K, or $c_{\rm s} \simeq 7$ km s^{-1}

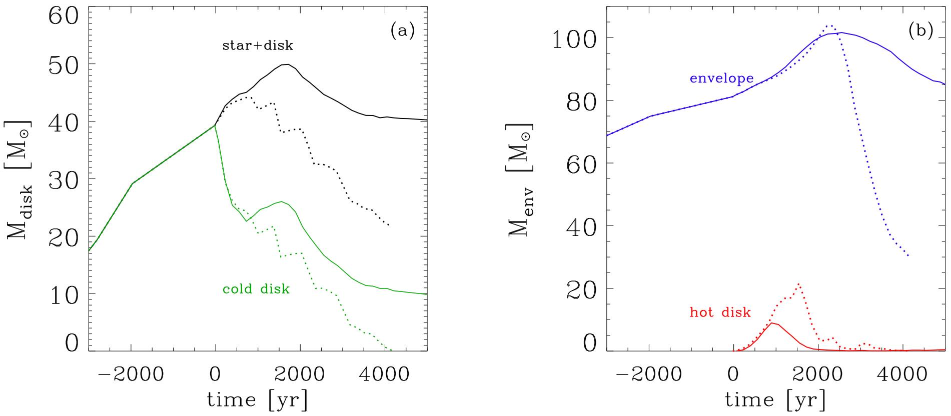

Figure 3.3: Evolution of disk mass over time. Solid lines are for the 'no-feedback' case. Dotted lines represent the 'with-feedback' case. *(a):* Black lines show the mass of the total star-disk system. Disk mass (green lines) is taken as dense ($n > 10^9$ cm $^{-3}$) gas with an H_2 fraction greater than 10^{-3}. *(b):* Red lines show the mass of hotter, non-molecular material in the same density range as the disk, and blue lines denote the total mass of the outer envelope, which is defined as comprising all $n > 10^8$ cm $^{-3}$ gas. Note how radiative feedback greatly reduces the total disk and envelope mass after approximately 1000 and 2000 yr.

(Fig. 3.4), corresponding to approximately the virial temperature of the sink:

$$T_{\rm vir} \simeq \frac{GM_{\rm sink}m_{\rm H}}{k_{\rm B}r_{\rm acc}} \simeq 10^4\,{\rm K}.$$

The mass of hot dense gas undergoes an equally smooth decline over the next 1000 yr in the 'no-feedback' case. A minimal amount of dense gas is newly heated after 1000 yr because there is no longer a dense disk structure entirely surrounding the main sink. Most of the dense gas instead trails behind the sink in the tidal tail, and the gravitational heating provided by the sink is now imparted directly to the lower-density particles. Sink gravitational heating thus halts the growth of the outer envelope, which we define to include all gas particles at densities above 10^8 cm^{-3} as well as the sinks (solid blue line in Fig. 3.3). The 'heat wave' travels beyond the disk at approximately the sound speed, causing the decline in envelope mass beginning at around 2500 yr in Figure 3.3, and reaching distances of > 7000 AU (see Figs. 3.4 and 3.5) by the end of the simulation. At this time, heated gas thus resides almost entirely at low densities ($n < 10^9$ cm^{-3})

This disk and envelope evolution resembles that in Stacy et al. (2010), particularly in that early gravitational heating by the sink caused the development of a phase of hot and dense gas. However, the hot phase in Stacy et al. (2010) lied mostly between densities of 10^8 and 10^{12} cm^{-3}, and the mass of both the envelope and total star-disk system showed a steady increase throughout the simulation. In contrast, in our current 'no-feedback' case, the hot phase lies mostly between densities of 10^6 and 10^9 cm^{-3}, and both the disk and envelope decline in mass after 2000 yr. This difference between simulations ultimately arises from the statistical variation in sink N-body dynamics, and the corresponding response from the surrounding gas.

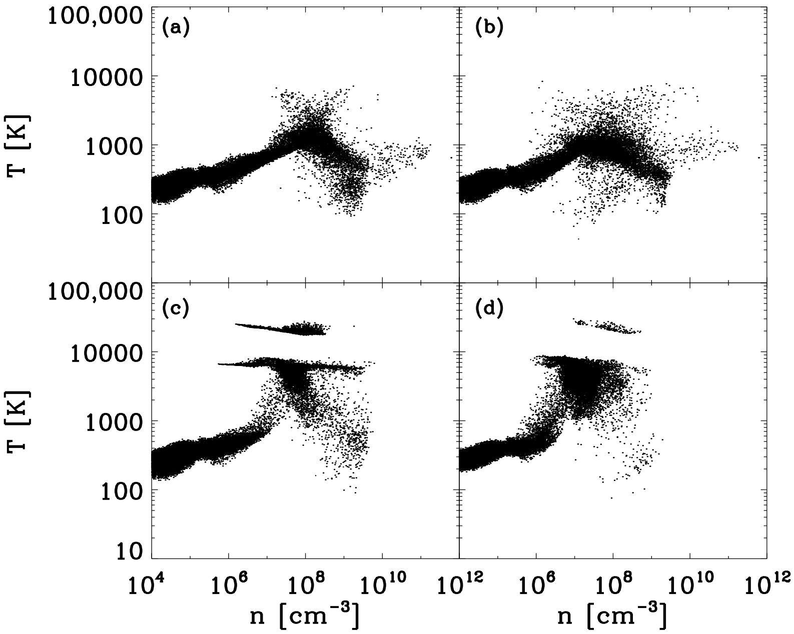

Figure 3.4: Temperature versus number density for both cases at various times in the simulations. *(a):* 'No-feedback' case at 2500 yr. *(b):* 'No-feedback' case at 5000 yr. *(c):* 'With-feedback' case at 3000 yr. *(d):* 'With-feedback' case at 4000 yr. Note how, in the 'no-feedback' case, there is only a light stream of particles with $n > 10^9$ cm^{-3} that is accreting onto the main sink. The gravitational potential well of the main sink leads to the heating of a growing region of lower-density gas. In the 'with-feedback' case, there is an expanding ionized region with temperature of 20,000 K along with a larger region of hot neutral gas with temperature of several thousand Kelvin.

3.3.1.2 With-feedback case

The ‘with-feedback’ case also exhibits a peak in $\chi_{\rm rad}$ coincident with the period of rapid sink formation, with a maximum of three sinks in the disk at any given time. This causes the disk to be dominated by N-body dynamics and disrupts the rotational structure, but without ejection of any sink. However, the disk growth is soon slowed by a different mechamism than that in the ‘no-feedback’ case. Just as in the latter, we also note a smooth early growth in the mass of hot dense gas (Fig. 3.3), initially sourced by the gravitational potential of the main sink. Once the sink is large enough to emit ionizing radiation, after $\sim$ 700 yr of accretion, infalling mass that would otherwise be incorporated into the disk is instead heated to become a hot neutral shell of several thousand Kelvin enclosing a smaller ionized bubble around the disk (see bottom panels of Fig. 3.4 and Fig. 3.6). This leads to the continued increase in the mass of the hot dense gas apparent in Figures 3.3 and 3.6 beyond that seen in the ‘no-feedback’ case. As the ionization front and hot neutral region expand and rarefy the gas, both the disk and hot dense regions lose mass. This is visible as a steep drop in mass at 1500 yr in Figure 3.3, once the hot pressure wave has reached beyond the dense region into $n < 10^9$ cm^{-3} gas. Throughout this early disk evolution, the total mass of the outer envelope steadily increases (red line in Fig. 3.3) until the same pressure wave passes through the edge of the envelope after 2000 yr.

At the same time, angular momentum causes the disk to expand in radius, making the disk more diffuse (see panel *a* of Fig. 3.2). The early steep decline in average disk density after the sink first forms is more pronounced than in the ‘no-feedback’ case due to the concurrent decline of the disk mass. Once the hot pressure wave travels into the outer envelope, the remaining disk mass is able to level off in density after 2000 yr. Meanwhile, as lower density parts of the disk are lost to ionization, the disk structure becomes highly irregular while rotational support is lost (panel *b* of Fig. 3.2).

3.3.2 Fragmentation

Consistent with Smith et al. (2011), the accretion luminosity does not heat the disk sufficiently to prevent fragmentation. Radiative feedback does slightly lower the overall fragmentation rate, however, as a total of eight sinks are formed in the 'no-feedback' case versus five sinks in the 'with-feedback' case. In both cases the second sink forms only ~ 100 yr after the initial sink, but, similar to most of the sinks formed, it is quickly lost to a merger. The next sinks to form and survive to the end of the simulation are created at 300 and 200 yr in the 'no-feedback' and 'with-feedback' cases, respectively. This very quick fragmentation is similar to what was described in Clark et al (2011b), Greif et al. (2011), and Smith et al. (2011). The last sink forms as late as 2000 yr in the 'no-feedback' simulation (see Table 4.1).

To understand the formation of the initial disk gravitatonal instability, we first check to see if the disk satisfies the Toomre criterion:

$$Q = \frac{c_{\mathrm{s}}\kappa}{\pi G \Sigma} < 1 \ , \tag{3.14}$$

where c_{s} is the soundspeed, Σ the disk surface density, and κ the epicyclic frequency, which for Keplerian rotation is equal to the disk angular velocity Ω. For the first few 100 yr both disks have average temperatures of around 1000 K, so $c_{\mathrm{s}} \sim 2$ km s^{-1}. $M_{\mathrm{disk}} \simeq 50$ M$_{\odot}$, and the disk radius is nearly 1000 AU, yielding a disk surface density of $\Sigma \simeq M_{\mathrm{disk}}/\pi R^2_{\mathrm{disk}} \sim 140$ g cm^{-2}. We also

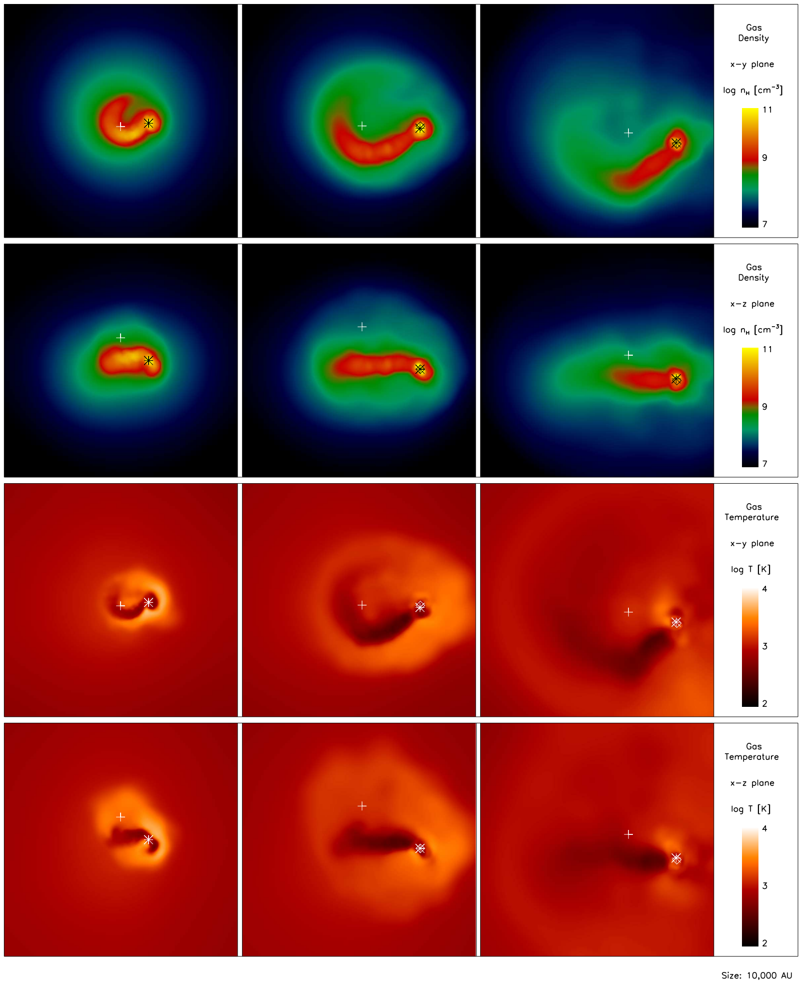

Figure 3.5: Projected density and temperature structure of central 10,000 AU without protostellar feedback at 1000 yr (*left column*), 2000 yr (*middle column*), and 5000 yr (*right column*) after initial sink formation. Asterisks denote the location of the most massive sink. Crosses show the location of the ejected sink. Diamonds mark the locations of the other sinks. *Top row* : Density structure of the central region in the x-y plane. *Second row* : Density structure of the central region in the x-z plane. *Third row* : Temperature structure of the central region in the x-y plane. *Bottom row* : Temperature structure of the central region in the x-z plane. Note the formation of a cool disk and tidal tail structure along with the growth of a surrounding bubble of warm gas. The ejected sink (cross) has a mass of 1 $M_\odot$.

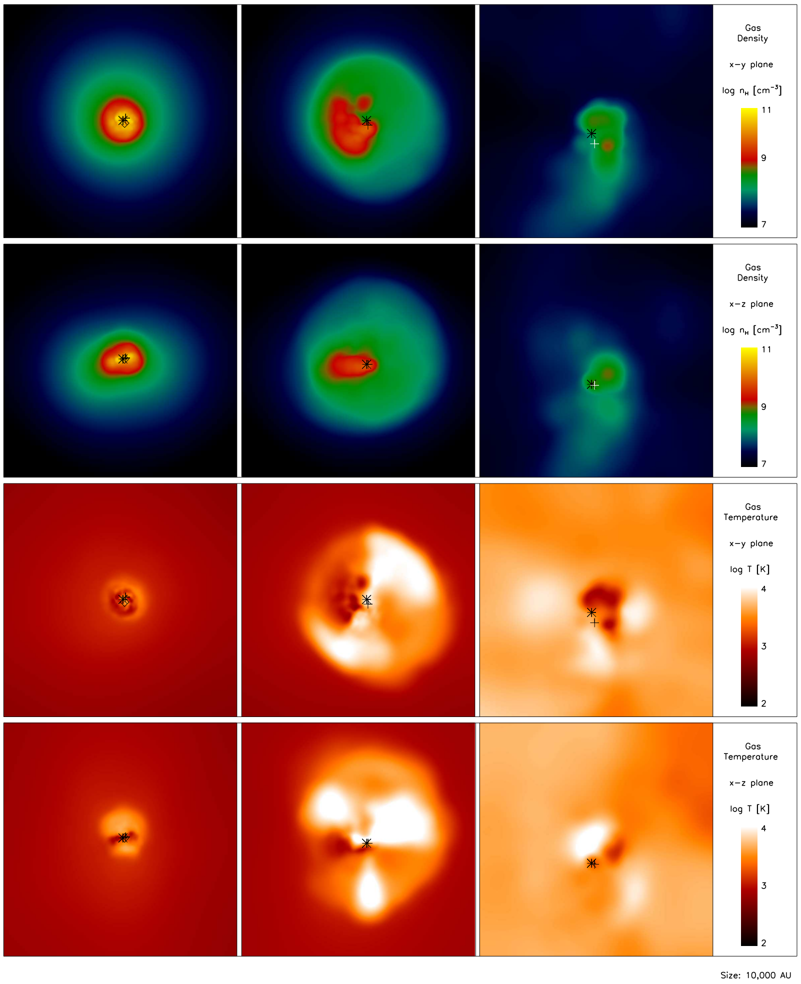

Figure 3.6: Projected density and temperature structure of gas under LW and ionization feedback at 1000, 2000, and 4000 yr after initial sink formation. Asterisks denote the location of the most massive sink. Crosses show the location of the second-most massive sink. Diamonds are the locations of the other sinks. For the rows and columns, we adopt the same convention as employed in Fig. 3.5. Note the growth of a roughly hour-glass shaped structure of hot gas surrounding the disk as the I-front expands into the low-density regions. The hot region expands well beyond the disk by 3000 yr.

sink	$t_{\rm form}$ [yr]	$M_{\rm final}$ [$M_\odot$]	$r_{\rm init}$ [AU]	$r_{\rm final}$ [AU]
1	0	27	0	0
2	300	0.9	100	2330
3	2000	2.75	70	83

Table 3.1: Formation times, final masses, distances from the main sink upon initial formation, and distances from the main sink at the final simulation output in the 'no-feedback' case. We include the sinks still present at the end of the simulation (5000 yr).

sink	$t_{\rm form}$ [yr]	$M_{\rm final}$ [$M_\odot$]	$r_{\rm init}$ [AU]	$r_{\rm final}$ [AU]
1	0	15.9	0	0
2	200	5.6	110	470

Table 3.2: Same as Table 3.1, but for sinks remaining at the end of the 'with-feedback' case at 4200 yr..

approximate κ to be 3×10^{-11} s^{-1}, so $Q \sim 0.2$, easily satisfying the Toomre criterion.

Figures 3.5 and 3.6 show the density and temperature morphology within the central 10,000 AU. The multiple sinks and clumpy disk structure are easily visible here, as expected from the low Toomre parameter, though the particular shape of the disk in each case is very different. The 'no-feedback' case has a clearly visible bifurcated temperature structure, with a cool disk and surrounded by warm gas. The 'with-feedback' also has cool disk gas, but the central region is much more dominated by an hour-glass shaped bubble of hot gas.

As discussed in Kratter et al. (2010), the actual minimum value of Q can vary with disk properties such as scale height, and from Figures 3.5 and 3.6 we see this varies throughout the disk evolution for both cases. Thus, it is also necessary to consider other disk properties, particularly the infall rate of mass onto the disk. The numerical experiments of Kratter et al. (2010) determined that further fragmentation will occur if the mass infall rate onto the disk is sufficiently high, $\dot{M}_{\rm in} \gtrsim c_{\rm s}^3/G$, such that the disk can no longer process the new material quickly enough. The star-disk system in the 'no-feedback' case grows at approximately $5 \times 10^{-3} {\rm M}_{\odot} {\rm yr}^{-1}$ over the first 2000 yr of infall (Fig. 3.3). For the 'with-feedback' case the star-disk system grows at approximately this same rate, but only for the first $\lesssim 1000$ yr. Comparing this to the average gas soundspeed in the disks, ~ 2 km s^{-1} in both cases, we find that $\dot{M}_{\rm in}$ is almost three times greater than $c_{\rm s}^3/G$. Thus, as expected, the disks in both cases fragment during their initial growth phases, though this phase lasts longer for the 'no-feedback' case, for which the formation of the last sink also coincides with a final 'bump' in the disk mass at 2000 yr. No new sinks form once the growth of the disks is halted.

As described in the recent work of Kratter and Murray-Clay (2011), the continued survival of the fragments also requires that a disk must cool quickly enough to overcome opposing effects such as pressure and tidal forces (the 'Stalling Criterion'). They find that this criterion should be easily met for molecular gas ($\gamma = 7/5$), which applies to the densest regions of the disks in our simulations. In particular, we find that for the first few hundred yr after sink formation, the average cooling time of the disk is $t_{\rm cool} \sim 50$ yr. We compare this to the β factor described in Kratter and Murray-Clay (2011) to find $\beta = t_{\rm cool}\Omega < 0.1$. The critical value of β necessary for free-fall collapse of the fragment ranges from 2.5 to 13 depending on γ, and the disks easily satisfy this criterion, thus leading to the early formation of sinks within the disks.

However, in the densest regions of the disk, the 'Collisional Criterion' described in Kratter and Murray-Clay (2011), which requires that the sinks

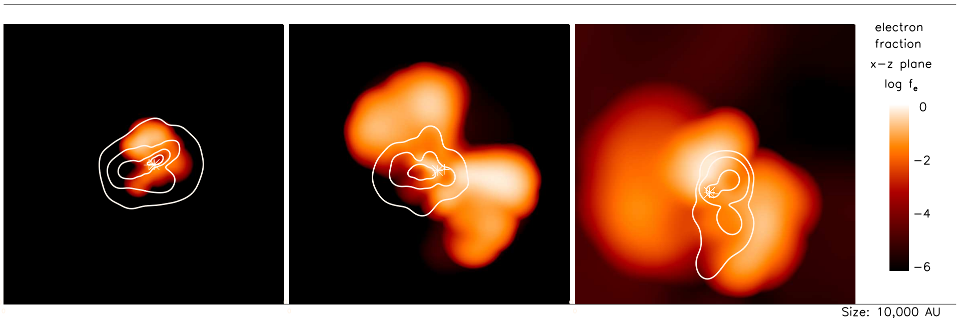

Figure 3.7: Projected ionization structure of gas at 1700, 2300, and 4200 yr after initial sink formation. White lines in left two panels depict the density contours of the disk at densities of $10^{8.5}$, 10^9, $10^{9.5}$, and 10^{10} cm^{-3}. White lines in the right panel depict contours at densities of 10^8, $10^{8.25}$, and $10^{8.75}$ cm^{-3}. Box length is 10,000 AU. Note the pronounced hour-glass morphology of the developing ultra-compact H II region, roughly perpendicular to the disk. This morphology becomes more spherical as the I-front expands.

collapse on roughly the orbital timescale, is harder for these sinks to satisfy. When the disks are undergoing fragmentation during the first few hundred yr, the sinks form within $\sim$ 100 AU of each other and orbit at approximately 5-10 km s^{-1}, yielding an orbital timescale on the order of 100 yr. This is not significantly longer than the free-fall timescale of the sinks, which is $\lesssim$ 100 yr. This leads to sink merging before an entire orbit is complete, particularly during early times in the 'no-feedback' case. The one merger that occurs for the main sink in the 'with-feedback' case occurs after multiple orbits, however, and is a result of migration.

3.3.3 Ionization Front Evolution

The I-front initially appears around the main sink $\sim$ 500 yr after the sink first forms, once it has grown to $\simeq$ 15 $M_\odot$ (see panel *d* of Fig. 3.1). The morphology of the growing I-front is shown in Figure 3.7, where we can see that the I-front expands as an hour-glass shape above and below the disk, and becomes more spherical at later times. Figure 3.8 compares the I-front evolution with that predicted by the analytical Shu champagne flow solution (Shu et al. 2002, see also Alvarez et al. 2006). Different analytical solutions can be found for the evolution of gas under the propagation of an I-front into a powerlaw density profile, which in our case is approximately $\rho \propto r^{-2}$. The ratio of the un-ionized gas temperature to that of the H II region must also be specified for the analytical solution, and in our case we choose a ratio of 20,000 K to 1000 K, or 0.05. The propagation of the I-front can then be described, assuming D-type conditions and that the I-front closely follows the preceeding shock, by a velocity of

$$v_s = x_s c_{\mathrm{s}}, \tag{3.15}$$

while the size of the I-front is

$$r_s = x_s c_{\mathrm{s}} t, \tag{3.16}$$

where c_{s} is the ionized gas soundspeed and x_s is the position of the shock in similarity coordinates, which for our case is $x_s = 2.54$ (see panel *b* of Figure 3.8).

Multiple factors cause deviations from the analytical solution. For instance, the density structure of the gas is not spherically symmetric. Furthermore, the initially close proximity of the ionization front to the sink causes the gravity of the sink to have a non-negligible effect on the early H II region dynamics, a factor that is neglected in the analytical solution. However, this effect loses importance as the H II region grows well beyond the gravitational radius, $r_{\rm g} \simeq GM_*/c_{\rm s} \simeq 50$ AU for a $15M_\odot$ star and 20,000K H II region. The analytical solution also does not take into account the continued infall of gas onto the central region. The outer envelope beyond the disk, which we take as the gas with density greater than 10^8 cm^{-3}, grows for the first 2000 yr at a rate of $\simeq 10^{-2}$ M$_\odot$ yr^{-1}, or 5×10^{47} neutral particles per second. In comparison, the sink emits at 1.5 $\times 10^{48}$ photons per second. Though the infall is not large enough to quench the H II region entirely, it is a large enough fraction of the ionization rate to cause the total mass of the H II region to fluctuate. The motion of the sink through the disk causes the immediately surrounding density structure to vary as well, also contributing to the H II region's unsteady growth. The drop in H II mass at 3500 years occurs after the I-front reaches beyond the envelope into the lower-density ($n > 10^6$ cm^{-3}) core, where the preceeding pressure wave of warm neutral gas has caused a pile-up of gas betweeen 10^6 and 10^8 cm^{-3} (see Fig. 3.4).

This fluctuation is similar to what Galván-Madrid et al. (2011) described in their numerical study of hypercompact H II regions. However, our I-front evolution differs significantly from the analytical study by Omukai and Inutsuka (2002), where they found that a spherical free-falling envelope would not be unbound by an I-front typically until the Pop III star reaches well over 100 M$_\odot$. In our study the gas does become unbound in the regions polar to the disk, thus indicating how variations in three-dimensional structure and accretion flow play a crucial role in a Pop III star's accretion history.

Along with the H II region, suppression of H$_2$ cooling by LW radiation leads to the development of a growing region of hot neutral gas that expands in a bubble around the disk at the soundspeed, which is approximately 7 km s^{-1} (see also Chapter 3.3.1). After 3000 yr this pressure wave has expanded

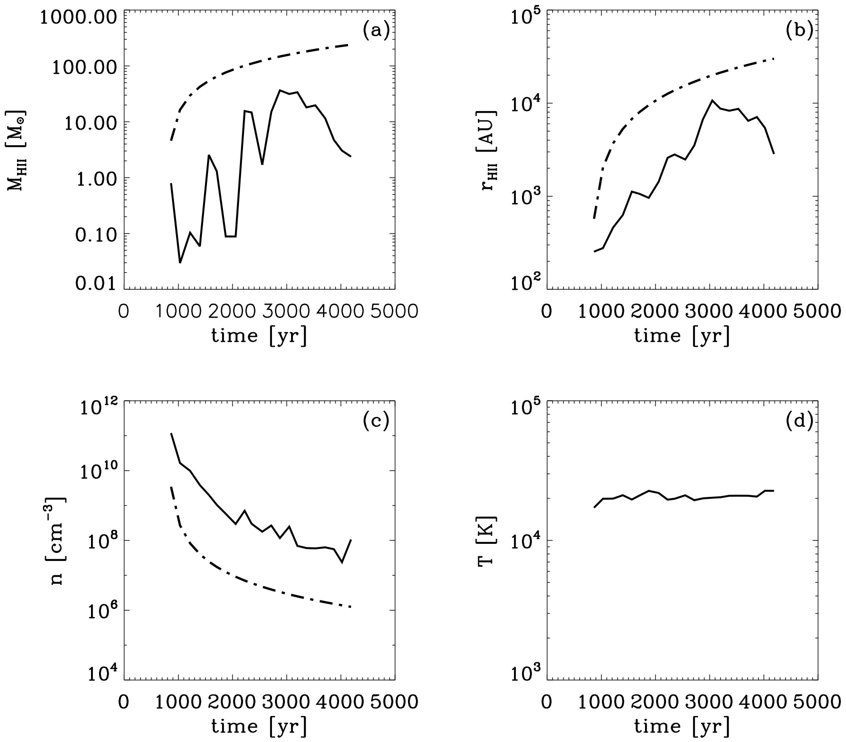

Figure 3.8: Evolution of various H II region properties over time. Solid line is taken from the simulation, while the dashed line is the prediction of the self-similar Shu champagne flow solution. *(a):* Total mass of the H II region. *(b):* Radial extent of the H II region, taken as the distance between the sink and the most distant ionized particle. *(c):* Average density of the ionized particles. *(d):* Average temperature of the ionized particles. Note how the H II region fluctuates on small timescales while the long-term evolution generally follows the predicted analytical solution.

to a radial extent of $r_{\rm pres} \sim 5000$ AU, matching well the predicted size of $r_{\rm pres} = c_{\rm s}\, t = 4400$ AU.

3.3.4 Protostellar Mass Growth

The sink growth in both cases is very similar for the first ~ 200 yr, up to the point the main sinks reach 12 $\mathrm{M}_{\odot}$. This is similar to some of the simulations presented in Smith et al. (2011) in which feedback did not cause a significant decline in sink growth until it grew to > 10 $\mathrm{M}_{\odot}$. Afterwards, we find the deviation in sink accretion history to be significant, leading to a final mass of 27 $\mathrm{M}_{\odot}$ in the 'no-feedback' case and 15 $\mathrm{M}_{\odot}$ in the 'with-feedback' case.

In our 'no-feedback' case, the average accretion rate is 5.4×10^{-3} $\mathrm{M}_{\odot}\,\mathrm{yr}^{-1}$. For the first 600 yr, M_* evolves with time as $t_{\rm acc}^{0.64}$. After the ejection of the secondary sink, the growth rate declines significantly to $M_* \propto t_{\rm acc}^{0.13}$ (see Figure 3.9). Even after the growth of the disk and envelope is halted, tidal torques are able to continuously funnel additional mass onto the sink.

With feedback, the average accretion rate drops to $3\times10^{-3}\mathrm{M}_{\odot}\,\mathrm{yr}^{-1}$. M_* evolves more slowly as $t_{\rm acc}^{0.56}$ for the first 500 yr, and afterwards the accretion rate drops to nearly zero. Given this strong protostellar feedback onto the disk, we can devise a simple analytical estimate for the final mass attainable by Pop III stars as follows:

$$M_* = \dot{M}_* t_{\rm feed}, \qquad (3.17)$$

where, $t_{\rm feed}$ is the timescale over which Pop III accretion will be essentially shut off. Given that Pop III stars must accrete through a disk, and assuming for simplicity the thin-disk approximation,

$$\dot{M}_* = 3\pi\Sigma\nu, \tag{3.18}$$

where ν is the effective viscosity within the disk. We can approximate this using

$$\nu = \alpha c_{\rm s}^2/\Omega, \tag{3.19}$$

where α is the disk viscosity parameter (Shakura and Sunyaev 1973). For gravitational torques within strongly self-gravitating disks, $\alpha \propto (t_{\rm cool}\Omega)^{-1}$ and typically ranges from 0.1-1 (e.g. Lodato and Rice 2005). In cases like the central regions of our disk closest to the main sink, where $t_{\rm cool} \sim \Omega^{-1}$ (see Chapter 3.3.2), the value for α should be closer to 1.

We now have the expression

$$M_* = 3\pi\Sigma c_{\rm s}^2 \frac{\alpha}{\Omega} t_{\rm feed}. \tag{3.20}$$

If we estimate that the feedback begins once the photodissociation front reaches the scale of the disk radius, which will occur over the sound-crossing time $t_{\rm sound}$, we then have $t_{\rm feed} \sim t_{\rm sound} \simeq 1000$ AU / 7 km s^{-1} $\simeq 700$ yr. Using $\Sigma = 140$ g cm^{-2}, $\alpha = 1$, $\Omega = 3 \times 10^{-11}$ s^{-1}, and $c_{\rm s} = 2$ km s^{-1}, we have a final mass of $M_* = 20$ M$_\odot$, well approximating the final protostellar mass reached in our 'with-feedback' case.

We note that the lack of accretion in the 'with-feedback' case after the sink reaches 15 M$_\odot$ is to some extent a numerical artifact. This is most likely due to a lack of shielding from radiation on sub-sink scales, leading to an overestimation of the radiation that will reach into the inner disk. Furthermore,

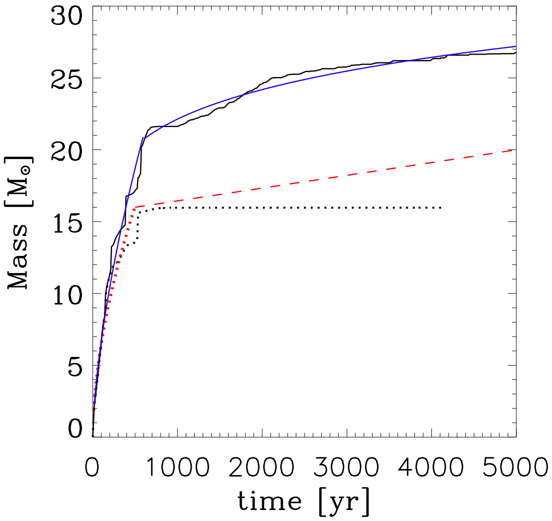

Figure 3.9: Effect of radiative feedback on protostellar accretion. Black solid line shows mass growth with no radiative feedback, while black dotted line shows the ‘with-feedback’ case. The blue solid line is a double powerlaw fit to the sink growth rate for the ‘no-feedback’ case, and the red dotted line is a fit to the first 500 yr of the ‘with-feedback’ case. The red dashed line shows a conservative upper limit for continued sink growth in the ‘with-feedback’ case not seen in the simulation. Radiative feedback leads to a divergence in the accretion histories in less than 1000 yr, and in the ‘with-feedback’ case the sink does not grow beyond ~ 20 M$_\odot$ in the time of the simulation.

the discrete nature of the gas particles means that the average accretion rate after this point could be below $\sim 10^{-5}$ $\mathrm{M}_{\odot}$ yr^{-1} over timescales on the order of 1000 yr without being resolved. Given the disruption of the disk in both cases at later times, let us estimate by how much the sink accretion rate should truly decline. In the 'with-feedback' case, by 3000 years of sink accretion the mass of gas in the disk has declined from 40 $\mathrm{M}_{\odot}$ to $\lesssim 10$ $\mathrm{M}_{\odot}$, over a factor of four. Σ thus decreases by the same amount. The disk temperature also decreases from 1000 to 600 K. Considering equations (18) and (19), this implies that the accretion rate should decrease by an order of magnitude, from 2×10^{-2} $\mathrm{M}_{\odot}$ yr^{-1} over the first 1000 years to $\sim 10^{-3}$ $\mathrm{M}_{\odot}$ yr^{-1} afterwards. A future simulation with improved resolution might thus show further sink growth, in this case to roughly 20 $\mathrm{M}_{\odot}$ after 5000 yr (see Fig. 3.9).

In the 'no-feedback' case, at 1000 yr the disk mass has dropped to slightly more than half of its value at the time of initial sink formation, and the mass continues to decline further to one-fourth the intial value. If we also account for an increase in disk size due to angular momentum conservation, then Σ decreases by nearly an order of magnitude. The disk temperature has also dropped from 1000 to 500 K by the end of the simulation (see Figure 3.2), leading to a decrease in c_{s}. From this we approximate that the sink accretion rate should again drop by over an order of magnitude after 1000 years, which indeed occurs for the 'no-feedback' case.

3.4 Summary and Discussion

We have performed cosmological simulations of the build-up of a Pop III star to determine how LW and ionizing radiative feedback influences the mass growth of the star and the fragmentation of primordial gas. We find that radiative feedback will not prevent fragmentation, but will lower the final mass attainable by a Pop III star. Inclusion of feedback also led to a massive binary system instead of a higher-order multiple like that seen in, e.g., Stacy et al. (2010) and our 'no-feedback' case, since the feedback quenched disk growth and fragmentation early on. In agreement with Smith et al. (2011), we furthermore find that stellar N-body dynamics can also play a significant role in the growth of a Pop III star through stellar ejections and disk scattering.

It is interesting to compare our results to that of recent work by Peters et al. (2010). They similarly examine ionizing and non-ionizing radiative feedback on massive star formation, though they study the case of present-day star formation, and their initial configuration was different from ours in that they began with a 1000 $M_{\odot}$ rotating molecular cloud core. They find H II regions which fluctuate in size and shape as gas flows onto the stars, and that the final mass of the largest stars is set by 'fragmentation-induced starvation,' a process in which the smaller stars accrete mass flowing through the disk before it is able to reach the most massive star. This is in contrast to models in which the final stellar mass is set once ionizing radiation shuts off the disk accretion (e.g. McKee and Tan 2008). In our 'with-feedback' case we find that it is radiative feedback that shuts off accretion to both sinks, and that the smaller sink does not intercept any gas flow onto the main sink, simply because the infall rate is so low. A similar study of current-day star formation by Krumholz et al. (2009) found that a prestellar core would similarly collapse into a disk that would host a multiple system of massive stars, even under the effects of radiation pressure. However, they followed smaller average accretion rates over a longer period of time (50,000 yr) and found that gravitational and Rayleigh-Taylor instabilities would continue to feed mass onto the disk and stars.

We also note that, despite their very similar numerical setups, the disk evolution and accretion rate of our 'no-feedback' case differs somewhat from that described in Stacy et al. (2010). Several distinctions between the simulations, however, explain this. The high-density cooling and chemistry is updated from that used in Stacy et al. 2010 (see Chapter 3.2.2). We also use an adaptive softening length instead of a single softening length for all gas particles as in Stacy et al. (2010), and our criteria for sink accretion are slightly more stringent. The main contribution to the difference, however, is likely the stochastic nature of the sink particle dynamics. While no sink was ejected in Stacy et al. (2010), the sink ejection and subsequent rapid velocity of the main sink in our 'no-feedback' case altered the disk structure, and the main sink would likely have grown to a higher mass otherwise. Nevertheless, the final sink masses in both simulations were still the same to within a factor of two.

The radiative feedback seen here is much stronger than the analytical prediction of McKee and Tan (2008). They found that a Pop III star could grow to over 100 $M_{\odot}$ through disk accretion, as disk shadowing allowed mass to flow onto the star even while the polar regions became ionized. Our lack of resolution prevents this disk shadowing to be modeled properly on sub-sink scales, and the ionizing photon emission emanating from the sink edge is likely overestimated. McKee and Tan (2008) furthermore assumed disk axisymmetry, which does not describe the disk in either of our test cases. At various points in the 'with-feedback' simulation, the lack of axisymmetry allowed the sink to ionize the more diffuse parts of the disk, which would not have occured in the McKee and Tan (2008) model. Nevertheless, shielding does indeed keep some high density particles from becoming ionized in our 'with-feedback' case. However, the I-front does not expand in a uniform fashion along the polar directions, as the disk rotates, and the position of the main sink within the disk varies as it orbits its companion sink. Thus, different angles will be shielded at different times. Once gas along a certain direction has been ionized, it may recombine at later times, but LW radiation prevents most of this gas from cooling back down to below a few thousand Kelvin. The resulting pressure wave of warm neutral gas continues to expand in all directions, and mass flow onto the disk and sinks is greatly reduced. Thus, while our results underestimate the effect of shielding, it still highlights how non-axisymmetry will enhance the effects of radiative feedback, and the true physical case likely lies somewhere in between our 'with-feedback' case and the prediction of McKee and Tan (2008). In a similar vein, non-axisymmetry can also promote further disk fragmentation, and this in turn can result in N-body dynamics that may provide another means of reducing Pop III accretion rates.

The fragmentation of primordial gas and growth of Pop III stars has recently been modeled from cosmological initial conditions with resolution reaching nearly protostellar scales (Clark et al. 2011b, Greif et al. 2011). However, though our simulation is less highly resolved, it explores a different regime of Pop III growth. The aforementioned studies could not follow the mass accretion for more than 100-1000 yr, before the protostars had grown beyond 10 $M_{\odot}$, and they did not follow the growth of the I-front. Our work thus affords a first look, starting from cosmological initial conditions, at how Pop III growth will continue beyond 1000 yr, after the formation of the I-front. Future cosmological simulations will eventually bridge this gap by both resolving protostellar scales and modeling ionizing radiation, but such a calculation pushes current computational limits.

If radiative feedback were typically able to prevent Pop III stars from growing to more than a few tens of solar masses, this would have several effects on their observational signatures. PISNe would be less frequent, as this requires a star to grow to greater than 140 $M_{\odot}$. Old, metal-poor stars within the Milky Way halo and nearby dwarf galaxies may preserve the nucleosynthetic pattern of the first SNe, so this may help to explain the lack of PISNe chemical signatures found in these nearby stars (e.g. Christlieb et al. 2002; Beers and Christlieb 2005; Frebel et al. 2005; Tumlinson 2006; but see Karlsson et al. 2008). Instead, Pop III stars may end their lives through core-collapse SNe or direct collapse to BHs. For sufficient stellar rotation rates, the possibility of Pop III collapsar GRBs also remains (e.g. Stacy et al. 2011). The feedback of Pop III stars on their neighboring metal-free minihalos would also be altered, though the details of how the mass and formation rate of such ‘Pop III.2’ stars would be affected remains to be determined by future simulations.

Chapter 4

Rotation speed of the first stars[1]

4.1 Overview

The mass of the first stars is the main factor in determining their cosmological impact. Pop III stars are generally believed to be very massive ($\sim$ 100 $M_\odot$; e.g. Abel et al. 2002; Bromm et al. 2002), though recent evidence for fragmentation in primordial gas may imply that the typical Pop III mass was somewhat lower (Clark et al. 2008, Clark et al. 2011a, Turk et al. 2009; Stacy et al. 2010). Mass determines both the ionizing photon production as well as the end state of the star. For instance, stars in the mass range of $140\ M_\odot < M_* < 260\ M_\odot$ will die as pair-instability supernovae (PISNe; Heger and Woosley 2002), while below 40 $M_\odot$, stars are expected to explode as core-collapse SNe, leaving behind a neutron star or black hole. Nomoto et al. (2003), however, find that the nature of the explosions from this mass range may vary depending on the angular momentum of the collapsing core. Stars with little angular momentum will explode as faint SNe, while stars of the same mass but higher angular momentum will become extremely energetic hypernovae.

Pop III stars also have the potential to produce gamma-ray bursts (GRBs), particularly given the connection between long-duration GRBs and the deaths of massive stars (see Woosley and Bloom 2006). GRBs may provide one of the most promising methods of directly probing the final stages of Pop III stars, provided they occurred with a high enough frequency (e.g. Bromm and Loeb 2002, 2006; Gou et al. 2004; Belczynski et al. 2007). Naoz and Bromberg (2007) used early *Swift* data and an idealized star formation rate model to estimate that Pop III stars may indeed produce GRBs at an efficiency of $\sim 10^{-4}$ GRBs per solar mass incorporated in primordial stars. For the collapsar model of GRB generation to operate, this will require sufficient angular momentum in the Pop III progenitor for an accretion torus to form around the remnant black hole (e.g. Woosley 1993; Lee and Ramirez-Ruiz 2006). The progenitor star must also lose its hydrogen envelope to enable the relativistic jet to penetrate through and exit the star (e.g. Zhang et al. 2004). Fulfilling both of these conditions can be difficult for a single-star progenitor, however, because removing the extended hydrogen envelope will also lead to removal of angular momentum in the core (e.g. Spruit 2002; Heger et al. 2005; Petrovic et al. 2005). These conditions for a GRB may be more easily met, however, in a close binary system that experiences Roche lobe overflow (e.g. Lee et al. 2002; Izzard et al. 2004). Let us also note an alternate scenario recently explored by Suwa and Ioka (2010). They analytically find that the jet can break out even from an extended hydrogen envelope of a Pop III star if the jet is powered by magnetic fields. This interesting result warrants further numerical study.

---

[1] This chapter has been published as Stacy A., Bromm V., Loeb A., 2011, MNRAS, 413, 543

Another possibility arises if a Pop III star has a large enough spin. This can affect its nucleosynthesis and change the evolution off the main sequence (MS), opening a new pathway for the formation of single-star progenitor GRBs (e.g. Yoon and Langer 2005; Woosley and Heger 2006; Ekström et al. 2008a).

Woosley and Heger (2006) find through their stellar evolution models that very massive ~ 20 $M_\odot$ stars rapidly rotating at $\simeq 400$ km s^{-1} ($\simeq 40\%$ of the break-up speed) can completely mix while on the MS, bypassing the red giant phase and becoming a Wolf-Rayet (WR) star. This evolutionary path may furthermore allow the star to retain enough angular momentum to become a GRB, particularly if the star has low-metallicity and thus experiences significantly reduced mass loss compared to solar-metallicity WR stars. Yoon and Langer (2005) agree, using a different numerical methodology, that rotationally induced mixing will allow a low-metallicity massive star to evolve into a rapidly rotating WR star and potentially a GRB. Finally, Ekström et al. (2008a) studied the evolution of metal-free stars with a range of masses (15-200 $M_\odot$) and a high rotation rate of 800 km s^{-1}, corresponding to a fraction of 40-70% of their break-up speed. In contrast to the previous studies, in their models chemical mixing was usually not sufficient for the red giant phase to be avoided. In fact, they found that the rotating stars generally end their lives at a cooler location of the Hertzsprung-Russel diagram (HRD). In addition, rotating stars produced a higher amount of metals, compared to their non-rotating counterparts. Ekström et al. (2008a) attribute this difference to the fact that, unlike the earlier studies, they did not include the magnetic dynamo mechanism of Spruit (2002). With or without this mechanism, however, all studies conclude that stellar rotation altered the evolution and fate of low-metallicity and Pop III stars. We also point out that, though we sometimes refer to low-metallicity studies, Pop III evolution is distinct from that of low-metallicity, and results for one do not simply extrapolate to the other (e.g. Ekström et al. 2008b). This highlights the need for continued investigation of rotating metal-free stars.

It is apparent that the angular momentum of Pop III stars plays a key role in their evolution and death, as well as their subsequent impact on the IGM. Whereas the mass scale of the first stars has been investigated in numerous studies, their spin remains poorly understood. It is an open question whether Pop III stars can realistically attain the high spin needed for the above-mentioned processes to occur. Current observations of massive O and B-type stars in our Galaxy and the Large Magellanic Cloud show that they can indeed be rapid rotators, spinning at a significant percentage of break-up speed (a few tens of percent). They have a large range of spin, from several tens of km s^{-1} to well over 300 km s^{-1}, with an average of about 100–200 km s^{-1} (e.g. Huang and Gies 2008; Wolff et al. 2008). This does not necessarily apply to Pop III stars, however, which formed in a different environment. While Pop III stars formed in minihalos whose gravitational potential wells were dominated by dark matter (DM), massive stars today form within molecular clouds that are not DM dominated, and are embedded in much larger galaxies. The angular momentum in the latter case ultimately derives from galactic differential rotation on the largest scales, and turbulence in the interstellar medium (ISM) on smaller scales (see, e.g. Bodenheimer 1995). Wolff et al. (2008) argue that their measured stellar rotation rates reflect the initial conditions of the cores in which the stars formed, particularly the core turbulent speeds and resulting infall rates. To better determine the possible rotation rates of Pop III stars, it is thus necessary to study the environment specific to where they formed.

To better understand the potential for the various spin-dependent evolutionary pathways of Pop III stars, we perform a three-dimensional cosmological simulation that follows the evolution of primordial gas in a minihalo to densities of $n > 10^{12}$ cm^{-3}. Similar to Bromm and Loeb (2004) and Stacy et al. (2010), we represent gravitationally collapsing high-density peaks using the sink particle method first introduced by Bate et al. (1995). This allows us to follow the mass flow onto the sinks for many (~ 100) dynamical times. As a sink particle grows in mass, the angular momentum of the accreted mass is recorded, allowing us to measure the total angular momentum of the sink and estimate the spin of the Pop III star represented by the sink. This is very similar to the method used in Jappsen and Klessen (2004) when they studied the angular momentum evolution of protostellar cores, though their calculation had lower resolution and was designed to study modern-day star formation as seen in the ISM. We give further details concerning our numerical methodology in Chapter 4.2, while in Chapter 4.3 we present our results, including estimates of the stellar rotation rate. In Chapter 4.4 we discuss the implications for the evolution and death of Pop III stars, and in Chapter 4.5 we address the possibility of sub-sink fragmentation. We summarize our main conclusions in Chapter 4.6.

4.2 Numerical Methodology

4.2.1 Initial Setup

Similar to the method used in Stacy et al. (2010), we carry out our study using GADGET, a three-dimensional smoothed particle hydrodynamics (SPH) code (Springel et al. 2001; Springel and Hernquist 2002). We perform the final part of the simulation described in Stacy et al. (2010) again, starting from approximately 4000 years (~ 100 free-fall times) before the first sink particle forms. This simulation was originally initialized at $z = 99$ in a periodic box of length 100 h^{-1} kpc using both SPH and DM particles. This was done in accordance with a ΛCDM cosmology with $\Omega_{\Lambda} = 0.7$, $\Omega_{\rm M} = 0.3$, $\Omega_{\rm B} = 0.04$, and

$h = 0.7$. To accelerate structure formation, we chose an artificially enhanced normalization of the power spectrum of $\sigma_8 = 1.4$. We have verified that the density and velocity fields in the center of the minihalo are very similar to previoussimulations. Even though we used an artificially high value ofσ_8, the angular momentum profile of our minihalo just beforesink formation was still very similar to that of other cosmologicalsimulations which used lower σ_8 values. In particular, the cosmological simulation of Yoshida et al. (2006), which used$\sigma_8 = 0.9$, and that of Abel et al. (2002), which used$\sigma_8 = 0.7$, resulted in minihalo profiles which were especiallysimilar to ours on the smaller scales from which the mass of the sinksis accreted. This demonstrates that our realization leads toconditions that are typical for primordial star formation (see the discussion in Stacy et al. 2010).

To achieve high resolution we employed a standard hierarchical zoom-in procedure (see Stacy et al. 2010 for further details). This involved adding three additional nested refinement levels of length 40, 30, and 20 kpc (comoving) centered on the site where the first minihalo will form. Each level of higher refinement replaces particles from the lower level with eight child particles such that in the final simulation a parent particle is replaced by up to 512 child particles. The highest-resolution gas particles have a mass of $m_{\rm SPH} = 0.015\ {\rm M}_{\odot}$. Therefore, the mass resolution of the refined simulation is: $M_{\rm res} \simeq 1.5 N_{\rm neigh} m_{\rm SPH} \lesssim 1\ {\rm M}_{\odot}$, where $N_{\rm neigh} \simeq 32$ is the typical number of particles in the SPH smoothing kernel (e.g. Bate and Burkert 1997). The main difference between the current simulation and that described in Stacy et al. (2010) is that we now record the angular momenta and velocities of the sink-accreted particles before they become incorporated into the sinks. This allows us to track the total spin of the sink particles as they grow in mass.

4.2.2 Chemistry, heating, and cooling

The chemistry, heating, and cooling of the primordial gas is treated similarly to that in earlier studies such as Bromm and Loeb (2004), Yoshida et al. (2006), and Stacy et al. (2010). We track the abundance evolution of the following species: H, H^+, H^-, H_2, H_2^+, He, He^+, He^{++}, e^-, and the deuterium species D, D^+, D^-, HD, and HD^+. In the high-density disk that forms within the minihalo, H_2 is the dominant cooling agent, and although deuterium is unimportant for the thermal and chemical evolution of the gas at the late stages of collapse and accretion studied here, we include it for completeness. We use the same chemical network and the same cooling and heating terms as used in Stacy et al. (2010). This included accounting for modified physics at densities greater than $\simeq 10^8$ cm^{-3}: three-body processes which accelerate the formation of H_2 until the gas becomes fully molecular around $\simeq 10^{10}$ cm^{-3}, enhanced cooling due to collisions between H_2 molecules, H_2 formation heating, and modified values for the adiabatic exponent $\gamma_{\rm ad}$ and the mean molecular weight μ. As described in Stacy et al. (2010), the evolution of the primordial gas up to the formation of the first sink particle was consistent with that of previous studies.

4.2.3 Sink Particle Method

We convert an SPH particle into a sink particle if it reaches a number density of $n_{\rm max} = 10^{12}$ cm^{-3}. SPH particles that are within a distance $r_{\rm acc}$ of the sink are removed from the simulation and their mass is also added to that of the sink, provided that they are not rotationally supported against infall towards the sink. We set $r_{\rm acc}$ equal to the resolution length of the simulation,

$r_{\rm acc} = L_{\rm res} \simeq 50\,{\rm AU}$, where:

$$L_{\rm res} \simeq 0.5 \left(\frac{M_{\rm res}}{\rho_{\rm max}} \right)^{1/3} \, ,$$

with $\rho_{\rm max} \simeq n_{\rm max} m_{\rm H}$ and $m_{\rm H}$ being the proton mass. The sink particle's mass, $\rm M_{sink}$, is initially close to the resolution mass of the simulation, $M_{\rm res} \simeq 0.7$ $\rm M_{\odot}$.

We check for rotational support by comparing the specific angular momentum of the SPH particle, $j_{\rm SPH} = v_{\rm rot} d$, with the requirement for centrifugal support, $j_{\rm cent} = \sqrt{G M_{\rm sink} r_{\rm acc}}$, where $v_{\rm rot}$ and d are the rotational velocity and distance of the particle relative to the sink. Once the sink is formed, any SPH particle that satisfies $d < r_{\rm acc}$ and $j_{\rm SPH} < j_{\rm cent}$ is accreted onto the sink. A sink particle can also be merged with another sink particle if these same criteria are met. When the sink is first formed, and after each subsequent accretion event, its position and velocity are set to the mass-weighted average of the particles it has accreted. In this way sink particles can grow and accrete mass over time.

As discussed in Bromm et al. (2002) and Stacy et al. (2010), our criteria for sink formation should be robust. A gas particle must collapse two orders of magnitude above the average density of the surrounding disk, $\simeq 10^{10}$ cm^{-3}, before it is above the density threshold for sink formation. This along with the small value for $r_{\rm acc}$ and the further accretion criterion of non-rotational support ensures that sinks are indeed formed from gravitationally collapsing gas.

Sink particles are held at a constant density of $n_{\rm max} = 10^{12}$ cm^{-3}, a constant temperature of 650 K, and a constant pressure corresponding to its temperature and density. Giving the sink a temperature and pressure prevents the existence of a pressure deficit around the sink that otherwise would yield an artificially high accretion rate (see Bromm et al. 2002; Martel et al. 2006). However, the sink can still evolve in position and velocity due to gravitational and hydrodynamical interactions.

The sink particle method is very useful for various reasons. It eliminates the need to incorporate chemistry, hydrodynamics and radiative transfer at extremely high densities ($n > 10^{12}$ cm^{-3}). More importantly, by stopping the density growth at $n > 10^{12}$ cm^{-3}, the method allows the evolution of the region of interest to be followed for many dynamical times. Without the sink particle method, this would be computationally challenging because the increasing density would lead to prohibitively small numerical timesteps, a problem sometimes called 'Courant myopia'. Finally, the sink particle method allows for a direct measurement of the angular momentum growth and the accretion rate onto the high-density region instead of having to indirectly extrapolate this from the instantaneous density and velocity profiles at the end of the simulation (e.g. Abel et al. 2002; Yoshida et al. 2006).

4.3 Results

4.3.1 Sink Growth and Angular Momentum

4.3.1.1 Accretion Rate

The first minihalo within the cosmological box forms at $z \simeq 20$. The subsequent evolution of the central region of the minihalo to densities of $n = 10^{12}$ cm^{-3} is described in Stacy et al. (2010). The growth of the first sink that forms, which will be referred to as sink A, is similar to that found in Bromm and Loeb (2004) as well as Stacy et al. (2010). The mass growth is especially similar to that in Stacy et al. (2010) for the first few hundred years, up to several dynamical times after the sink initially forms. Though the sink accretion criteria have some small differences in each of these three studies, this similarity in initial sink growth points especially to the robustness of the density threshold criterion for initial sink formation. After 5000 years of accretion, sink A grows to a mass of 34 $\mathrm{M}_{\odot}$, similar to that found in Bromm and Loeb (2004). However, this is largely due to a significant merger event at around 3800 years, and before this the mass of sink A is around 1/3 below that found in Bromm and Loeb (2004). Furthermore, the final sink mass is slightly less ($\sim 20\%$) than the final mass found in Stacy et al. (2010). The reduced accretion rate found in this current calculation likely arises because a sink is not allowed to accrete a particle if that particle is rotationally supported against infall onto the sink, which is an additional condition that was not included by Stacy et al. (2010). This condition seems to slightly decrease the number of sink merger events, though the growth rate between merger events is also somewhat reduced.

Around 300 years after the formation of sink A, a second sink forms. Meanwhile, as sink A grows, a disk with radius of about 1000 AU develops around the sink, and disk fragmentation allows further sinks to form. By the end of the simulation, 5000 years after sink A first forms, there is a total of four sinks. The sink that is second-most massive, which we will label sink B, has grown almost to 9 $\mathrm{M}_{\odot}$ (Fig. 4.1), while the remaining two sinks are $\sim$ 1 and 7 $\mathrm{M}_{\odot}$. The overall accretion rate of sink B, $\simeq 2 \times 10^{-3}$ $\mathrm{M}_{\odot}$ yr^{-1}, is around 30% that of sink A, $\simeq 7 \times 10^{-3}$ $\mathrm{M}_{\odot}$ yr^{-1}. The accretion rate for both sinks does not stay at a steady value, however, and actually declines as the sinks grow. To show this we also provide power-law fits to the sink growth (red lines in Fig. 4.1). For sink A, $M_{\mathrm{sink}} \propto t^{0.48}$, and $\dot{M} \propto t^{-0.52}$. For sink B,

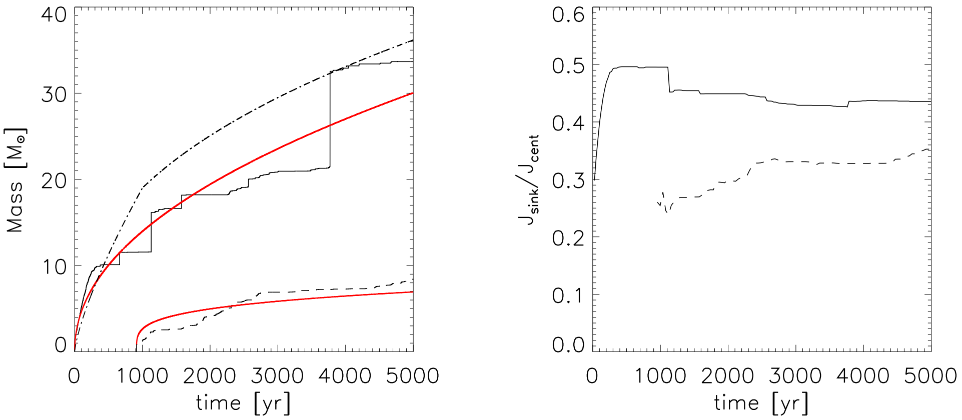

Figure 4.1: *Left*: Growth of sink mass over time. Solid line is the growth of sink A, and dashed line is the growth of sink B. Dash-dot line is the result from Bromm & Loeb (2004). Red lines are power-law fits to the mass curves. Though sink A grows rapidly for the first few hundred years, adding the accretion criterion of non-rotational support later causes its growth rate to be somewhat lower than that found in Bromm & Loeb (2004) until a large merger event at 3800 years. *Right*: Ratio $\epsilon = J_{\rm sink}/J_{\rm cent}$ as sinks grow over time. Representation of different sinks is the same as in the left panel. For sink B's accretion and the first $\sim$ 1000 years of sink A's accretion, note the similarity in how both mass and ϵ increase over time. This is due to the steadily growing rotational support of the mass that flows onto the sinks.

$M_{\rm sink} \propto t^{0.25}$, and $\dot{M} \propto t^{-0.75}$.

4.3.1.2 Angular Momentum

As the sinks grow in mass, the angular momentum of each particle accreted, $J_{\rm SPH} = m_{\rm SPH} v_{\rm rot} d$, is added to the total angular momentum of the sink, $J_{\rm sink}$. Note that the scale of the sink, $\rm r_{acc}$ = 50 AU, is smaller than the radius corresponding to the sonic point:

$$r_{\rm sp} = \frac{GM_*}{c_s^2}, \tag{4.1}$$

where $c_{\rm s}$ is the sound speed. A typical sink mass is 10 $\mathrm{M}_\odot$, and the highest-temperature, high-density ($n > 10^8 \mathrm{cm}^{-3}$) gas is approximately at 7000 K, or $c_{\rm s} \simeq 7$ km s^{-1}. This yields $r_{\rm sp} \simeq 180$ AU. For the cooler disk gas, $T \sim 500$ K and $c_{\rm s} \simeq 2$ km s^{-1}, so that $r_{\rm sp}$ is larger, ~ 2000 AU, and similar to the size of the large-scale disk. The sinks therefore easily resolve the scale of the sonic point. Angular momentum transport from inside $r_{\rm sp}$ to outside $r_{\rm sp}$ will be difficult once the inflow becomes supersonic (Ulrich 1976; Tan and McKee 2004). In Chapter 4.3.2, we will show that the inflow onto the sinks does indeed quickly become supersonic, and in fact the total angular momentum within the sonic point steadily grows as more mass continues to fall in. However, the angular momentum inside $r_{\rm sp}$ can still be redistributed through torques within the large-scale disk.

$J_{\rm sink}$ stays at a fairly steady fraction, $\epsilon = J_{\rm sink}/J_{\rm cent}$, of the angular momentum required for full centrifugal support at the accretion radius, $J_{\rm cent} = M_{\rm sink} j_{\rm cent}$. Figures 4.1 and 4.2 show this fraction to range from $\epsilon \simeq 0.45 - 0.5$ for sink A and $\epsilon \simeq 0.25 - 0.35$ for sink B. Thus, on the scale of the accretion radius the sinks never become fully rotationally supported. Rotational velocities of the accreted particles were also recorded, and the total rotational velocity of each sink, $v_{\rm sink}$, can be determined through a mass-weighted average of each accreted particle's $v_{\rm rot}$ (right panel of Fig. 4.2). Similar to the behavior of $J_{\rm sink}$, $v_{\rm sink}$ stays at the same fairly constant fraction of $v_{\rm cent} = \sqrt{GM_{\rm sink}/r_{\rm acc}}$.

The specific angular momentum of the sinks does not stay perfectly constant, however. Comparing the mild evolution of ϵ with the sinks' mass growth (Fig. 4.1) shows a general correspondence between them, similar to that found in the simulations of Jappsen and Klessen (2004). For sink B in particular, the shape of the mass versus time curve is very similar to that of the ϵ versus time curve, and the same applies for the first ~ 1000 years of sink A's accretion. These are periods when the mass that flows onto the sinks is gradually increasing in rotational support as the large-scale disk spins up. The gas close to sink A is the first to spin up, and so sink A reaches its maximum ϵ earlier on in the simulation.

It is interesting to compare $J_{\rm sink}$ with the minimum angular momentum required for centrifugal support against infall onto a black hole, as this is one of the minimum requirements for a successful collapsar engine to power a GRB. For a non-rotating black hole of mass $M_{\rm BH}$, the innermost stable circular orbit occurs at $r_{\rm ISCO} = 6GM_{\rm BH}/c^2$. This corresponds to a minimum angular momentum of $J_{\rm ISCO} = \sqrt{6}GM_{\rm BH}^2/c$, which would be slightly smaller for rotating black holes. As can be seen in Fig. 4.2, sink A and sink B both gather at least an order of magnitude more angular momentum than necessary for a collapsar engine. Whether this large sink-scale angular momentum continues down to stellar scales is discussed below.

4.3.2 Stellar Rotational Velocity

4.3.2.1 Thin Accretion Disk

We now address how the measured sink spin can be extrapolated to the scale of the final (MS) Pop III star. To this end, let us compare $J_{\rm sink}$ to angular momentum values corresponding to rotational break-up speeds on stellar scales. A representative value for $J_{\rm break-up}$ can be found assuming a mass of 100 $M_{\odot}$ and a radius of 5 $R_{\odot}$, typical for massive Pop III MS stars (e.g. Bromm et al. 2001a), though this value may be somewhat larger for high

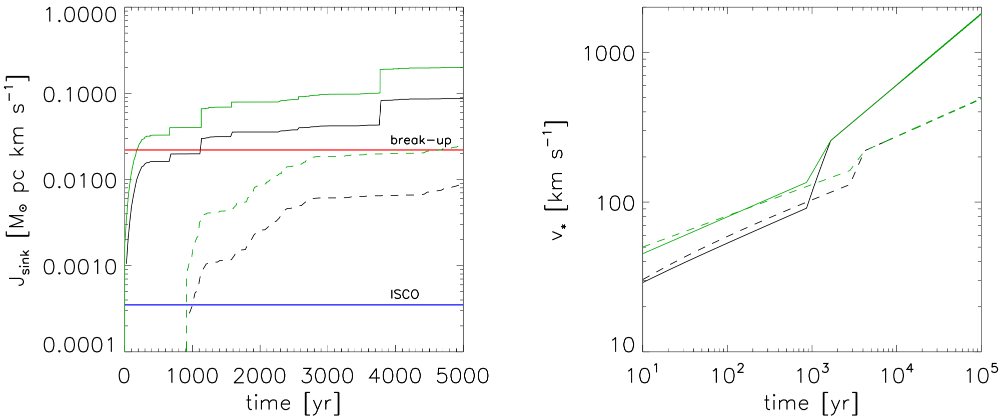

Figure 4.2: *Left*: Angular momentum $J_{\rm sink}$ of the sinks over time, taken by summing the angular momentum $J_{\rm SPH} = m_{\rm SPH} v_{\rm rot} d$ of each accreted particle just before it is added onto the sink. Solid black line represents sink A, dashed black line represents sink B. The angular momentum of each sink grows as it accretes more mass, always staying at a fraction of $J_{\rm cent}$ (solid green line for sink A, dashed green line for sink B). Note that for sink A, $J_{\rm sink}$ exceeds the stellar $J_{\rm break-up}$ (red line) by the end of the simulation. The horizontal blue line shows the orbital angular momentum at the *innermost stable circular orbit (ISCO)*, $J_{\rm ISCO}$, for a 100 $\mathrm{M}_\odot$ black hole. This value is well exceeded by $J_{\rm sink}$ of both sinks. *Right*: Sink rotational velocity, $v_{\rm sink}$, measured at $r = r_{\rm acc}$ (with sink A denoted by a solid black line, and sink B by a dashed black line). Values for $v_{\rm sink}$ are recorded as the mass-weighted average of $v_{\rm rot}$ for all accreted particles. The upper (green) lines for each line type represent the velocity needed for centrifugal support, $v_{\rm cent}$. Note that $v_{\rm sink}$ stays at a nearly constant fraction of $v_{\rm cent}$.

rotation rates. In the latter half of the simulation, $J_{\rm sink}$ for sink B approaches $J_{\rm break-up}$, while sink

A easily surpasses $J_{\rm break-up}$ (red line in Fig. 4.2). If all of sink A's angular momentum became confined to smaller stellar scales this would thus be unphysical. This becomes even more apparent after an analogous examination of sink A's rotational velocity. At the end of the simulation, sink A has a rotational velocity of $v_{\rm sink} = 11$ km s^{-1}. We can extrapolate $v_{\rm sink}$ to the stellar scale of 5 $\mathrm{R}_{\odot}$ by assuming conservation of angular momentum to find $v_* = v_{\rm sink} r_{\rm acc}/5\mathrm{R}_{\odot}$. This turns out to be over 20,000 km s^{-1}, significantly greater than our typical stellar break-up velocity[2], $v_{\rm break-up} \simeq \sqrt{G\,100\mathrm{M}_{\odot}/5\mathrm{R}_{\odot}} \simeq$ 2000 km s^{-1} Again, this is unphysical, and serves as an example of the classic angular momentum problem in the context of star formation (e.g. Spitzer 1978; Bodenheimer 1995), now extended to the immediate protostellar environment.

Further insight can be found by evaluating the centrifugal radius,

$$r_{\rm cent} = \frac{j_{\rm sink}^2}{G M_{\rm sink}}, \tag{4.2}$$

where $j_{\rm sink} = J_{\rm sink}/M_{\rm sink}$. For sink A, in the latter part of the simulation $j_{\rm sink}$ is typically around 8×10^{20} cm^2 s^{-1}, while sink B has $j_{\rm sink} \simeq 3 \times 10^{20}$ cm^2 s^{-1}. At the end of the calculation, $r_{\rm cent} \simeq 10\,\mathrm{AU}$ for sink A and $r_{\rm cent} \simeq 6\,\mathrm{AU}$ for sink B, around two orders of magnitude larger than the stellar sizes cited above. At a length scale of $r_{\rm cent}$, contraction would be halted by the centrifugal barrier, and a disk would form. Accretion onto the star would then continue through the disk, and the disk is expected to grow in size. As mentioned above and described in Stacy et al. (2010), in the simulation a disk structure does indeed form and grow well beyond the sink radius. Other very high-resolution simulations also find that primordial gas develops into disks on small scales, less then 50 AU from the star (Clark et al. 2008, Clark et al. 2011a).

---

[2] The formally correct equation for break-up velocity is $v_{\rm break-up} = \sqrt{\frac{2}{3} G\,M/\mathrm{R}}$, where the factor of $\frac{2}{3}$ accounts for deformation due to rotation. However, due to the approximate nature of our calculations, for simplicity we omit this factor of $\frac{2}{3}$ from our calculations.

We therefore infer that much of the angular momentum of the sinks will be distributed in a disk, while most of the sink mass lies within the small $\simeq 5\,\mathrm{R}_\odot$ star. There is evidence for the existence of similar disk structure around massive stars in the Galaxy (see, e.g. Cesaroni et al. 2006; Kraus et al. 2010). The nature of the disk can be estimated through a comparison of the thermal energy with the kinetic energy of rotational and radial motion at the sink accretion radius. For gas flow onto a gravitationally dominant central mass, dimensionally the sum of these energies per unit mass, should follow the approximate relation (e.g. Narayan and Yi 1994),

$$v_{\rm rot}^2 + v_{\rm rad}^2 + c_{\rm s}^2 \sim \frac{G\,M_{\rm sink}}{r_{\rm acc}} \equiv v_{\rm cent}^2. \tag{4.3}$$

Since sink A is the dominant mass, the above relation will more accurately apply to sink A than to sink B, but the energy comparison remains useful for both. Fig. 4.3 shows these energies for each sink relative to its specific gravity, or $v_{\rm cent}^2$, and how these ratios evolve over time. Overall sink ratios were calculated using a mass-weighted average over the individual particles accreted. For sink A, the rotational energy strongly dominates after $\sim$ 300 years and stays dominant for the rest of the simulation. For sink B, the thermal energy and energy of radial motion remain at similarly low values throughout most of the sink's accretion. Around 500 years after sink B forms, the rotational energy becomes the largest contribution to the total sink energy, and this dominance

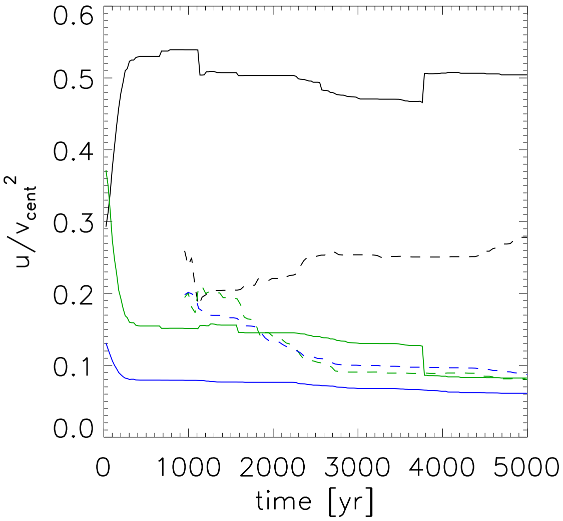

Figure 4.3: Ratio of the energy of sink-accreted particles to the specific gravitational energy of the sinks ($v_{\rm cent}^2 = GM_{\rm sink}/r_{\rm acc}$). Solid lines are for sink A, and dashed lines are for sink B. Upper (black) lines of each line type represent the energy of rotational motion, middle (green) lines represent the energy of radial motion, and lower (blue) lines represent thermal energy. For both sinks, the rotational energy component dominates for the majority of the accretion time, and a thin Keplerian disk is likely to develop on sub-sink scales.

steadily grows for the rest of the calculation. This relatively large amount of rotational energy and low amount of thermal and radial energy for both sinks implies that their sub-sink disks will become thin and Keplerian.

A comparison of the cooling time, $t_{\rm cool}$, with the timescale for angular momentum loss, $t_{\rm am}$, of the gas around the sinks gives further supporting evidence for sub-sink, thin, Keplerian disks. We calculate $t_{\rm am}$ directly from the simulation by recording the acceleration on each gas particle and determining the torque due to numerical viscosity ($\vec{\tau}_{\rm visc}$) as well as the torque exerted by gravity and pressure ($\vec{\tau}_{\rm grav}$ and $\vec{\tau}_{\rm pres}$). The total torque on a given particle within a gas cloud is given by

$$\begin{aligned}\vec{\tau}_{\rm tot} &= \vec{\tau}_{\rm grav} + \vec{\tau}_{\rm pres} + \vec{\tau}_{\rm visc} \\ &= m_{\rm SPH}\vec{d} \times \left(\vec{a}_{\rm grav} + \vec{a}_{\rm pres} + \vec{a}_{\rm visc}\right) \ , \end{aligned} \tag{4.4}$$

where

$$t_{\rm am} \simeq J_{\rm SPH}/|\vec{\tau}_{\rm tot}| \ , \tag{4.5}$$

and

$$t_{\rm cool} \simeq \frac{nk_{\rm B}T}{\Lambda} \ , \tag{4.6}$$

with $k_{\rm B}$ being the Boltzmann constant, T the gas temperature, and Λ the cooling rate (in erg cm^{-3} s^{-1}). We find that $\vec{\tau}_{\rm grav}$ and $\vec{\tau}_{\rm pres}$ dominate, accounting for 80% of the total. Fig. 4.4 shows the z-component, perpendicular to the disk plane, of the specific torque acting upon the gas within the large-scale disk, as measured from the location of sink A. The spiral structure indicates the dominance of gravitational torques which remove angular momentum from the center of the disk on timescales of $100-1000$ years, enabling disk material to be accreted onto the sinks.

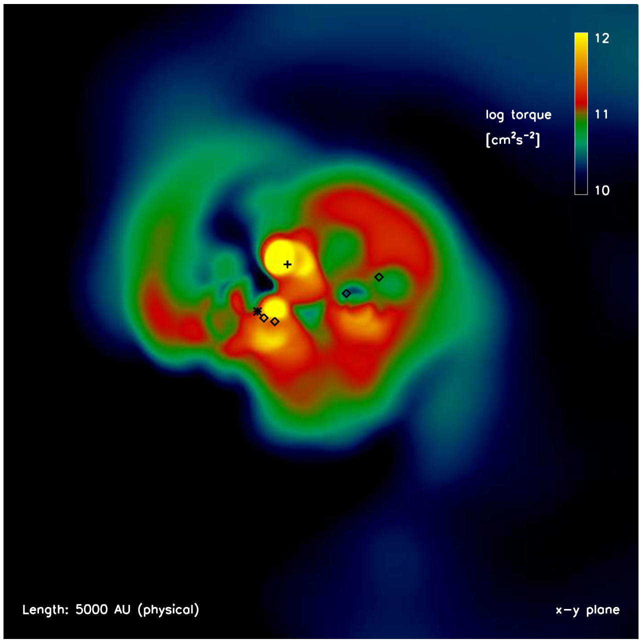

Figure 4.4: Specific torque acting on the gas within the central 5000 AU of the simulation box, the region enclosing the large-scale star-forming disk. Torques are calculated at a representative time of 2500 years after the first sink forms. Shown is the z-component, perpendicular to disk plane, of all contributions to specific torque as measured from sink A. The asterisk denotes the location of sink A, the cross denotes the location of sink B, and the diamonds are the locations of the remaining lower-mass sinks. There is a total of six sinks, but this number will later be reduced through sink mergers. Note the spiral structure, where gravitational torques will remove angular momentum from the disk center on a timescale of approximately 100-1000 years.

Fig. 4.5 shows these timescales for the gas particles in radially averaged bins. From this we can see that for the gas surrounding each sink, $t_{\rm cool} \sim t_{\rm am}$ at distances greater than 1000 AU. However, at 1000 AU $t_{\rm cool}$ falls below $t_{\rm am}$. This coincides well with the fact that this is the radius of the large-scale disk which embeds the whole stellar multiple system. At the sink edges, $t_{\rm cool}$ is nearly an order of magnitude shorter than $t_{\rm am}$ for both sinks. Thermal energy of the gas is radiated away quickly enough that rotational energy will likely remain dominant. Though torques are active, particularly gravitational ones from the spiral structure in the disk, they are unlikely to remove angular momentum quickly enough to prevent the formation of a sub-sink Keplerian disk once the central stellar mass has grown substantially.

4.3.2.2 Extrapolation to Stellar Surface

If the entire extent of the sub-sink disks is indeed Keplerian and the disk self-gravity is negligible, then gas within the sinks will rotate at $v(r) \simeq v_{\rm Kep}(r) \simeq \sqrt{GM_*/r}$, where r is the distance from the star, $M_* = f_* M_{\rm sink}$ is the mass of the star, and f_* is the sink mass fraction that ends up in the star while the remaining mass is stored in the disk. For $f_* \lesssim 1$, we will have $v(r) \lesssim \sqrt{GM_{\rm sink}/r}$. If the inneredge of the disk extends all the way to the stellar surface, which isexpected if magnetic fields are not important (see Chapter 4.6), then the gasacquired by the star from the accretion disk will be rotating at fullKeplerian velocity. a typical predicted size for a massive main-sequence (MS) Pop III star, and $R_* = 100\ {\rm R}_\odot$, a larger size expected for a Pop III protostar that has not yet begun Kelvin-Helmholtz contraction (Omukai and Palla 2003). For sink A, the protostar will have a rotational velocity up to $\gtrsim 200$ km s^{-1}, while the corresponding velocity will be ~ 100 km s^{-1} for

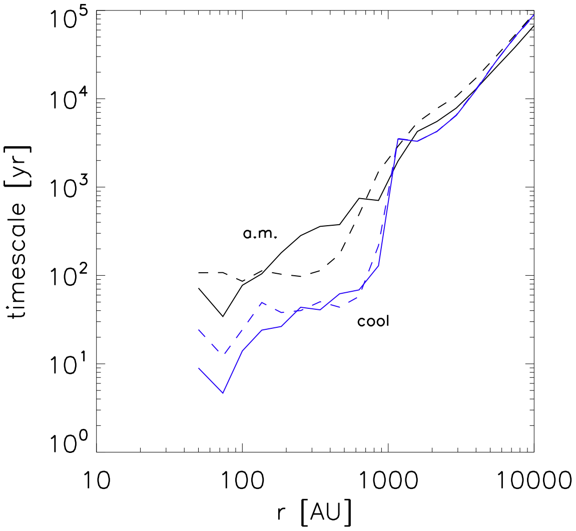

Figure 4.5: Radially averaged timescales versus distance from the sink at a typical accretion time of 2500 years. The cooling timescale, $t_{\rm cool}$, is shown in blue as the lower set of lines, and the angular momentum loss timescale, $t_{\rm am}$, is shown in black as the upper set of lines. Solid lines are for sink A, and dashed lines are for sink B. For both sinks, $t_{\rm cool}$ is an order of magnitude shorter than $t_{\rm am}$ from the sink edge out to $\sim$ 1000 AU, the edge of the large-scale disk.

sink B. Once on the MS, the sink A star will rotate at $\gtrsim 1000$ km s^{-1}, while the sink B star will rotate at ~ 550 km s^{-1}.

The location of the stellar surface varies as the star's radius evolves. The total angular momentum acquired by the star will depend upon this evolution, and at any given time this total J_* is given by

$$J_*(t) = \int_0^t j(R_*)\dot{M}\,dt = \int_0^t \sqrt{GM_*R_*}\dot{M}\,dt \ , \tag{4.7}$$

where R_* is the radius of the star. To evaluate this expression, we use the same prescription for the protostellar radial evolution as described in Stacy et al. (2010), which in turn was based upon the earlier work of, e.g. Stahler et al. (1986) and Omukai and Palla (2003). In this prescription, when the protostar first forms as a small hydrostatic core, it will initially undergo a phase of adiabatic accretion and gradual expansion. During this time the protostellar radius will grow as

$$R_{*I} \simeq 50\mathrm{R}_\odot \left(\frac{M_*}{\mathrm{M}_\odot}\right)^{1/3} \left(\frac{\dot{M}}{\dot{M}_{\mathrm{fid}}}\right)^{1/3} \ , \tag{4.8}$$

where $\dot{M}_{\mathrm{fid}} \simeq 4.4 \times 10^{-3}\mathrm{M}_\odot\,\mathrm{yr}^{-1}$ is a fiducial rate, typical for Pop III accretion. During the subsequent phase of Kelvin-Helmholtz (KH) contraction, the radius will shrink according to

$$R_{*II} \simeq 140\mathrm{R}_\odot \left(\frac{\dot{M}}{\dot{M}_{\mathrm{fid}}}\right) \left(\frac{M_*}{10\mathrm{M}_\odot}\right)^{-2} \ . \tag{4.9}$$

We estimate that the transition from adiabatic accretion to KH contraction occurs when the value of R_{*II} falls below that of R_{*I}. For M_* and $\dot{M}$ we employ the power-law fits discussed in Chapter 4.3.1, and we set $M_* \simeq M_{\rm sink}$ in the following analysis. In doing this we have made the simplifying assumption that nearly all of the gas accreted onto the sink quickly flows through the relatively low-mass disk onto the dominating massive star. We also extend the fits to 10^5 years, roughly the point when KH contraction will cease and the star settles onto the MS, with a final radius of $5\,{\rm R}_\odot$. Although the Pop III radial evolution and MS size is based on work that does not account for varying accretion rates and stellar rotation, which may inflate the radius, this should still give a general picture of how the Pop III rotational velocity will evolve.

The resulting evolution of $v_* = J_*/R_*$ for each sink is shown in Fig. 4.6. Note that during the stars' initial slow expansion, the velocity is not quite at break-up because the stars are gathering mass from gradually increasing radii. Once the stars begin KH contraction, however, the total angular momentum of the stars in fact exceeds break-up, but in this case we assume that the angular momentum will slow the KH contraction accordingly, and we adjust the stellar radius such that the star will again rotate at break-up speed. By setting the right-hand side of Equ. (4.7) equal to $J_{\rm Kep}$, we find that the radius during this third slowed contraction phase will evolve according to

$$\frac{d}{dt}\ln R_{*III} = -\frac{d}{dt}\ln M \tag{4.10}$$

Once this phase begins, the star will rotate at break-up speed, $v_* = v_{\rm max} \simeq \sqrt{GM_{\rm sink}/R_*}$.

Given this model, at 10^5 years the star within sink A has mass of 125 ${\rm M}_\odot$, a radius of 7 ${\rm R}_\odot$, and a rotational velocity of 1800 km ${\rm s}^{-1}$. The star within sink B has mass of 15 ${\rm M}_\odot$, a radius of 12 ${\rm R}_\odot$, and a rotational velocity

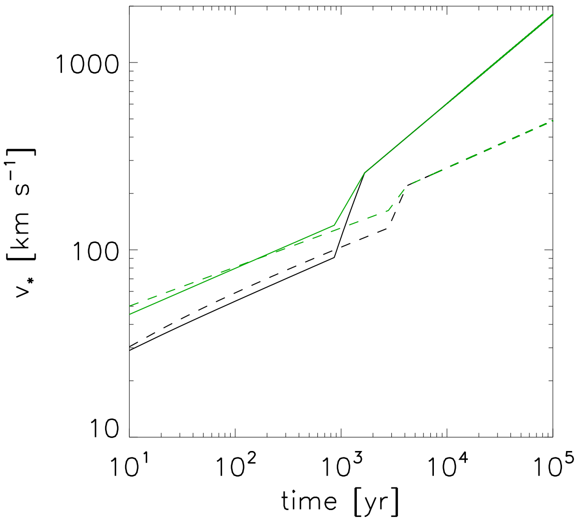

Figure 4.6: Evolution of stellar rotation. Lower black lines show the rotational velocities v_* of the stars as they initially grow slowly through adiabatic accretion and then undergo KH contraction onto the MS. Upper green lines are the break-up velocities of the stars, $v_{\rm max} \simeq \sqrt{GM_{\rm sink}/R_*}$. Solid lines are for sink A, and dashed lines are for sink B. Note that once KH contraction begins at around 1000 years for sink A and 3000 years for sink B, both stars quickly spin up to the full break-up velocity.

of 500 km s^{-1}. Though details of this model are uncertain, particularly how the accretion rate will evolve during later times beyond the end of our simulation, we can still expect spin-up to occur during KH contraction, likely yielding rotational velocities near break-up speed.

We can also make a more conservative estimate to represent the possible case that sub-sink torques do become strong enough to yield sub-Keplerian rotation rates. Since the overall sink angular momentum stays at a fairly constant fraction of $J_{\rm cent}$, we can apply this to sub-sink scales as well. Then we have $v(r) = \epsilon\, v_{\rm Kep}(r) = \epsilon\sqrt{GM_{\rm sink}/r}$. This is similar to the situation described by Narayan and Yi (1994) in which the gas cannot cool efficiently, causing the accretion flow to stay at approximately the virial temperature. The resulting viscosity is high relative to cold gas, allowing angular momentum to be transported outwards and leading to rotational velocities that remain at a constant fraction $\epsilon < 1$ of $v_{\rm Kep}(r)$ for a large range of radii. At 10^5 years, given $\epsilon = 0.45$ (see Fig. 4.1), the star within sink A will be rotating at $v_{*,\rm low} \simeq 800$ km s^{-1} (see Fig. 4.6). This is still a high rotational velocity that is a substantial fraction of the break-up speed. The fastest-rotating stars considered by Woosley and Heger (2006) and Yoon and Langer (2005), for instance, had ϵ values of 0.45 - 0.5. The sink B star would not rotate quite as rapidly due to its lower mass and its slightly lower values of ϵ, but for $\epsilon = 0.35$ the sink B star is still estimated to reach a significant rotational velocity of $v_{*,\rm low} \simeq 300$ km s^{-1}. Also note that, in the conservative case, $v_{\rm max}$ at 10^5 years is slightly higher than that shown in Fig. 4.6 because KH contraction is no longer slowed by excess angular momentum, and the stars have already reached the MS radius by this time. We summarize these estimates for stellar masses and rotation rates in Table 4.1.

sink	$M_*(5000\,\mathrm{yr})$ [$\mathrm{M}_\odot$]	$M_*(10^5\,\mathrm{yr})$ [$\mathrm{M}_\odot$]	j_{sink} [cm^2/s]	v_* [km/s]	$v_{*,\mathrm{low}}$ [km/s]
A	34	125	8×10^{20}	1800	800
B	9	15	3×10^{20}	500	300

Table 4.1: Stellar masses at 5000 years, extrapolated mass at 10^5 years, specific angular momenta of the sinks, final stellar rotational velocities v_*, and the more conservative estimate of stellar rotational velocity $v_{*,\mathrm{low}}$.

4.4 Implications of Rapid Rotation

4.4.1 Rotational Mixing

Numerous previous studies have found that high rotational velocities such as those predicted from our simulation will alter the stellar evolution (see, e.g. Maeder and Meynet 2000). Models of Maeder (1987), for instance, find that above a critical velocity of 350 km s^{-1} for 20 $\mathrm{M}_\odot$ stars (or 30-40% of break-up velocity), rotationally induced mixing will lead to a very different evolution. Instead of the expected redward track off the MS in the HRD, mixing reduces the chemical gradient throughout the star enough that no extended hydrogen envelope forms. The star smoothly transitions from hydrogen to helium burning, and the stellar radius stays roughly constant while the temperature and luminosity both steadily increase. The star then enters the WR stage, during which heavy mass loss leads to a decrease in the luminosity, though the temperature still remains high. As will be further discussed in the next section, updated studies by Yoon and Langer (2005) and Woosley and Heger (2006) of low-metallicity stars, and also studies by Heger and Langer (2000) of solar-metallicity stars, all similarly find that massive stars with high rotation rates ($\sim$ 40-50% of break-up speed) can undergo chemically homogeneous evolution to become rapidly rotating WR stars.

Rotational mixing is likely to occur according to the calculations we

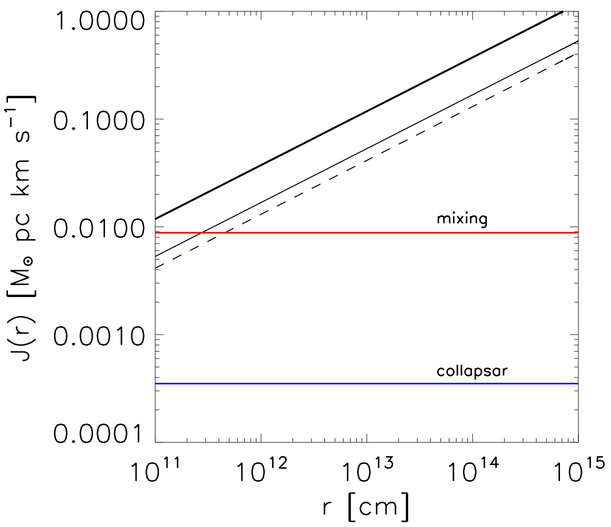

Figure 4.7: Angular momentum relative to the center of the stars, assuming they have grown to a mass of 100 $M_\odot$ and have an approximate radius of 5 $R_\odot$. Thick black solid line represents the situation of Keplerian rotation where $J(r) = J_{\rm Kep}(r)$. The thin diagonal lines represent the case of $J(r) = \epsilon\, J_{\rm Kep}(r)$. For sink A (solid line), $\epsilon = 0.45$ was used. For sink B (dashed line), we used a smaller value of $\epsilon = 0.35$. Blue line (labeled as "collapsar") shows $J_{\rm ISCO}$. Red line (labeled as "mixing") shows $0.4 * J_{\rm break-up}$, the approximate minimum angular momentum necessary for a low-metallicity star to undergo rotational mixing and chemically homogeneous evolution, as determined by Yoon and Langer (2005) and Woosley and Heger (2006). The angular momentum requirement for the collapsar engine, $J > J_{\rm ISCO}$, is easily met on sub-sink scales. Rotational mixing will readily occur as well as the stars approach their break-up speed.

present here, particularly if the stars do indeed rotate at nearly full break-up speed (see Fig. 4.7). This will have important implications for Pop III feedback. Effective temperatures of stars that undergo such rotational mixing can reach up to an order of magnitude higher than corresponding non-rotating stars, while luminosities may be two to three times as high (see, e.g. Yoon and Langer 2005). This will lead to an increased emission of ionizing radiation at harder wavelengths, so the HII regions will be larger than expected from non-rotating models of stars of the same mass (e.g. Greif et al. 2009).

It is important to note that these results do vary depending upon metallicity and details of the stellar model. For instance, in contrast to earlier studies, Ekström et al. (2008a) find that even rotational speeds of up to 70% of break-up speed will not be sufficient to drive chemically homogeneous evolution. However, they do find rotation to increase the MS lifetime by 10-25%, which again would increase the total amount of ionizing radiation from rotating massive Pop III stars. A final distinction between rotating and non-rotating Pop III evolution is that rotating models generally yield higher total amounts of metals by the end of their nucleosynthesis (Ekström et al. 2008a). Depending on how this metallicity gets spread to the star's surroundings through stellar winds and SN explosions, higher metallicity will enhance the later cooling and collapse of gas when subsequent generations of stars form, most likely lowering their average mass (e.g. Omukai 2000; Bromm et al. 2001b; Schneider et al. 2006; Frebel et al. 2007, 2009; Greif et al. 2010)

4.4.2 GRBs and Hypernovae

The final fate of the stars in our simulation will depend on the mass they reach through accretion, though computational limitations prevent us from following the entire accretion history over the stellar lifetime of ~ 3 Myr. However, extrapolating from the first 5000 years (see Fig. 4.1) implies that both stars we have discussed are likely to grow significantly more massive. They should certainly be massive enough to avoid a white dwarf fate and make a neutron star or black hole, assuming they do not die as PISNe and leave behind no remnant at all. If they in fact die as core-collapse SNe, we can estimate the effect of rotation on the later SN explosion. Though a black hole remnant is more likely, particularly for the more massive star of sink A, we can derive a more conservative estimate by considering a neutron star remnant. As described in Woosley and Heger (2006), the total rotational energy of a resulting neutron star of radius 12 km and gravitational mass of 1.4 $\mathrm{M}_{\odot}$ will be $E_{\mathrm{rot}} \simeq 1.1 \times 10^{51}\,(5\,\mathrm{ms}/P)^2$ erg, where P is the rotation period of the neutron star. They find that for E_{rot} to be comparable to the energy of a hypernova, $\sim 10^{52}$ erg, P would need to be ≤ 2 ms. In their low-metallicity models that begin with stars rotating with similar ϵ values to what we found for sink A ($\epsilon \sim 0.45$), they infer resulting neutron star rotation rates that do meet this criterion. They find the same results even for lower ϵ like for those of sink B, though this is only if magnetic torques are not included in the model. Thus, even using the more conservative estimate it is conceivable that the rotational energy reservoir found in sink A and B of our work could be enough to power a hypernova. If the stars rotate more rapidly, at nearly their break-up velocity as we predict, then hypernovae would be even more likely.

Will there still be enough angular momentum for the collapsar engine to work on these stellar scales? If we use the low estimate of $J(r) = \epsilon\, J_{\mathrm{Kep}}(r) = \epsilon \sqrt{G M_{\mathrm{sink}}\, r}$, then on these scales the angular momentum for both sinks still easily meets the required $J > J_{\mathrm{ISCO}}$, especially if their high ϵ values continue as the stars grow to larger masses (see Fig. 4.7). But will such stars retain this angular momentum as they evolve? Low metallicity stellar models in Yoon and Langer (2005) and Woosley and Heger (2006) that were initialized with ϵ values similar to that of sink A show that such stars may indeed be able to retain sufficient amounts of angular momentum in their cores throughout their evolution to the pre-SN stage, depending upon the strength of magnetic fields and the mass loss rate during the WR stage. Though there is still some angular momentum loss in their GRB-forming models, it is limited because rotationally induced mixing allowed these stars to avoid a red giant phase on their path to becoming WR stars. However, Woosley and Heger (2006) generally find that when both magnetic fields and strong mass loss are included in their models, the ability of even their high-ϵ models to meet the GRB requirements becomes borderline.

For the lower ϵ value of 0.35 as found for sink B, a GRB becomes yet less likely, and the star cannot even go through a WR phase unless the models exclude magnetic fields. However, as discussed in Chapter 4.3.2, the stars within both sink A and sink B are expected to rotate at a much higher fraction of break-up speed - close to 100%. In this case, the above path for becoming a GRB should work yet more readily. Unless there are mechanisms for significant angular momentum transport away from the stars (see Chapter 4.6), the angular momentum condition for the collapsar engine will be met.

4.5 Sub-Sink Fragmentation

Up to this point we have assumed that each sink will host a single star-disk system, but it is possible that more than one star could exist inside a sink. For instance, a sink merger might lead to a sub-sink binary instead of the presumed coalescence of two stars. We may also consider the possibility that the mass of the sink will fragment and a sub-sink stellar multiple will form in this way. As described by Jappsen and Klessen (2004), this is more likely for higher values of β, the ratio of rotational to gravitational energy. As in Goodman et al. (1993) and Jappsen and Klessen (2004), we can arrive at a simple estimate by assuming that the sinks are undergoing solid-body rotation, have constant angular velocity Ω, and have uniform density. In this case, sink A has $\Omega = 1.5 \times 10^{-9}$ s^{-1} and sink B has $\Omega = 6 \times 10^{-10}$ s^{-1}. We also have

$$\beta = \frac{(1/2)\, I\Omega^2}{qGM^2/R}, \tag{4.11}$$

where $I = pMR^2$ is the moment of inertia, $p = 2/5$, and $q = 3/5$. In this case sink A has $\beta = 0.070$ and sink B has $\beta = 0.044$, very similar to the values derived for the sinks in Jappsen and Klessen (2004). The requirement for fragmentation ranges from $\beta > 0.01$ to $\beta > 0.1$, depending on the true density structure and thermal properties of gas on sub-sink scales, as well as the effects of magnetic fields (e.g. Boss and Myhill 1995; Boss 1999). For the above values of β, it is thus not entirely certain whether subfragmentation would occur, and this will need to be determined with higher resolution studies.

As discussed earlier, however, disk structure is expected even on sub-sink scales, so it would also be appropriate to examine the Toomre criterion for disk fragmentation:

$$Q = \frac{c_{\rm s}\kappa}{\pi G\Sigma} < 1\ . \tag{4.12}$$

Here, Σ is the disk surface density and κ the epicyclic frequency, which is equal to the angular velocity for a disk undergoing Keplerian rotation. However, evaluating Q would require knowledge of disk temperature and surface density on sub-sink scales, which is not available. As discussed in Chapter 4.3.2, cooling is likely to occur faster than angular momentum transport, leading to a sub-sink Keplerian disk. However, gas within these inner regions is more susceptible to heating and other protostellar feedback. This makes disk fragmentation more likely to occur in the cooler outer regions of the disk on scales much larger than the sinks, and indeed such fragmentation is seen in the simulation. Similar points were made in studies such as Kratter and Matzner (2006) and Krumholz et al. (2007).

If a sub-sink binary were to form, however, this could be yet another pathway towards a GRB. As discussed in studies such as Fryer et al. (1999), Bromm and Loeb (2006), and Belczynski et al. (2007), a binary that is tight enough can allow Roche lobe overflow and a common-envelope phase to occur. This will remove the hydrogen envelope of the primary, fulfilling one of the requirements for a collapsar GRB. Even if the stars are rapid rotators, however, Belczynski et al. (2007) find that Pop III binaries will yield GRBs in only a small fraction, $\lesssim 1\%$, of cases. Tidal interactions rarely spin up one of the binary members sufficiently to produce a GRB, and in fact such interactions more often cause the binary members to spin down.

On the other hand, if a wide 50 AU binary were to form within the sinks, this may still leave enough angular momentum for a GRB to form through the rotational mixing pathway. The total angular momentum that will go into the binary orbit will be

$$J_{\mathrm{orb}} = M_1 M_2 \frac{\sqrt{aG\left(M_1 + M_2\right)\left(1 - e^2\right)}}{M_1 + M_2}, \tag{4.13}$$

where a is the semimajor axis of the orbit, e is the eccentricity, and M_1 and M_2 are the stellar masses (e.g. Belczynski et al. 2007). If sink A becomes a circular-orbit binary with $M_1 = M_2 = 17\ \mathrm{M}_\odot$, then $J_{\mathrm{orb}} = 5 \times 10^{-2}\,\mathrm{M}_\odot$ pc km s^{-1}, about 50% of $\mathrm{J}_{\mathrm{sink}}$ for sink A at the end of the simulation. If the remaining angular momentum went to the spin of each of the binary components, a GRB may still be able to form.

4.6 Summary and Discussion

We evolved a three-dimensional SPH cosmological simulation until the formation of the first minihalo at $z = 20$, and then followed the evolution of the minihalo gas up to maximum density of 10^{12} cm^{-3}. After this point we used the sink particle method to continue the simulation for 5000 years. A large-scale thick disk of order 1000 AU that formed around the main sink was resolved and so the calculation was able to follow angular momentum transport that occurred within this disk down to resolution length scales of 50 AU. We find that there is sufficient angular momentum in Pop III star-forming cores, represented by the sink particles, to yield rapidly rotating Pop III stars. More specifically, we find that the star-disk systems are likely to rotate at Keplerian speeds. This leads to stellar rotational velocities that can potentially exceed 1000 km s^{-1} for stars with $M \gtrsim 30\,\mathrm{M}_\odot$. This in turn should lead to chemically homogeneous evolution, yielding hotter and more luminous stars than without rotation. The stars should also retain sufficient spin to power hypernovae as well as collapsar GRBs (e.g. Nomoto et al. 2003; Yoon and Langer 2005; Woosley and Heger 2006). Such GRBs may be observed by the *Swift* satellite, which has already detected GRBs at a redshift as high as $z \approx 8.2$ (Salvaterra et al. 2009; Tanvir et al. 2009), and may also be detected by possible future missions such as JANUS and EXIST.

We emphasize the caveat that we did not fully resolve stellar scales. We have measured the total angular momentum accreted within $r_{\rm acc} \simeq 50$ AU of the star, and we have argued that a Keplerian disk and perhaps a binary is expected to form on sub-sink scales, still leaving enough angular momentum for one or two rapidly rotating stars. However, there are further processes which can transport angular momentum away from rotating stars. For instance, angular momentum may be lost through stellar winds, but the mass and angular momentum loss through winds is expected to be much lower for low-metallicity and Pop III stars than for higher-metallicity stars (Nugis and Lamers 2000; Kudritzki 2002). Other processes include disk torques induced by gravitational instability as well as viscous torques, which have a variety of sources including hydromagnetic instability (see, e.g. Papaloizou and Lin 1995 for a review).

In particular, the magneto-hydrodynamic (MHD) aspect of Pop III star formation is still very uncertain (e.g. Maki and Susa 2007), and we therefore here neglect any angular momentum loss due to magnetic torques. Earlier work, however, gives some hint as to the possible effect of magnetic fields. Machida et al. (2008) conclude that if a star-forming primordial cloud has a large enough initial magnetic field ($B > 10^{-9}\,[n/10^{3}\mathrm{cm}^{-3}]^{2/3}$ G), a protostellar jet will be driven provided that the cloud's rotational energy is less than its magnetic energy. However, Xu et al. (2008) find that the Biermann battery mechanism and flux freezing alone will not amplify magnetic fields in a collapsing halo quickly enough to reach this threshold value. In contrast, small-scale dynamo amplification as described by Schleicher et al. (2010) could generate sufficient magnetic fields for the magneto-rotational instability (MRI) to operate in primordial protostellar disks (e.g. Balbus and Hawley 1991). The resulting turbulent viscosity would facilitate outward angular momentum transfer in the disk, and it may further allow generation of sufficient magnetic field strength to drive collimated protostellar outflows that can also remove angular momentum (e.g. Tan and Blackman 2004; Silk and Langer 2006). This may furthermore facilitate some form of 'disk-locking' as described by various authors such as Koenigl (1991), Shu et al. (1994), and Matt and Pudritz (2005), where the stellar rotation will be 'locked' to a rate given by the star's mass, accretion rate, magnetic field strength, and radius. Such a model was described by Koenigl (1991), for example, to yield $\Omega_* \sim GM_*^{5/7}\dot{M}^{3/7}B^{-6/7}R_*^{-18/7}$, where Ω_* is the star's angular velocity and B the stellar magnetic field strength. In short, the rate at which these effects will remove angular momentum from the star is very dependent on the still uncertain magnetic field strength in Pop III star forming regions, although such effects are a likely part of the explanation for slowly rotating stars observed in the Galaxy (see, e.g. Bodenheimer 1995). Whether this also applies in the early Universe will be best determined through future numerical simulations. A three-dimensional cosmological simulation that can resolve stellar scales and follow MHD processes for many dynamical times is highly computationally demanding. For the moment, our preliminary calculation provides an upper limit for the Pop III stellar rotation rate.

A comparison with Jappsen and Klessen (2004) shows interestingly similar results. The average specific angular momentum of their protostellar objects was 8×10^{19} cm^2 s^{-1}, and the typical mass of each object was $\simeq 1$

$M_\odot$. They find that the specific angular momentum increases with mass, with $j \propto M^{2/3}$ being their preferred fit. Our sink particles are 9 and 34 times more massive and so should have specific angular momenta about 4 and 10 times higher, or $3 - 8 \times 10^{20}$ cm^2 s^{-1}. This is indeed the specific angular momentum measured for our sinks. This also compares well with the range of observed angular momenta of various structures in the Milky Way. For instance, the average specific angular momentum of binaries in the Taurus star-forming region was found by Simon et al. (1995) to be $j \simeq 2 \times 10^{20}$ cm^2 s^{-1}, and similar values were found for G-dwarf stars by Duquennoy and Mayor (1991). For less-evolved structures, Caselli et al. (2002) found an average of $j = 7 \times 10^{20}$ cm^2 s^{-1} for cores of mean mass of 6 $M_\odot$. Goodman et al. (1993) observed larger cores of approximately 50 $M_\odot$ and obtained an average of $j \simeq 2 \times 10^{21}$ cm^2 s^{-1}. These cores would be expected to lose angular momentum as they evolve into protostars, leading to smaller values similar to those observed in stellar binaries. Despite the different initial conditions which give rise to Pop III stars versus stars in our Galaxy, the overall angular momentum reservoir for both is very similar. Thus, just as rapidly rotating massive stars are observed today (e.g. Huang and Gies 2008; Wolff et al. 2008), rapidly rotating massive stars seem likely to exist in the early Universe as well. Unless they are spun down by processes such as magnetic torques or bipolar outflows, such rapid rotation rates must play an important role in the evolution and final state of the first stars.

Chapter 5

Effect of Streaming Motion of Baryons Relative to Dark Matter on the Formation of the First Stars[1]

5.1 Overview

The formation of the first stars was a key event in the evolution of the early universe (e.g. Barkana and Loeb 2001; Bromm and Larson 2004; Ciardi and Ferrara 2005; Glover 2005; Bromm et al. 2009; Loeb 2010). After the emission of the Cosmic Microwave Background at $z \sim 1000$, the universe entered the 'Dark Ages,' the period when the distribution of matter was very uniform and no luminous objects had yet formed. During this time, cold dark matter (DM) density perturbations grew to make the halos inside of which the first stars formed at $z \lesssim 50$. These stars are believed to have formed within $M \sim 10^6\,\mathrm{M}_\odot$ minihalos, where the infall of the baryons into the gravitational potential well of the DM-dominated minihalo heated the gas sufficiently to enable H_2-driven cooling and fragmentation (e.g. Haiman et al. 1996; Tegmark et al. 1997; Yoshida et al. 2003).

The initial growth of the density fluctuations after recombination can be described using linear perturbation theory, which assumes that overdensities and velocity fields are small quantities. Similarly, cosmological simulations are initialized at high z with small gas and DM peculiar velocities, determined through a combination of the ΛCDM model and Zeldovich approximation (Zeldovich 1970). Recently, Tseliakhovich and Hirata (2010) added a complicating aspect to this picture by showing that at high redshift, there is a supersonic relative velocity between the baryons and DM. Whereas prior to recombination, photons and baryons are coupled such that the baryonic sound speed is $\sim c/\sqrt{3}$, after recombination the sound speed drops to ~ 6 km s^{-1}. The root-mean square relative velocity, on the other hand, is much higher, 30 km s^{-1}. The relative velocities are dominated by modes on the comoving scale of ~ 150 Mpc, the length scale of the sound horizon at recombination, and are coherent on smaller scales of a few Mpc.

---

[1] This chapter has been published as Stacy A., Bromm V., Loeb A., 2011, ApJ, 730, L1

Tseliakhovich and Hirata (2010) examined how this effect alters the growth of DM structure, causing a small ($\sim 10\%$) suppression of the matter power spectrum for modes with wavenumber $k \simeq 200\mathrm{Mpc}^{-1}$. Using the Press-Schechter formalism they have also found a decrease in $M \sim 10^6\,\mathrm{M}_\odot$ minihalos at high redshifts, $z = 40$. They furthermore find that the relative velocity effect yields a scale-dependent bias of the first halos. Extending upon this, Dalal et al. (2010) analytically studied the impact of the relative velocity on baryonic objects, finding that the collapse fraction will be slightly reduced and that the large-scale clustering of $M \lesssim 10^6\,\mathrm{M}_\odot$ minihalos will be modulated on scales of ~ 100 Mpc. The same applies to any observable that traces minihalos, including the 21 cm absorption power spectrum. Tseliakhovich et al. (2010) find similar results in a more detailed analysis.

While these previous studies examined the large-scale effects of the relative velocity, its direct influence on the delay of collapse and the evolution of gas falling into a single minihalo has yet to be considered. Simulations are necessary to understand how the relative streaming affects the non-linear regime and alters the processes involved in the collapse of minihalo gas. To this end, we perform a set of cosmological simulations which include these streaming motions. After the completion of this work, we became aware of an analogous paper by Maio et al. (2010). Similar to Maio et al. (2010), we find a delay of gas collapse in early low-mass $M \sim 10^5 - 10^6\,\mathrm{M}_\odot$ minihalos, but conclude that for typical streaming velocities this delay will be negligible by $z \sim 10$. Our work is complementary to that of Maio et al. (2010) in that, while they are able to find a $1-20\%$ overall suppression of the first objects, our factor of ~ 10 greater mass resolution allows us to see the subsequent collapse of the gas to high densities, revealing that even with relative streaming motions the thermal evolution of primordial gas and subsequent Pop III star formation will be very similar to no-streaming cases following the initial collapse.

5.2 Numerical Methodology

We carry out our investigation using GADGET, a widely-tested three dimensional smoothed particle hydrodynamics (SPH) code (Springel et al. 2001; Springel and Hernquist 2002). Simulations are performed in a periodic box with size of 100 h^{-1} kpc (comoving) and initialized at $z_\mathrm{i} = 100$ with both DM and SPH gas particles. This is done in accordance with a ΛCDM cosmology with $\Omega_\Lambda = 0.7$, $\Omega_\mathrm{m} = 0.3$, $\Omega_\mathrm{B} = 0.04$, and $h = 0.7$. We adopt $\sigma_8 = 0.9$ for the fiducial normalization of the power spectrum, and also examine the case of $\sigma_8 = 1.4$ in which structure formation is accelerated and the first minihalo collapses earlier. Each simulation box contains 128^3 DM particles and an equal number of SPH particles. The gas particles each have a mass $m_\mathrm{SPH} = 8\ \mathrm{M}_\odot$, so that the mass resolution is, $M_\mathrm{res} \simeq 1.5 N_\mathrm{neigh} m_\mathrm{SPH} \lesssim 400$

$M_\odot$, where $N_\mathrm{neigh} \simeq 32$ is the typical number of particles in the SPH smoothing kernel (e.g. Bate and Burkert 1997). This mass resolution allows us to follow the gas evolution to a maximum number density of $n_\mathrm{max} = 10^4$ cm^{-3}.

The chemistry, heating and cooling of the primordial gas is treated in a fashion very similar to previous studies (e.g. Bromm and Loeb 2004; Yoshida et al. 2006). We follow the abundance evolution of H, H^+, H^-, H_2, H_2^+, He, He^+, He^{++}, e^-, and the deuterium species D, D^+, D^-, HD, and HD^+. We use the same chemical network as used in Greif et al. (2010) and include the same cooling terms.

We first perform both the 'standard collapse' ($\sigma_8 = 0.9$) and 'early collapse' ($\sigma_8 = 1.4$) initializations with no streaming velocity added. For each of these we also perform 'moderate' and 'fast' streaming cases in which we include an initial streaming velocity $\mathrm{v_{s,i}}$ of 3 km s^{-1} and 10 km s^{-1}, respectively. The 'moderate' streaming case represents the predicted root mean square velocity (Tseliakhovich and Hirata 2010), given that peculiar velocities have decreased as $(1 + z)$ since recombination and thus have declined by a factor of 10 at the point our simulations are initialized. Our $\mathrm{v_{s,i}}$ values therefore correspond to velocities of 30 km s^{-1} and 100 km s^{-1} at recombination, similar to the velocities chosen by Maio et al. (2010), 30 and 60 km s^{-1}.

5.3 Results

5.3.1 Delay of Gas Collapse

The main effect of the relative streaming cases is to delay the collapse of the baryons into the DM halos. In the standard case, the collapse redshifts are $z_\mathrm{col} = 14.4$, 12.2, and 6.6 for $\mathrm{v_{s,i}} = 0$, 3, and 10 km s^{-1} (0, 30, and 100 km s^{-1} at recombination). The streaming cases correspond to delays in collapse of $\sim 7 \times 10^7$ and $\sim 5 \times 10^8$ years, respectively. In the accelerated collapse case these values are $z_{\rm col} = 23.6$, 21.3, and 12.4, corresponding to delays of $\sim 2 \times 10^7$ and $\sim 2 \times 10^8$ years. Thus, this delay is noticeable only for high initial values of $v_{\rm s,i} \gtrsim 3$ km s^{-1}, whereas at smaller values the delay is small compared to the Hubble time.

We can understand the criterion for gas collapse in terms of the cosmological Jeans mass. In the usual no-streaming case, the slow infall of gas into the halos will first begin when the gravitational potential well of the minihalo, characterized by its virial velocity $V_{\rm vir}$, is large enough to assemble the gas, which occurs when $V_{\rm vir} > c_{\rm s}$, where $c_{\rm s} = \sqrt{k_B T/\mu m_{\rm H}}$ is the sound speed. Once this process begins, the sound speed $c_{\rm s}$ will be coupled to $V_{\rm vir}$ through adiabatic heating (see top panels of Fig. 5.1), and the density will scale with sound speed approximately as $c_{\rm s}^3$. In Fig. 5.1, we determined the properties of the largest halo in our simulation using the HOP technique (Eisenstein and Hut 1998) to find the DM particle in the region of highest DM density. Assuming this particle marks the center of the halo, the extent of the halo was determined by finding the surrounding spherical region in which the average DM density is $200\rho_c$, where ρ_c is the redshift-dependent critical density.

The bottom panels of Fig. 5.1 illustrate that the adiabatic phase of evolution will continue until the virial mass of the minihalo is greater than the Jeans mass of the gas, $M_{\rm vir} > M_{\rm J}$. For the no-streaming case, we calculate $M_{\rm J}$ as

$$M_{\rm J} = \left(\frac{\pi}{6}\right) \frac{c_{\rm s}^3}{G^{3/2}\rho^{1/2}} \ , \tag{5.1}$$

Once the halo gains sufficient mass, and also provided that the $\rm H_2$-driven cooling time $t_{\rm cool}$ of the gas is shorter than its free-fall time $t_{\rm ff}$, the Jeans and

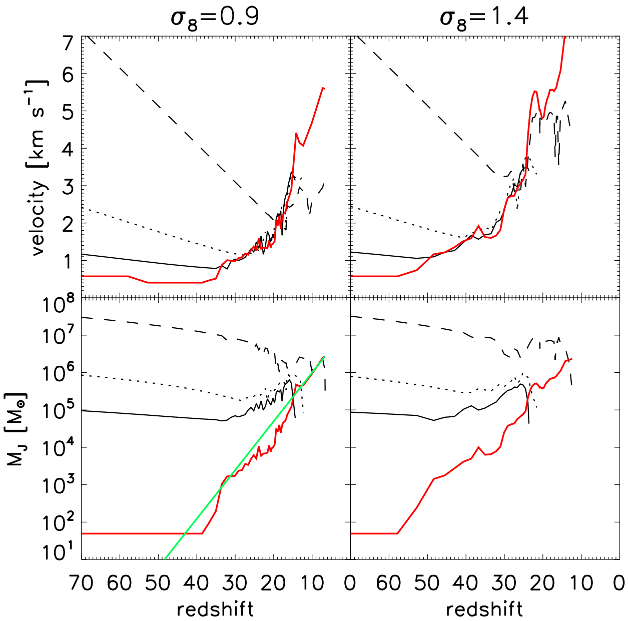

Figure 5.1: *Top panels*: Effective velocity $v_{\rm eff} = \sqrt{c_{\rm s}^2 + {\rm v}_{\rm s}^2}$ of the gas (thin lines) and virial velocity $V_{\rm vir}$ of the simulated minihalo (thick red line). *Top Left*: 'Standard collapse' case. Dashed line: $v_{\rm s,i} = 10$ km s^{-1}, dotted line: $v_{\rm s,i} = 3$ km s^{-1}, solid black line: no-streaming case. At each redshift $v_{\rm s}$ was found by taking an average over the entire gas within the simulation box. $c_{\rm s}$ refers to the average sound speed of all particles within the virial radius of the minihalo. *Top Right*: Early collapse case. Note that for the streaming cases, the redshift at which $v_{\rm eff}$ first falls below $v_{\rm vir}$ matches well with the point where the gas thermal evolution first follows that of $V_{\rm vir}$. *Bottom Panels*: Evolution of the Jeans mass $M_{\rm J}$ with redshift, evaluated using $v_{\rm eff}$ in the role of the effective sound speed. Notation is the same as in the upper panels. Red line: virial mass $M_{\rm vir}$ of the minihalo. Green line: exponential fit to the growth of the 'standard collapse' case minihalo. Gas collapse occurs quickly after $M_{\rm J}$ drops below $M_{\rm vir}$. The enhancement of $v_{\rm eff}$ due to the streaming velocity effectively increases $M_{\rm J}$, causing the gas collapse to be delayed until $M_{\rm vir}$ can further grow. This alters the final gas collapse redshifts of each case ($z_{\rm col} = 14.4$, 12.2, and 6.6 for the no streaming, moderate streaming, and fast streaming cases given 'standard collapse'; $z_{\rm col} = 23.6$, 21.3, and 12.4 for 'early collapse').

cooling criteria will be satisfied and the gas will begin the next phase of rapid collapse to higher densities, quickly reaching $n_{\rm max} = 10^4$ cm^{-3}.

The cause for the delay in collapse of the streaming cases lies in the enhanced effective velocity of the gas,

$$\mathrm{v_{eff}} = \sqrt{c_{\rm s}^2 + \mathrm{v}_{\rm s}^2}\ , \qquad (5.2)$$

where the streaming velocity decreases with redshift as $\mathrm{v_s}(z) = \mathrm{v_{s,i}}/(1+z)$. As shown in the top panels of Fig. 5.1, this delays the point at which the gas will begin falling into the halo. To accommodate the cases with streaming, we replace $c_{\rm s}$ in Equ. (5.1) with $\mathrm{v_{eff}}$, and the resulting increase of $M_{\rm J}$ is shown in the bottom panels of Fig. 5.1.

For any given collapse redshift, a larger $M_{\rm vir}$ is therefore required to trigger the collapse of streaming gas compared to the non-streaming case. In Fig. 5.2, we estimate for different redshifts the mininum halo mass into which gas with various initial streaming velocities can collapse. We arrive at these estimates using the following simple prescription. We first determine for a range of redshifts the minihalo mass corresponding to a virial temperature of 1500 K, which serves as the minimum mass for collapse and cooling given no streaming. We fit a typical halo growth history using $M_{\rm vir}(z) = M_0 e^{\alpha z}$ (the green line shown in Fig. 5.1), with $M_0 = 2 \times 10^7$ M$_\odot$ and α ranging from -0.2 to -0.5. We vary α depending on the no-streaming case minihalo mass and the desired collapse redshift. For every given collapse redshift and streaming velocity, we first determine the redshift $z_{\rm eq}$ where $V_{\rm vir}(z) = \mathrm{v_{eff}(z)}$. We assume that $z_{\rm eq}$ is the point where the gas switches from having properties of the intergalactic medium (IGM) to properties determined by the halo. Thus, for

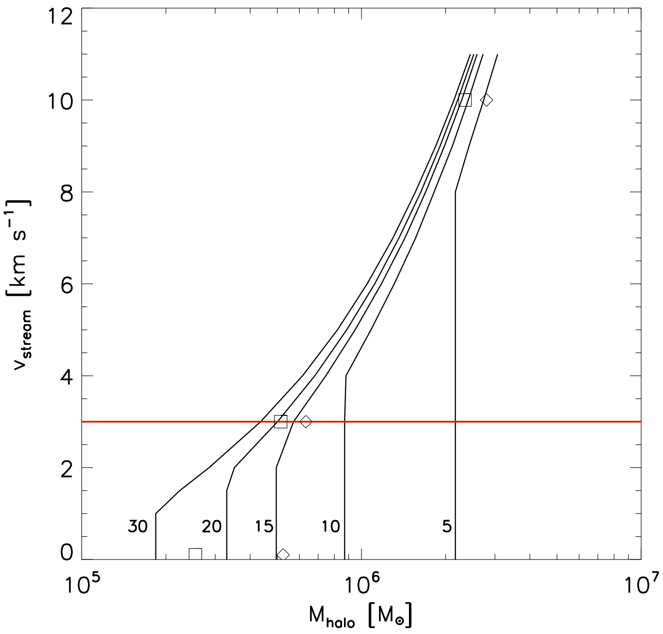

Figure 5.2: Effect of relative streaming on the minimum halo mass into which primordial gas can collapse. Each line represents the necessary halo masses for baryon collapse at a different redshift, marked in the plot. The diamonds represent the final halo masses found in 'standard collapse' simulations ($z_{\rm col} = 14$ for no streaming), and the squares represent masses from the 'early collapse simulations' ($z_{\rm col} = 24$ for no streaming). Note that the halo mass does not noticeably increase unless the initial streaming velocities are very high (greater than $\sim$ 3kms^{-1}). Also note that halos collapsing at high redshift are more affected by relative streaming, as the physical streaming velocities are higher at these early times.

$z > z_{\rm eq}$ the sound speed roughly follows that of the IGM, $c_{\rm s,IGM}$. Therefore, $z_{\rm eq}$ can be found by considering

$$V_{\rm vir}(z) = \sqrt{G\,M_{\rm vir}(z)/R_{\rm vir}(z)} = \sqrt{c_{\rm s,IGM}(z)^2 + {\rm v_s(z)}^2}\ , \tag{5.3}$$

where

$$R_{\rm vir}(z) \simeq 210 \left(\frac{M_{\rm vir}}{10^6 {\rm M_\odot}}\right)^{1/3} \left(\frac{1+z}{10}\right)^{-1} f(z)\ {\rm pc}, \tag{5.4}$$

and $f(z)$ is a factor of order unity with a mild dependence on redshift (Barkana and Loeb 2001). At $z = z_{\rm eq}$ the effective gas velocity is thus ${\rm v_{eq}} = V_{\rm vir}(z_{\rm eq})$. After this point the thermal energy of the halo gas dominates over the energy of streaming motion, and its sound speed can be described by the halo virial velocity thereafter.

Furthermore, $z_{\rm eq}$ marks the last time that the gas density within $R_{\rm vir}$ is still that of the IGM. The density of halo gas when it first couples to the DM is then

$$\rho_{\rm eq} = \rho_{\rm IGM}(z_{\rm eq}) \simeq 2 \times 10^{-29} \Omega_{\rm m} h^2 (1+z_{\rm eq})^3\ {\rm g\ cm^{-3}}. \tag{5.5}$$

Note that, because $z_{\rm eq}$ is lower for higher values of ${\rm v_{s,i}}$, $\rho_{\rm eq}$ correspondingly decreases.

Finally, as the gas infall into the halo continues for $z < z_{\rm eq}$, we estimate its average density to be

$$\rho(z) \simeq \rho_{\rm eq} \left(\frac{V_{\rm vir}(z)}{\rm v_{eq}}\right)^3\ . \tag{5.6}$$

The above equation describes how the gas density will adiabatically evolve with thermal energy as it collapses (e.g. Tegmark et al. 1997). Recall that ${\rm v_{eq}}$ is the effective sound speed when it first begins falling into the halo, and that adiabatic evolution implies $T \propto \rho^{\gamma-1} = \rho^{2/3}$ for an atomic gas with $\gamma = 5/3$.

Using $c_\mathrm{s} \propto T^{1/2}$ results in $\rho \propto c_\mathrm{s}^3$. Finally, we replace c_s with the virial velocity of the halo to arrive at the approximation in Equ. (5.6). The density will increase in this way until the gas virializes and reaches a maximum of $200\rho_\mathrm{IGM}(z)$. Inserting the applicable values for ρ and V_vir at the given collapse redshift, z_col, we arrive at $M_\mathrm{J}(z_\mathrm{col})$.

This model well reproduces the masses and collapse redshifts found in the simulations (symbols in Fig. 5.2). As the streaming velocities increase, the gas density during initial infall decreases, thereby lowering the typical gas density in the halo and raising the minimum mass that will satisfy $M_\mathrm{vir} > M_\mathrm{J}$. For the average 3 km s^{-1} streaming velocities, this minimum mass M_halo will approximately double for $z_\mathrm{col} = 30$, but will almost stay the same by $z_\mathrm{col} = 10$.

5.3.2 Thermal Evolution and Star Formation

Fig. 5.3 compares the thermal evolution for the 'standard' and 'early' collapse cases given no streaming with the corresponding rapid streaming cases ($v_\mathrm{s,i} = 10$ km s^{-1}). For the no streaming cases, the gas follows the canonical evolution of adiabatic heating as the IGM gas gradually becomes incorporated into the growing minihalo. This gas heats to the virial temperature (~ 1000 K) of the minihalo until the $\mathrm{H_2}$ fraction grows sufficiently high to allow the gas to cool to a minimum of $\simeq 200$ K. As the gas temperature drops, its density grows to approximately 10^4 cm^{-3} (see Bromm et al. 2002; Yoshida et al. 2006). At this density the gas has reached the 'loitering phase,' and this is the reservoir of gas from which Pop III stars will form.

For the $\mathrm{v_{s,i}} = 10$ km s^{-1} case, this evolution shows only minor differences from that described above. The initial heating of the low-density gas occurs more quickly than the purely adiabatic rate, and the streaming velocity

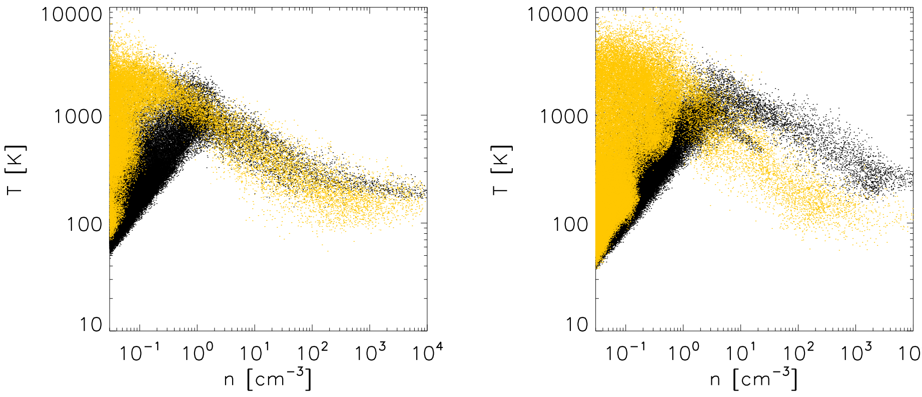

Figure 5.3: Evolution of temperature of the gas as density grows for both 'standard' and 'early' collapse cases. Black dots: No streaming case. Yellow dots: $\mathrm{v_{s,i}} = 10$ km s^{-1} case. *Left*: Standard case is shown at $z = 14.4$, while the $\mathrm{v_{s,i}}$ case is shown at $z = 6.6$. *Right*: Early collapse case is shown at $z = 23.6$ for no streaming, and $z = 12.4$ for $\mathrm{v_{s,i}} = 10$ km s^{-1}. There is almost no difference between the $\mathrm{v_{s,i}} = 3$ km s^{-1} (not shown) and no-streaming cases.

acts as a heating term for the low-density gas. However, once the gas gains sufficiently high temperature and H_2 fraction, the gas cools and condenses to approximately 200 K and 10^4 cm^{-3}, just as in the canonical case, though the minimum temperature is slightly lowered for the streaming cases. Subsequent star formation is therefore not suppressed, and should occur in the same way as it would in the no streaming case. Note also that Fig. 5.3 represents significantly higher streaming velocities than typically expected. For the more representative $\mathrm{v_{s,i}} = 3$ km s^{-1} cases, the thermal evolution shows almost no difference from those with no streaming. This further strengthens the argument that relative streaming between baryons and dark matter will do little to modify Pop III star formation.

Fig. 5.4 further elucidates the effect of relative streaming on gas collapse

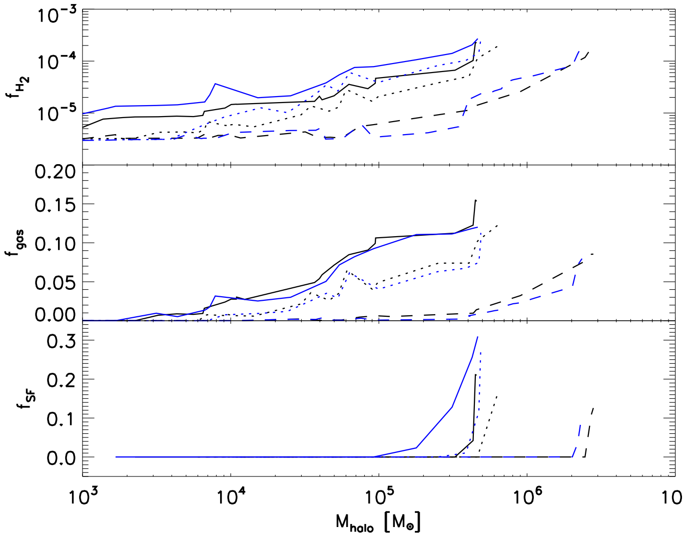

Figure 5.4: Evolution of gas properties with halo mass. Dashed lines: $v_{s,i}$ = 10 km s^{-1}, dotted lines: $v_{s,i}$ = 3 km s^{-1}, solid lines: no streaming. Black represents the 'standard collapse' set of simulations, while blue represents the 'early collapse' set. *Top panel*: Average H_2 fraction of the minihalo gas. *Middle panel*: Gas fraction f_{gas} of the halos. *Bottom panel*: Fraction of minihalo gas that is star-forming (i.e., $n > 1$ cm^{-3}). The reduced gas fraction and the delay of star formation for high streaming velocities are evident in the bottom panels. However, the H_2 fraction converges to greater than $\sim 10^{-4}$ in each case, allowing for the thermal evolution of the highest density gas to be relatively unchanged even for the highest streaming velocities.

and star formation. The delay of gas collapse until the minihalos have reached higher masses is evident in the bottom panel, which shows the fraction $f_{\rm SF}$ of the minihalo gas that is dense and star-forming, defined as the gas that exceeds densities of 1 $\rm cm^{-3}$. There is no star-forming gas in $< 10^6 M_\odot$ halos for the highest streaming velocities. The gas fraction $f_{\rm gas}$, calculated as the gas mass in the halo over its total mass, is reduced by up to a factor of ~ 1.2 for $\rm v_{s,i} = 3$ km $\rm s^{-1}$, and a factor of ~ 1.8 for $\rm v_{s,i} = 10$ km $\rm s^{-1}$, even after the gas has reached high densities. However, once gas collapse has occured, the average $\rm H_2$ fraction $f_{\rm H_2}$ is very similar in all cases, as is the subsequent thermal evolution (Fig. 5.3).

5.4 Summary and Discussion

Our series of simulations show that Pop III star formation will be essentially the same in cosmologies with relative streaming motions between gas and DM, even in regions with streaming velocities much higher than average ($\rm v_{s,i} \gtrsim 3$ km $\rm s^{-1}$). However, these regions of fast streaming will experience a modest delay in the collapse redshift at which Pop III stars will first form, while in regions of typical streaming the delay will be minimal ($\gtrsim 10^7$ years), in good agreement with Maio et al. (2010). In their work they also find similar reductions in halo gas fractions of up to a factor of 2, even given their larger box size and lower resolution. This is furthermore consistent with other recent work such as that of Tseliakhovich et al. (2010).

The effect on reionization should be similarly minimal. Though not yet known with certainty, recent work has suggested that the sources of reionization were dominated by early galaxies of virial temperatures above the hydrogen cooling threshold of 10^4K (corresponding to masses $\gtrsim 10^8 M_\odot$), with a much smaller contribution from $\lesssim 10^6 \mathrm{M}_\odot$ halos (e.g. Trac and Gnedin 2009; Trenti and Stiavelli 2009; Muñoz and Loeb 2011). The relative streaming motions will do little to alter the infall of gas into the larger potential wells of ionizing galaxies, and thus reionization should proceed virtually unaffected. The effect of streaming is mostly pronounced at the highest redshifts when the collapse fraction and the corresponding radiative effects of stars are exceedingly small.

In conclusion, we have directly simulated the delay in collapse, and the subsequent thermal evolution of the first baryonic structures under relative bulk velocities between gas and dark matter. Our results show that early star formation and subsequent evolution of reionization should quickly converge to the no-streaming case. Thus, results of previous and future cosmological studies concerning the formation of the first stars and galaxies will need only minimal modifications due to the relative streaming effect.

Chapter 6

Impact of Cosmic Rays on Population III Star Formation[1]

6.1 Overview

SN explosions are thought to be the site of cosmic ray (CR) production (e.g. Ginzburg and Syrovatskii 1969), and the CR background built up from the first SNe may affect the cooling and collapse of primordial gas clouds. Earlier studies (Shchekinov and Vasiliev 2004; Vasiliev and Shchekinov 2006) have shown how the presence of CRs at high redshifts could have lowered the minimum mass at which primordial gas could cool and collapse into virialized dark matter (DM) haloes (e.g. Haiman et al. 1996; Tegmark et al. 1997). This earlier study assumes the existence of ultra-heavy X particles that decay into ultra-high-energy CRs which interact with the cosmic microwave background (CMB), leading to the production of ionizing photons. In this paper, however, we instead examine CR effects which occur through direct collisional ionization of neutral hydrogen. The free electrons created from the ionization act as a catalyst for the formation of H_2 (McDowell 1961). Because molecular hydrogen emits photons through its rovibrational transitions, H_2 is able to cool primordial gas at temperatures below the threshold for atomic hydrogen cooling ($\lesssim 10^4$ K). Furthermore, CR ionization can indirectly lead to higher abundances of HD, which also acts as a cooling agent in low-temperature primordial gas (see Johnson and Bromm 2006). However, the presence of CRs can lead to ionization heating, as well. Whether this direct heating effect is strong enough to counter the additional cooling must be determined and will depend on the high-redshift CR energy density. Similar to our work, Rollinde et al. (2005, 2006) used models of early star formation to estimate the CR energy density in the early Universe, constraining it with the observed Li abundances in metal-poor Galactic halo stars.

---

[1] This chapter has been published as Stacy A. & Bromm V., 2007, MNRAS, 382, 229

In this paper, we will investigate the importance of the CR feedback on Pop III star formation by modeling its effect on the cooling of primordial gas in two cases: collapse within minihaloes, and shocks associated with the virialization of more massive DM haloes during the later stages of structure formation. The outline for this paper is as follows. In Chapter 6.2 we discuss CR acceleration and propagation in the high-redshift Universe and how these might differ from the present-day case. Chapter 6.3 describes the evolution of primordial gas in minihaloes and in virialization shocks when accounting for the effects of CRs. For the minihalo case we furthermore discuss how the fragmentation scale could change for a sufficiently high CR flux. We present our conclusions in Chapter 6.4.

6.2 Cosmic rays in the high-z Universe

6.2.1 Population III star formation

Though CR effects will be examined for a range of star formation rates, the typical Pop III star formation rate is taken to be that found in Bromm and Loeb (2006) at $z \simeq 15$, which is approximately $\Psi_* \simeq 2\times10^{-2}\ \mathrm{M}_\odot\ \mathrm{yr}^{-1}\ \mathrm{Mpc}^{-3}$ in a comoving volume. This rate was derived using the extended Press-Schechter formalism (Lacey and Cole 1993) to model the abundance and merger history of cold dark matter (CDM) haloes. In a neutral medium, before the redshift of reionization, Bromm and Loeb (2006) assume star formation occurs only in haloes that have become massive enough to enable atomic line cooling with virial termparatures above approximately 10^4 K. Recent work (see Greif and Bromm 2006) suggests that these more massive haloes were indeed the dominant site for star formation. Greif and Bromm (2006) argue that about 90 percent of the mass involved in metal-free star formation initially cooled through atomic line transitions.

At higher redshifts such as $z \sim 20$, however, the first stars are thought to have formed inside of $\sim 10^6$ $\mathrm{M}_\odot$ minihaloes through molecular cooling, and this mode of star formation is much more significant at this time. For the minihalo case at $z \sim 20$, Yoshida et al. (2003) estimate the rate of star formation through H_2 cooling to be $\Psi_* \sim 10^{-3}\,\mathrm{M}_\odot\,\mathrm{yr}^{-1}\,\mathrm{Mpc}^{-3}$. To account for such differences in these determinations of star formation rates, we examine a range of values spanning multiple orders of magnitude.

The Pop III initial mass function (IMF) currently remains highly uncertain, so for this study we do not perform our calculations using a specific IMF. For simplicity, we instead assume that those Pop III stars whose masses lie in the pair instability SN (PISN) range (140-260 $\mathrm{M}_\odot$) have an average mass of 200 $\mathrm{M}_\odot$ (e.g. Heger et al. 2003). A Pop III initial mass function (IMF) that extends over a large range of masses would imply that only a fraction of these stars were in the PISN range. Thus, here we assume that only slightly less than half of Pop III stars are in this mass range, leading to a somewhat more conservative value for the CR energy density. Our estimate generally corresponds to an IMF peaked around 100 $\mathrm{M}_\odot$. Due to their high mass, the first stars had very short lifetimes of about 3 Myr (e.g. Bond et al. 1984), and we therefore assume instantaneous recycling of the stellar material. As described below, this overall picture of Pop III star formation will be used to estimate the average CR energy density in the high-redshift Universe.

6.2.2 Cosmic ray production

For this paper CRs are assumed to have been generated in the PISNe that may have marked the death of Pop III stars. The CRs are accelerated in the SN shock wave through the first-order Fermi process by which high-energy particles gain a small percentage increase in energy each time they diffuse back and forth across a shock wave. This yields a differential energy spectrum in terms of CR number density per energy (e.g. Longair 1994):

$$\frac{dn_{\mathrm{CR}}}{d\epsilon} = \frac{n_{\mathrm{norm}}}{\epsilon_{\mathrm{min}}} \left(\frac{\epsilon}{\epsilon_{\mathrm{min}}} \right)^{x} \ , \tag{6.1}$$

where we will use $x = -2$ for definiteness, a typical value given by Fermi acceleration theory (e.g. Bell 1978a). Here, ϵ is the CR kinetic energy, ϵ_{min} is the minimum kinetic energy, and n_{CR} is the CR number density. Note that our results are somewhat sensitive to the choice of x. Choosing values for x that are closer to what is observed in the Milky Way, such as $x = -2.5$ or $x = -3$, or using a CR spectrum similar to that given in Rollinde et al. (2005, 2006) will increase CR heating and ionization, if the overall CR energy density is held constant. For these steeper power laws a higher fraction of the total CR energy resides in the lower-energy CRs, which are the ones that contribute the most to these CR effects, as discussed in Chapters 6.3.1 and 6.3.4 and in the discussion for Fig. 6.3. . Such steeper spectral slopes can in fact yield CR heating and ionization rates up to an order of magnitude higher than for

$x = -2$. Using $x = -2$ is therefore a more conservative choice that does not assume any modifications to standard Fermi acceleration theory.

By equating the total CR energy density $U_{\rm CR}$ with the integral of the differential CR spectrum over all energies, the normalizing density factor $n_{\rm norm}$ is estimated to be

$$n_{\rm norm} = \frac{U_{\rm CR}}{\epsilon_{\rm min} \ln\left(\frac{\epsilon_{\rm max}}{\epsilon_{\rm min}}\right)} \approx \frac{1}{10}\frac{U_{\rm CR}}{\epsilon_{\rm min}} \ , \tag{6.2}$$

where we get approximately 1/10 for the coefficient choosing $\epsilon_{\rm max} = 10^{15}$ eV and $\epsilon_{\rm min} = 10^{6}$ eV. The differential energy spectrum is therefore

$$\frac{dn_{\rm CR}}{d\epsilon} = \frac{U_{\rm CR}}{\epsilon^2_{\rm min} \ln\left(\frac{\epsilon_{\rm max}}{\epsilon_{\rm min}}\right)} \left(\frac{\epsilon}{\epsilon_{\rm min}}\right)^{-2} \ , \tag{6.3}$$

with

$$U_{\rm CR}(z) \approx p_{\rm CR} E_{\rm SN} f_{\rm PISN} \Psi_*(z) t_H(z)(1+z)^3 \ . \tag{6.4}$$

This can also be written as

$$\begin{aligned} U_{\rm CR}(z) \approx 2\times10^{-15}\,{\rm erg\,cm^{-3}} \left(\frac{p_{\rm CR}}{0.1}\right)\left(\frac{E_{\rm SN}}{10^{52}\,{\rm erg}}\right)\left(\frac{1+z}{21}\right)^{\frac{3}{2}} \\ \times\left(\frac{f_{\rm PISN}}{2\times10^{-3}\,{\rm M_\odot^{-1}}}\right)\left(\frac{\Psi_*}{2\times10^{-2}\,{\rm M_\odot\,yr^{-1}\,Mpc^{-3}}}\right), \end{aligned} \tag{6.5}$$

where $p_{\rm CR}$ is the fraction of SN explosion energy, $E_{\rm SN}$, that goes into CR energy, and $f_{\rm PISN}$ is the number of PISNe that occur for every solar mass unit of star-forming material. Here we take the above star-formation rate to be constant over a Hubble time t_H, where

$$t_H(z) \simeq 2 \times 10^8\,\mathrm{yr} \left(\frac{1+z}{21}\right)^{-3/2} \quad , \tag{6.6}$$

evaluated at the relevant redshift. We assume that each star quickly dies as a PISN with $E_{\rm SN} = 10^{52}$ erg, appropriate for a $200\,\mathrm{M}_\odot$ star (Heger and Woosley 2002), ten percent of which is transformed into CR energy (e.g. Ruderman 1974). The value of ten percent is derived from Milky Way (MW) energetics, and here we have simply extrapolated this to PISNe. Very little is known about what value of $p_{\rm CR}$ applies to PISNe specifically, so assuming their shock structure to be similar to local SNe appears to be a reasonable first guess. We choose $1/500\,\mathrm{M}_\odot$ for $f_{\rm PISN}$, so that there is one PISN for every $500\,\mathrm{M}_\odot$ of star-forming material. This implies that somewhat less than half of the star forming mass falls within the PISN range.

Compared to PISNe, the usual core-collapse SNe (CCSNe) thought to accelerate CRs in the Milky Way have an explosion energy that is lower by about an order of magnitude. However, the masses of their progenitor stars are also much lower, ranging from $\sim 10-40\,\mathrm{M}_\odot$. Thus, if we have an IMF extending to this lower mass range, there will be approximately an order of magnitude more SNe per unit mass of star-forming material. However, because $E_{\rm SN}$ for low-mass ($\sim 10\,\mathrm{M}_\odot$) CCSNe progenitors will be lower by a similar amount, these two effects may cancel out and result in a total $U_{\rm CR}$ that is comparable to the PISN case. Furthermore, the difference in shock velocities, $u_{\rm sh}$, between a PISN and a CCSN should not be more than a factor of a few. Though CCSNe have a lower explosion energy, this energy is used to accelerate roughly ten times less ejected mass, $M_{\rm ej}$, than in a PISN. Simple energy conservation, $E_{\rm SN} \simeq \frac{1}{2}M_{\rm ej}u_{\rm sh}^2$, then indicates that the shock velocities of these different SNe will be similar. This also leads to similar estimates for $\epsilon_{\rm min}$ for both cases since the minimum CR energy is expected to depend on shock velocity. For a given star formation rate the results of our study would therefore change little if the source of CRs were CCSNe instead of PISNe.

It should be pointed out that the explosion mechanism of the highest-mass CCSNe progenitors, $\sim 40\,{\rm M}_\odot$, is still somewhat uncertain and may be associated with very high explosion energies comparable to that of PISNe, though if most of the CCSNe derive from lower-mass progenitors they should still have lower explosion energies as argued above. Furthermore, we emphasize that the choice of PISNe versus CCSNe is not crucial for our study as long as there exists some source of sufficient CR production. These sources do not necessarily have to be only PISNe. Constraints on the number of PISNe in the early Universe, such as provided by the problem of overproduction of metals in the IGM by PISNe (e.g. Venkatesan and Truran 2003; Tumlinson et al. 2004; Daigne et al. 2006), will therefore not affect the relevance of this study.

Finally, it is worth noting that the CR energy densities used in this paper are well-within upper limits placed by previous studies. For instance, one of the constraints that can be used to place an upper limit on $U_{\rm CR}$ is the ^{6}Li plateau observed in metal-poor Galactic halo stars. While a number ratio of ^{6} Li/H$\simeq 10^{-11}$ is observed (Asplund et al. 2006), the much smaller ratio ^{6} Li/H$\simeq 10^{-14}$ is predicted by big bang nucleosynthesis (BBN). In Rollinde et al. (2005, 2006), the overabundance of ^{6}Li compared to predictions from BBN is assumed to have come from CRs generated by the first stars. In Rollinde et al. (2005) this assumption was used to derive an upper limit on the high-z CR energy density. Assuming a model with a single burst of Pop III star formation, they found CR energy densities at the time of these bursts to range from approximately 10^{-10} to 10^{-12} erg cm^{-3} for burst times ranging from $z = 100$ to $z = 10$. Such limits are roughly three orders of magnitude larger than the $U_{\rm CR}$ values used in our investigation, so that we do not violate any known constraints on CR production in the early Universe.

6.2.3 High-redshift GZK cutoff

The Greisen-Zatsepin-Kuzmin (GZK) cutoff is an upper limit to the energy of a CR if it is extragalactic in origin and thus has traveled through the sea of CMB photons (Greisen 1966; Zatsepin and Kuz'min 1966). This limit exists because of interactions between CRs and CMB photons which lead to photo-pion and pair production, reducing the energy of the CR for each interaction. The reactions for pair production and photo-pion production, respectively, are (e.g. Berezinskii and Grigor'eva 1988)

$$p^+ + \gamma \rightarrow p^+ + e^+ + e^- \ , \tag{6.7}$$

$$p^+ + \gamma \rightarrow \pi^+ + n \ , \tag{6.8}$$

$$p^+ + \gamma \rightarrow \pi^0 + p^+ \ . \tag{6.9}$$

Photo-pion production is the most important interaction for CR protons (De Marco 2005). However, this reaction can only take place if the energy of a CMB photon is above the energy threshold of $\epsilon_t = 140$ MeV, but this is possible in the rest frame of CRs with sufficiently large Lorentz factors (e.g. Longair 1994). The reaction will continue until the CR energy falls below the corresponding threshold, which is $\epsilon_{\rm GZK} = 5 \times 10^{19}$ eV in today's Universe. This cutoff has recently been observed by the HiRes experiment (Abbasi et al. 2008).

In the high-redshift Universe, however, the GZK cutoff will be somewhat lower, as can be seen as follows: While in today's Universe the average energy of a CMB photon is $\epsilon_{\rm CMB} = 2.7 k_{\rm B} T_{\rm CMB} = 6 \times 10^{-4}$ eV, at higher redshifts this energy will be larger by a factor of $(1+z)$. In the CR rest frame, the CMB photon energy is

$$\epsilon'_{\rm CMB} \approx \gamma\, 6 \times 10^{-4}\,{\rm eV}\,(1+z)\ , \tag{6.10}$$

where γ is the Lorentz factor of a CR proton. Equating $\epsilon'_{\rm CMB}$ with ϵ_t, we find

$$\gamma \approx \frac{2 \times 10^{11}}{(1+z)}\ . \tag{6.11}$$

We can now calculate the CR energy for which the threshold for photo-pion production is reached:

$$\epsilon_{\rm GZK}(z) = \gamma m_{\rm H} c^2 \approx \frac{3 \times 10^{20}\,{\rm eV}}{(1+z)}, \tag{6.12}$$

where $m_{\rm H}$ is the mass of a proton. A more precise calculation, carrying out an integration over the entire Planck spectrum and over all angles, yields

$$\epsilon_{\rm GZK}(z) = \frac{5 \times 10^{19}\,{\rm eV}}{1+z} \approx 2 \times 10^{18}\,{\rm eV} \left(\frac{1+z}{21}\right)^{-1}\ . \tag{6.13}$$

Thus, at redshifts of 10 or 20, the GZK cutoff is around an order of magnitude smaller than in today's Universe, giving a robust upper limit to the CR energy.

The GZK cutoff applies only to those CRs that travel large distances through the CMB. A CR can undergo a maximum of approximately 10 interactions with CMB photons before falling below the GZK limit (e.g. Longair 1994). Given an interaction cross section of $\sigma = 2.5 \times 10^{-28}$ cm^2 for photo-pion production and a CMB density of $n_\gamma = 5 \times 10^2\ \mathrm{cm}^{-3}\,(1+z)^3$, the interaction mean-free-path is

$$\lambda = (\sigma n_\gamma)^{-1} \simeq \frac{10^{25}\,\mathrm{cm}}{(1+z)^3}. \tag{6.14}$$

The maximum distance from which ultra-high energy CRs (UHECRs) with $\epsilon_{\mathrm{CR}} \geq 5 \times 10^{19}$ eV$/(1+z)$ could have originated is therefore

$$d_{\max} \simeq 10\lambda \simeq \frac{10^{26}\,\mathrm{cm}}{(1+z)^3} \simeq 3\,\mathrm{kpc}\left(\frac{1+z}{21}\right)^{-3}. \tag{6.15}$$

Thus, at $z = 20$ a UHECR impinging upon a primordial gas cloud must have been accelerated in a source no more than a proper distance of $\sim$ 3 kpc away. The origin of UHECRs remains unknown even in today's Universe, though possible sources range from pulsar winds to active galactic nuclei (AGN) and gamma-ray bursts (GRBs) (e.g. de Gouveia Dal Pino and Lazarian 2001; Waxman 2001; Torres et al. 2002). Though structures at $z = 15$ and $z = 20$ are not yet massive enough to form AGN, pulsars and GRBs may be plausible UHECR sources at these redshifts (e.g. Bromm and Loeb 2006).

6.2.4 Magnetic fields

Magnetic fields are an important component of CR studies due to their effects on both CR acceleration and propagation through the Universe. For instance, the maximum energy a CR can reach with the Fermi acceleration process has a linear dependence on the ambient magnetic field strength if the growth rate of the CR's energy is limited by its Larmor radius (Lagage and Cesarsky 1983). Under this assumption strengths of $\sim 10^{-10}$ G are necessary to accelerate a CR to 10^9 eV (Zweibel 2003).

The strength, generation, and dispersal of magnetic fields at high redshifts, however, is still highly uncertain. One of the most widely held views is that magnetic seed fields were created soon after the Big Bang and were later amplified in higher-density structures through dynamo mechanisms. Seed fields are thought to form through various processes including galaxy-scale outflows in the early Universe and the Biermann battery mechanism in regions such as shock waves and ionization fronts (e.g. Kronberg et al. 1999; Gnedin et al. 2000). For one illustrative example, Ichiki et al. 2006 propose a mechanism by which seed fields are created before recombination through second-order cosmological perturbations. They calculate the seed field at the redshift of recombination, $z_{\rm rec} \approx 1000$, to be

$$B_0(z_{\rm rec}) \simeq 10^{-14}\,{\rm G}\left(\frac{\lambda}{10\,{\rm kpc}}\right)^{-2}\ , \tag{6.16}$$

where λ is the comoving size of the structure in question for scales less than about 10 Mpc. If we take into account magnetic flux freezing as structures become dense and the Universe expands, we get a seed field at virialization of

$$B_0(z_{\rm vir}) \simeq 10^{-20}\,{\rm G}\left(\frac{\lambda}{10\,{\rm kpc}}\right)^{-2}\left(\frac{\rho_{\rm s}}{\rho_o}\right)^{2/3}_{z_{\rm vir}}(1+z_{\rm vir})^2\ , \tag{6.17}$$

where $(\rho_{\rm s}/\rho_o)_{z_{\rm vir}} \sim 200$ is the overdensity of the structure in question compared to the average density of the Universe at $z_{\rm vir}$, the redshift at which the structure first virializes. For a minihalo with a comoving size of around 10 kpc and virialization redshift $z_{\rm vir} = 20$, this gives $B_0 \sim 10^{-16}\,$G. When dynamo effects are taken into account, the magnetic field is further amplified and can grow exponentially on a timescale determined by differential rotation and turbulence within the structure (e.g. Field 1995; Widrow 2002). Magnetic field amplification within the accelerating region of a SN remnant itself may also increase its strength by up to two orders of magnitude (e.g. van der Laan 1962; Bell and Lucek 2001). This magnetic field growth can occur through processes such as flux freezing in the compressed regions of the SN remnant and non-linear amplification through growth and advection of Alfvén waves generated by the pressure of CRs themselves. Within structures that have already experienced star formation, magnetic fields can further be built up through field ejection in stellar winds, SN blastwaves, and protostellar jets (e.g. Machida et al. 2006).

For these fields to be spread into the general IGM, however, there must be a sufficient degree of turbulent mixing and diffusion in intergalactic regions. While such processses are effective within structures, it is less obvious that they are also effective in the IGM at eras soon after star formation has begun (Rees 2006). Thus, the build-up and amplification of magnetic fields in pristine intergalactic matter and in the filaments at high redshifts is very uncertain. We can estimate the critical magnetic field at $z \sim 20$ that would influence CR propagation by equating the relevant physical distance scale with the Larmor radius $r_{\rm L}$ and finding the corresponding magnetic field strength, where for a proton $r_{\rm L} = \gamma m_{\rm H} \beta c^2/(eB)$, and e is the proton charge. Considering the maximum scale a CR could travel at $z \sim 20$, we write $r_{\rm L} = \beta c/H(z=20)$, where βc is the CR velocity and $H(z)$ the Hubble constant at redshift z. For $\epsilon_{\rm CR} = 10^6$ eV, we find $r_{\rm L} \simeq 90$ Mpc, corresponding to a magnetic field strength of 10^{-20} G, several orders of magnitude higher than what Ichiki et al. (2006) estimated for this length scale. When looking at CR propagation between minihaloes, the physical distance in question is much smaller, $r_{\mathrm{L}} \simeq 1$ kpc. This corresponds to a magnetic field strength of $5{\times}10^{-17}$ G, around an order of magnitude stronger than the magnetic field predicted by Ichiki et al. (2006). These seed fields from recombination are thus too small to affect CR propagation.

It is therefore not implausible that at high redshift there existed sufficient magnetic fields in the DM haloes to accelerate CRs to relativistic energies while their propagation in the IGM and filaments was very close to rectilinear due to the weak magnetic fields in these regions. This unconfined propagation in the IGM would allow a universal isotropic CR background to build up, and this is what we assume in our analysis.

6.3 Evolution of Primordial Clouds

6.3.1 Idealized models

We examine the evolution of primordial gas by adapting the one-zone models used in Johnson and Bromm (2006) (see also Mackey et al. 2003). In the $z \sim 20$ collapsing minihalo case, typical halo masses are $\sim 10^6\ \mathrm{M}_\odot$. The minihaloes form during hierarchical mergers at velocities too low to cause any shock or ionization in the minihalo, so the electron-catalysed molecule formation and cooling is insufficient to allow stars less than around $100\,\mathrm{M}_\odot$ to form (e.g. Bromm et al. 1999, 2002; Abel et al. 2002). CR ionization and heating, however, can potentially alter the thermal and chemical evolution of primordial gas.

In our model, the minihalo has an initial ionization fraction of $x_e = 10^{-4}$

and undergoes free-fall collapse. Its density therefore evolves according to $dn/dt = n/t_{\rm ff}$, with the free-fall time being

$$t_{\rm ff} = \left(\frac{3\pi}{32G\rho}\right)^{1/2} , \tag{6.18}$$

where $\rho = \mu m_{\rm H} n \approx m_{\rm H} n$ and $\mu = 1.2$ is the mean molecular weight for neutral primordial gas. The initial density was taken to be the density of baryons in DM haloes at the point of virialization (e.g. Clarke and Bromm 2003)

$$n_0 \simeq 0.3\,{\rm cm}^{-3}\left(\frac{1+z}{20}\right)^3 . \tag{6.19}$$

The initial temperature of the gas was taken to be 200 K, and the initial abundances were the primordial ones (e.g. Bromm et al. 2002).

As our second case, we consider strong virialization shocks that arise in later stages of structure formation during the assembly of the first dwarf galaxies. The corresponding DM haloes virialize at $z \sim 10 - 15$, and have masses ranging from $\sim 10^8$ to $\sim 10^{10}$ $M_\odot$. The conditions during the assembly of the first dwarf galaxies show some key differences from the former case. The virial velocities of these DM haloes are much greater, implying merger velocites that are now high enough to create a shock that can partially ionize the primordial gas (Johnson and Bromm 2006 and references therein). The post-shock evolution is taken to be roughly isobaric (e.g. Shapiro and Kang 1987; Yamada and Nishi 1998). We use an initial post-shock temperature of

$$T_{\rm ps} = \frac{m_{\rm H} u_{\rm sh}^2}{3k_{\rm B}} . \tag{6.20}$$

For an initial density of $n_{\rm ps}$, again found from Equ. (6.19), the temperature and density will follow the relation $T_{\rm ps} n_{\rm ps} \simeq Tn$.

6.3.2 Thermal and chemical evolution

In calculating the evolution of the primordial clouds, we solve the comprehensive chemical reaction network for all the species included in Johnson and Bromm (2006), and consider cooling due to H, H_2, and HD. The temperature of the CMB sets the lower limit to which the gas can cool radiatively (e.g. Larson 1998). Assuming that CRs with the above energy spectrum impinge upon the primordial gas cloud, we add the respective heating and ionization rates. Once a low-energy CR enters the high-density region of the cloud, each time it ionizes an H atom, an electron with average energy $< E >= 35$ eV is released (Spitzer and Tomasko 1968). Including the ionization energy of 13.6 eV implies that a CR proton loses approximately 50 eV of kinetic energy upon each scattering. This places a limit on the number of scatterings a CR can undergo in a cloud as well as a limit on the distance into the cloud that it can reach before it loses all its energy to ionization. This distance can be described by a penetration depth

$$D_p(\epsilon) \approx \frac{\beta c \epsilon}{-\left(\frac{d\epsilon}{dt}\right)_{\text{ion}}} \ , \tag{6.21}$$

where (Schlickeiser 2002)

$$-\left(\frac{d\epsilon}{dt}\right)_{\text{ion}} = 1.82 \times 10^{-7} \text{eV}\,\text{s}^{-1} n_{\text{H}^0} f(\epsilon), \tag{6.22}$$

$$f(\epsilon) = (1 + 0.0185 \ln\beta) \frac{2\beta^2}{\beta_0^3 + 2\beta^3}, \tag{6.23}$$

and

$$\beta = \left[1 - \left(\frac{\epsilon}{m_{\rm H}c^2} + 1\right)^{-2}\right]^{1/2} . \qquad (6.24)$$

Here, $m_{\rm H}$ is the mass of a proton, $\beta = v/c$, and $({\rm d}\epsilon/{\rm dt})_{\rm ion}$ is the rate of CR energy loss due to ionization. The cutoff value of $\beta_0 \simeq 0.01$ is appropriate for CRs traveling through a medium of atomic hydrogen, since $\beta_0 c = 0.01c$ is the approximate orbital velocity of electrons in the ground state of atomic hydrogen. When the velocity of CRs falls below $\beta_0 c$, the interaction between the CRs and electrons will sharply decrease, as will the ionization rate (Schlickeiser 2002), but for our study all CRs are assumed to be above this critical velocity. Thus, for a given distance D into a cloud, a CR has an effective optical depth of D/D_p. Fig. 6.1 shows the dependence of D_p on CR energy for a neutral hydrogen density of $n_{\rm H^0} = 1$ cm^{-3}, which is typical for densities in the minihalo case. Densities will of course greatly increase towards the end of the free-fall evolution, but the size of the collapsing gas cloud, and thus the distance CRs must travel, will decrease. Although the overall attenuation would be slightly greater if the time-dependent density evolution were accounted for instead of using a constant attenuation value, when comparing these two cases the difference is not large enough to yield a significant variation in the minihalo's temperature evolution. For simplicity, only the typical density was therefore used in calculating the attenuation.

As can be seen in Fig. 6.1, the lowest-energy CRs do not get attenuated until they travel a distance of about a few hundred pc, so in gas clouds of this size or smaller the CR flux will not be significantly attenuated. This also shows that the low-energy CRs are the ones that will have the greatest ionization and heating contribution to the cloud, as they more readily release

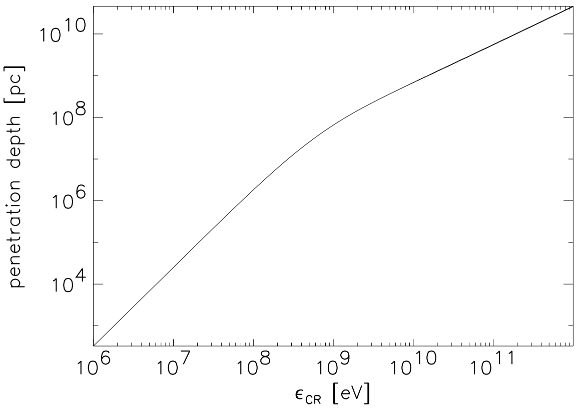

Figure 6.1: Penetration depth as a function of CR energy. We here assume a neutral hydrogen number density of $n_{\rm H} = 1$ cm^{-3}. Only clouds with radii larger than about a few hundred pc will entirely attenuate the lowest-energy CRs through ionization losses. This also implies that low-energy CRs are necessary to contribute significant ionization and heating, as those are the ones that will release most of their energy into gas clouds of size $\sim 0.1-1$ kpc.

their energy into the gas. In contrast, higher energy CRs will quickly travel through a minihalo without transferring much of their energy into the gas. They instead lose energy more slowly over much longer distances. Accounting for the attenuation yields CR ionization and heating rates of

$$\Gamma_{\rm CR}(D) = \frac{E_{\rm heat}}{50\,{\rm eV}} \int_{\epsilon_{\rm min}}^{\epsilon_{\rm max}} \left(\frac{d\epsilon}{dt}\right)_{\rm ion} \frac{dn_{\rm CR}}{d\epsilon} e^{-D/D_p} {\rm d}\epsilon \tag{6.25}$$

and

$$\zeta_{\rm CR}(D) = \frac{\Gamma_{\rm CR}}{n_{\rm H^0} E_{\rm heat}} \ . \tag{6.26}$$

These rates can also be written as

$$\Gamma_{\rm CR}(D) = 5 \times 10^{-29}\,{\rm erg\,cm^{-3}\,s^{-1}} \left(\frac{U_{\rm CR}}{2 \times 10^{-15}\,{\rm erg\,cm^{-3}}} \right) \times \left(\frac{E_{\rm heat}}{6\,{\rm eV}} \right) \left(\frac{n_{\rm H^0}}{1\,{\rm cm^3}} \right) \left(\frac{\epsilon_{\rm min}}{10^6\,{\rm eV}} \right)^{-1} I(\epsilon) \tag{6.27}$$

and

$$\zeta_{\rm CR}(D) = 5 \times 10^{-18}\,{\rm s^{-1}} \left(\frac{U_{\rm CR}}{2 \times 10^{-15}\,{\rm erg\,cm^{-3}}} \right) \times \left(\frac{\epsilon_{\rm min}}{10^6\,{\rm eV}} \right)^{-1} I(\epsilon), \tag{6.28}$$

where

$$I(\epsilon) = \frac{\int_{\epsilon_{\rm min}}^{\epsilon_{\rm max}} f(\epsilon) \left(\frac{\epsilon}{\epsilon_{\rm min}} \right)^{x} e^{-D/D_p} {\rm d}\epsilon}{\int_{\epsilon_{\rm min}}^{\epsilon_{\rm max}} \left(\frac{\epsilon}{\epsilon_{\rm min}} \right)^{x+1} {\rm d}\epsilon} \,. \tag{6.29}$$

The factor $E_{\rm heat}$ is equal to 6 eV for the minihalo case because, though CRs lose about 50 eV of energy after each ionization, only about 6 eV of that energy goes toward heating in a neutral medium (see Spitzer and Scott 1969; Shull and van Steenberg 1985). The value of $E_{\rm heat}$ increases for media with larger ionization fractions due to an increase in Coulomb interactions between the newly freed electrons and the medium, and for the ionization fractions typical of the virialization shock case, one has $E_{\rm heat} \simeq 26$ eV.

The minimum kinetic energy, $\epsilon_{\rm min}$, with which the CRs impinge upon the gas clouds can be roughly estimated by assuming that during Fermi acceleration a particle will acquire the velocity of the shock wave itself after crossing it a single time (see Bell 1978b). This gives a minimum energy

$\epsilon_{\mathrm{min}} \sim \frac{1}{2} m_{\mathrm{H}} u_{\mathrm{sh}}^2 \approx 10^6$ eV, where $u_{\mathrm{sh}} \approx 10^4\,\mathrm{km\,s^{-1}}$ is the PISN shock velocity in its initial blast-wave stage. The effects of changing ϵ_{min} will be discussed later. Due to the power-law distribution of CR energies, the value of the maximum CR kinetic energy, ϵ_{max}, has less importance since the number densities and ionization rates of highly relativistic CRs are much smaller than those of nonrelativistic and marginally relativistic ones. We therefore choose a default value of $\epsilon_{\mathrm{max}} = 10^{15}$ eV, a typical maximum value determined from Fermi acceleration theory (e.g. Blandford and Eichler 1987).

Fig. 6.2 shows the gas cloud evolution for the minihalo collapse case for models with and without CR effects at $z = 20$. The heating rate is evaluated at $D = 100$ pc, the characteristic distance to the cloud center, as this is where star formation is expected to take place. Various combinations of $\Psi_* = 2 \times 10^{-3}$ or $2 \times 10^{-2}\,\mathrm{M_\odot\,yr^{-1}\,Mpc^{-3}}$ and $\epsilon_{\mathrm{min}} = 10^6$, 10^7, or 10^8 eV are considered. The resulting CR ionization leads to an increase in the electron abundance in the cloud. These electrons act as the only catalyst for H_2 formation since at this early time in the Universe there are no dust grains on which H_2 could form. The increased electron abundance thus allows for more H_2 to form. H_2, in turn, can also be used in the main reaction that creates HD (see, e.g. Johnson and Bromm 2006). With the increase in molecular abundance due to CR ionization, the cloud is able to cool to temperatures much closer to the CMB floor if $\Psi_* = 2 \times 10^{-2}\,\mathrm{M_\odot\,yr^{-1}\,Mpc^{-3}}$ and $\epsilon_{\mathrm{min}} = 10^6$ or 10^7 eV. This indirect cooling effect is stronger than the direct CR heating effect even for star formation rates up to 100 to 1000 times higher than those shown here. Futhermore, for Ψ_* as low as $2 \times 10^{-4}\,\mathrm{M_\odot\,yr^{-1}\,Mpc^{-3}}$, the CR effects are negligible for all ϵ_{min} values explored in this study.

To further illustrate how the level of CR-induced cooling can vary with

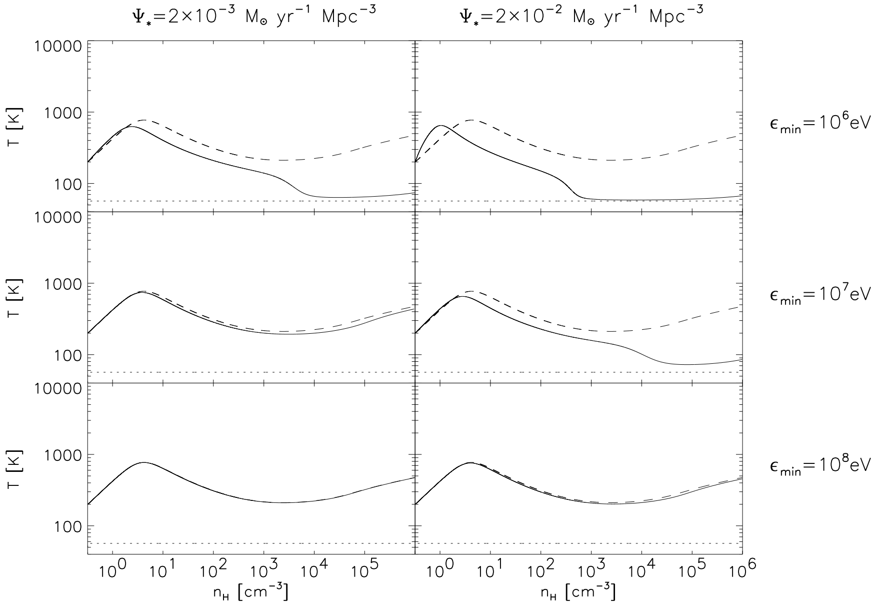

Figure 6.2: Thermal evolution of primordial gas clouds undergoing free-fall collapse inside minihaloes at $z = 20$ for various combinations of Pop III star formation rate and $\epsilon_{\rm min}$. The solid lines show the evolution when the effect of CRs is included, while the dashed lines depict the standard evolution where only cooling due to H_2 and HD are considered. The dotted line represents the CMB temperature floor at $z = 20$. Notice that the presence of CRs can significantly alter the evolution, in particular lowering the temperature, compared to the canonical picture of how primordial gas behaves in minihaloes. However, this effect crucially relies on the presence of CRs with sufficiently low kinetic energy.

CR parameter values, Fig. 6.3 shows the minimum temperature $T_{\rm min}$ reached by the minihalo gas versus $U_{\rm CR}$ and spectral index x given a constant $\epsilon_{\rm min} = 10^6$ eV. It is evident that the cloud can cool to temperatures near the CMB floor for $U_{\rm CR}$ values ranging over nearly four orders of magnitude. At extremely high values of $U_{\rm CR}$ that are near the upper limit set by the ^{6}Li measurements, CR-induced heating begins to overcome cooling effects, and the minihalo gas can no longer reach temperatures near the CMB floor. Also, for shallower spectral indices, much less of the CR energy density is distributed at low energies. For these shallower power laws, CRs thus cause only negligible change in the minimum gas temperature since they yield almost no heating or cooling of the gas.

Examination of Fig. 6.2 and the corresponding ionization rates for each case show that CRs can facilitate cooling in the minihalo to nearly the CMB floor if the ionization rate is greater than approximately 10^{-19} s^{-1}. Any rate below this yields negligible cooling. Considering the dependence of the ionization rate on $\epsilon_{\rm min}$ and $U_{\rm CR}$ in Equ. (6.28) and Equ. (6.29) for the minihalo case, we can write

$$\zeta_{\rm CR} \approx 10^{-19}\,{\rm s}^{-1} \left(\frac{U_{\rm CR}}{2\times 10^{-15}\,{\rm erg\,cm^{-3}}}\right) \left(\frac{\epsilon_{\rm min}}{10^7\,{\rm eV}}\right)^{-1.3} . \qquad (6.30)$$

Recalling the dependence of $U_{\rm CR}$ on redshift and Ψ_* from Equ. (6.4), we find that there will be sufficient ionization, so that the CR-induced cooling will be significant in the minihalo, if the following condition is met:

$$\left(\frac{\Psi_*}{10^{-2}\,{\rm M_\odot\,yr^{-1}\,Mpc^{-3}}}\right) \left(\frac{1+z}{21}\right)^{\frac{3}{2}} \left(\frac{\epsilon_{\rm min}}{10^7\,{\rm eV}}\right)^{-1.3} \gtrsim 1 \ . \qquad (6.31)$$

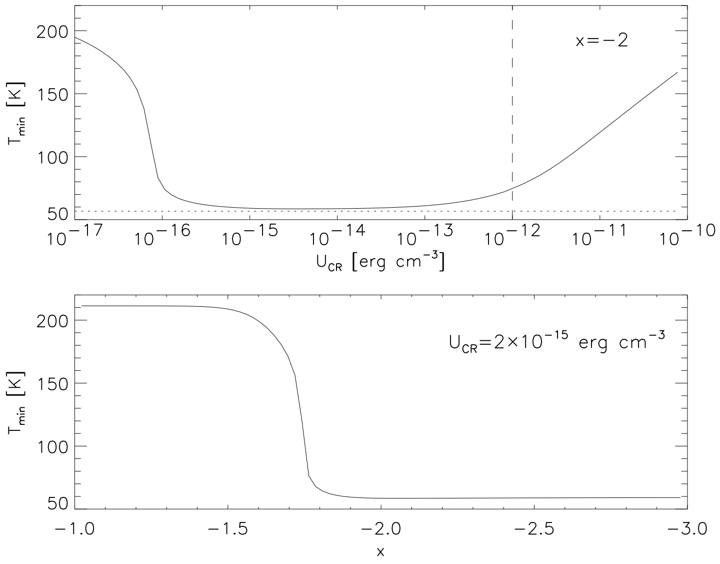

Figure 6.3: Minimum temperature reached by the minihalo gas versus $U_{\rm CR}$ *(top panel)* and spectral slope x *(bottom panel)*. The dotted lines denote the CMB temperature, and the dashed line in the upper panel is the upper bound on $U_{\rm CR}$ based on constraints from the ^{6}Li measurements. Here $\epsilon_{\rm min}$ is kept constant at 10^6 eV. Note that the cloud cools nearly to the CMB floor for $U_{\rm CR}$ values ranging over almost four orders of magnitude. CR-induced heating starts to overcome cooling effects and the minimum temperature begins to rise only once $U_{\rm CR}$ values are near the ^{6}Li constraint. For shallower spectral slopes, and thus smaller numbers of low-energy CRs for a given $U_{\rm CR}$, CRs cause little cooling or heating and do not change the minimum temperature of the minihalo gas.

Here, we assume that all other variables that determine $U_{\rm CR}$ have the same values used thus far in this study.

In Fig. 6.4, we show the evolution of a gas cloud in the virialization shock case at $z = 15$. The heating rate is now evaluated at $D = 500$ pc, a typical distance from the outer edge of the halo to its densest region. We again examine the evolution for various combinations of Ψ_* and $\epsilon_{\rm min}$. Note that here we consider star formation rates that are an order of magnitude larger than in the minihalo case. Such increased rates reflect the later formation times of the first dwarf galaxies, so that structure formation has already progressed further. In most of these cases the presence of CRs has a negligible effect. This is in part due to the enhanced CR attenuation resulting from the larger cloud sizes. Furthermore, unlike in the free-fall minihalo evolution, in the case of strong shocks the gas never reaches very high densities of neutral hydrogen. Densities for the shocked case are instead typically around $\lesssim 0.2$ cm^{-3} early in the halo's evolution, and 100 cm^{-3} after the gas temperature has reached the CMB floor. The average heating and ionization rates for this case are thus lower, but the main explanation for the lack of CR-induced differences is that even without CRs the shocked region is highly ionized and able to cool through molecular transitions to the CMB floor. As shown in Johnson and Bromm (2006), HD transitions are able to cool the gas down to the CMB temperature within a Hubble time. Thus, with these cooling mechanisms already in place, CRs can only serve to heat the gas, and the CR heating effect can dominate over molecular cooling only for more extreme star formation rates, as can be seen in the upper right panel of Fig. 6.4, where the gas temperature does not reach the CMB floor in the presence of strong CR heating.

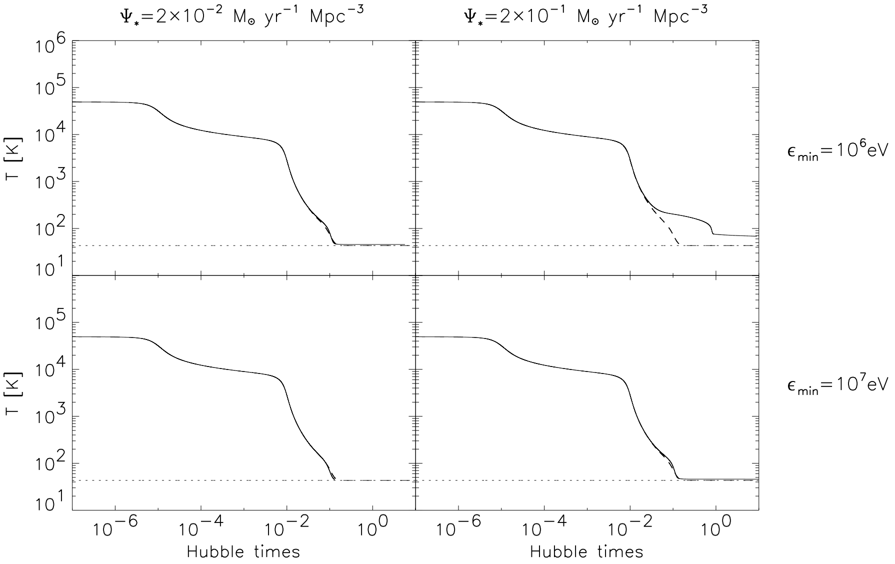

Figure 6.4: Thermal evolution of primordial gas clouds experiencing virialization shocks during the assembly of the first dwarf galaxies at $z = 15$. We adopt the same manner of presentation, and the same convention for the lines, as in Fig. 6.2. Notice that the presence of CRs has no impact on the evolution, with the exception of extremely high Pop III star formation rates *(upper right panel)*, where cooling to the CMB floor is prevented.

6.3.3 Local CR Feedback

Our study thus far has assumed that the CRs possibly created in the early Universe all become part of a homogeneous and isotropic background. However, if a particular minihalo is within sufficiently close range to a CR-accelerating PISN, the flux of CRs from the nearby PISN may have a greater effect on the evolution of the minihalo than that from the CR background.

The average CR luminosity associated with the PISN is given by

$$\begin{aligned} L_{\rm CR} &= 2\times10^{38}\,{\rm erg\,s^{-1}}\left(\frac{p_{\rm CR}}{0.1}\right) \\ &\times\left(\frac{E_{\rm SN}}{10^{52}\,{\rm erg}}\right)\left(\frac{\Delta t_{\rm SN}}{2\times10^{5}\,{\rm yr}}\right)^{-1} \ , \end{aligned} \tag{6.32}$$

where $\Delta t_{\rm SN}$ is the time over which the PISN emits CRs, here assumed to be approximately the time that passes from the beginning of the PISN to the end of its Sedov-Taylor phase of expansion (see Lagage and Cesarsky 1983). We can then estimate the CR flux, $f_{\rm CR}$, and energy density, $U_{\rm CR}$, emitted by the PISN using

$$f_{\rm CR} = \frac{L_{\rm CR}}{4\pi d^2} \ , \tag{6.33}$$

where d is the distance between the CR source and the minihalo. This can also be expressed as

$$\begin{aligned} f_{\rm CR} &\simeq 10^{-4}\,{\rm erg\,cm^{-2}\,s^{-1}}\left(\frac{p_{\rm CR}}{0.1}\right) \\ &\times\left(\frac{E_{\rm SN}}{10^{52}\,{\rm erg}}\right)\left(\frac{\Delta t_{\rm SN}}{2\times10^{5}\,{\rm yr}}\right)^{-1}\left(\frac{d}{100\,{\rm pc}}\right)^{-2} . \end{aligned} \tag{6.34}$$

The CR energy density can now be estimated to be

$$U_{\rm CR} \simeq \frac{f_{\rm CR}}{<\beta c>}\ . \tag{6.35}$$

For $p_{\rm CR} = 0.1$, $E_{\rm SN} = 10^{52}$ erg, and $\Delta t_{\rm SN} = 2{\times}10^{5}$ yr, $U_{\rm CR}$ can then be written as

$$U_{\rm CR} \simeq 5\times10^{-15}{\rm erg\,cm^{-3}}\left(\frac{d}{100\,{\rm pc}}\right)^{-2}\frac{\int_{\epsilon_{\rm min}}^{\epsilon_{\rm max}}\epsilon^{x}{\rm d}\epsilon}{\int_{\epsilon_{\rm min}}^{\epsilon_{\rm max}}\beta\epsilon^{x}{\rm d}\epsilon}\ . \tag{6.36}$$

This energy density is now used in Equ. (6.27) and Equ. (6.28) to determine the CR heating and ionization rates due to the CR emission from a single nearby PISN. Fig. 6.5 shows the thermal evolution of a minihalo under the influence of the CR flux from a 10^{52} erg PISN at 10 and 100 pc away. The PISN was assumed to emit CRs for 2×10^{5} yr with a minimum CR energy of 10^{6} eV. The resulting CR flux begins to impinge on the minihalo at times that correspond to two different stages during the collapse, when the gas cloud reaches a density of $n_{\rm H} = 1$ cm^{-3} and when it reaches $n_{\rm H} = 100$ cm^{-3}. At 10 pc, the CR emission allows the gas cloud to cool nearly to the CMB floor, while at 100 pc distance, it causes only a slight change in the thermal evolution of the gas. We also examined the evolution at a distance of 1 kpc from the PISN, but the CR effects were negligible.

For such a local burst of CR emission to have a noticeable impact on the evolution of the primordial gas, a PISN in very close proximity would be required. However, such a scenario is not very likely. In effect, a cloud at 10 pc distance from the explosion would be part of the same minihalo, and the strong UV radiation from the PISN progenitor would have evaporated any gas in its vicinity by photoionization-heating (e.g. Alvarez et al. 2006; Greif et al.

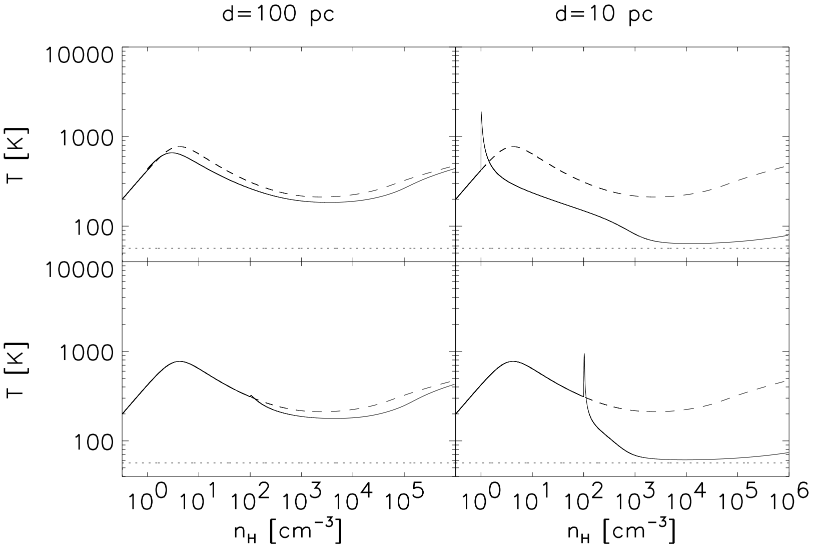

Figure 6.5: Thermal evolution of primordial gas in a minihalo under the effect of a PISN explosion 100 pc away *(left column)* and 10 pc away *(right column)*. The PISN is assumed to emit CRs for 2×10^5 yr with a minimum CR energy of 10^6 eV. We assume that the CR flux reaches the cloud during different stages in its collapse, characterized by the corresponding densities: $n_{\rm H} = 1$ cm^{-3} *(top row)* and $n_{\rm H} = 10^2$ cm^{-3} *(bottom row)*. The dashed lines show the evolution without CR flux prsent. The dotted lines show the CMB temperature floor at $z = 20$. Notice that the cloud has to be extremely close to the explosion site ($d \sim 10$ pc) to experience a significant effect. Such close proximity, however, is very unlikely due to the strong radiative feedback from the PISN progenitor.

2007). When considering realistic cases where the gas evolution in minihaloes could have been significantly impacted by CRs, one therefore needs to invoke a universal background that consists of the global contributions to the CR flux, as opposed to the burst-like emission from a single nearby PISN. However, at close distances the local CR feedback may still provide another source of ionization in nearby gas clouds, indirectly leading to increased molecular cooling, thus helping to facilitate collapse and possibly formation of lower-mass stars, as discussed below in Chapter 6.3.5.

6.3.4 Dependence on minimum CR energy

One of the crucial uncertainties concerning high-redshift CRs is the minimum energy $\epsilon_{\rm min}$ of the CRs that impinge upon a primordial cloud. Our default value of $\epsilon_{\rm min}$=10^6 eV derives from a simple estimate for the lowest possible energy that a CR proton could gain in a SN shock, though other processes may influence this value, possibly increasing or decreasing it. The minimum CR kinetic energy, however, is crucial, because the ionization cross section varies roughly as $\epsilon_{\rm CR}^{-1}$ for non-relativistic CRs with kinetic energies less than their rest mass energy but greater than $\sim$$10^5$ eV, the energy corresponding to a velocity of $\beta_0 \simeq 0.01$. Thus, higher-energy CRs will travel farther into the cloud before first ionizing a particle. Only lower-energy CRs will release a large portion of their energy into the cloud, and their absence can significantly lower the overall heating and ionization rate inside the cloud. This is especially apparent when looking at how the thermal evolution of the minihalo (Fig. 6.2) changes when $\epsilon_{\rm min}$ is increased. For typical star formation rates and $\epsilon_{\rm min} = 10^8$ eV, the impact of CRs becomes negligible. It is furthermore interesting to note that for a given $U_{\rm CR}$ and low $\epsilon_{\rm min}$ values ($\sim 10^6$ eV), using a powerlaw in momentum instead of a powerlaw in energy will give CR heating and ionization rates about an order of magnitude smaller than those found in the original calculations. This is because using a momentum powerlaw is equivalent to using a shallower spectral index at low CR energies, resulting in fewer low-energy CRs, and this again illustrates the importance of having a sufficient number of low-energy CRs to contribute to CR effects.

Decreasing $\epsilon_{\rm min}$ to arbitrarily low values, on the other hand, will not yield ever increasing CR ionization rates, as the cross section starts to quickly fall off below $\sim 10^5$ eV, and our lowest $\epsilon_{\rm min}$ of 10^6 eV is already sufficiently close to the peak in ionization cross section to obtain the maximum CR effects. This was confirmed by actually lowering the value of $\epsilon_{\rm min}$ to 1 and 10 keV to see how the heating and ionization rates changed. In both the minihalo and virialization shock case these rates were changed by less than a factor of two.

One of the reasons for the uncertainty in $\epsilon_{\rm min}$ is that the low-energy part of the CR spectrum is difficult to observe even inside the MW. The interaction of CRs with the solar wind and the resulting deflection by solar magnetic fields prevents any CRs with energies lower than around 10^8 eV from reaching Earth, and thus MW CRs below this energy cannot be directly detected. The Galactic CR spectrum is thought to extend to lower energies between 10^6 and 10^7 eV (e.g. Webber 1998). However, at non-relativistic energies the CR spectrum in the MW is expected to become much flatter due to ionization energy losses that would be much less relevant in the high-z IGM, as even at the redshifts we consider the density of the IGM is around three orders of magnitude lower than the average MW density.

6.3.5 Fragmentation scale

As is evident in Fig. 6.2, given a strong enough energy density, CRs can serve to lower the minimum temperature that a collapsing cloud inside a minihalo is able to reach. This could have important implications for the fragmentation scale of such gas clouds. We estimate the possible change in fragmentation scale due to CRs by assuming that the immediate progenitor of a protostar will have a mass approximately given by the Bonnor-Ebert (BE) mass (e.g. Johnson and Bromm 2006)

$$M_{\rm BE} \simeq 700\,{\rm M}_{\odot} \left(\frac{T_{\rm f}}{200\,{\rm K}}\right)^{3/2} \left(\frac{n_{\rm f}}{10^4\,{\rm cm}^{-3}}\right)^{-1/2} , \tag{6.37}$$

where $n_{\rm f}$ and $T_{\rm f}$ are the density and temperature of the primordial gas at the point when fragmentation occurs. For each of the cases shown in Fig. 6.2, the evolution of the BE mass was calculated as the cloud collapsed in free-fall. This evolution is shown in Fig. 6.6. For the three cases that had the most significant CR effects, the respective cooling and free-fall times were also examined. When the cooling time, $t_{\rm cool}$, first becomes shorter than the free-fall time, the gas can begin to cool and fall to the center of the DM halo unimpeded by gas pressure (Rees and Ostriker 1977; White and Rees 1978). As the cloud contracts, however, the density increases and the free-fall time becomes shorter, eventually falling back below the cooling time. At this point, when $t_{\rm ff} \sim t_{\rm cool}$, we evaluate the BE mass. This is the instance where the gas undergoes a phase of slow, quasi-hydrostatic contraction, what has been termed 'loitering phase' (see Bromm and Larson 2004). Slow contraction continues, and the gas will leave this loitering regime when its mass is high enough to become gravitationally unstable, thus triggering runaway collapse. Thus, the 'loitering phase' is the characteristic point in the evolution when

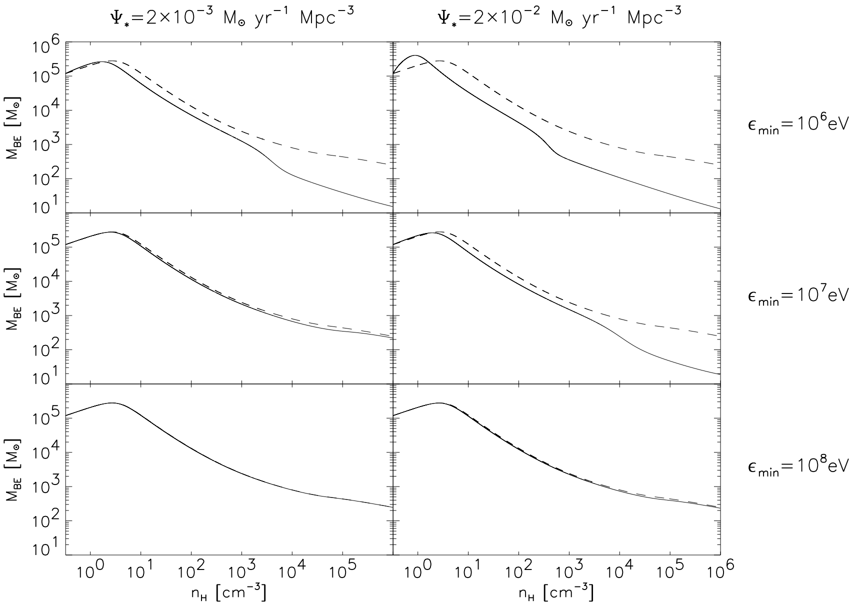

Figure 6.6: M_{BE} as a function of hydrogen number density for freely-falling clouds inside minihalos at $z \sim 20$. The curves correspond to the evolution shown in Fig. 6.2, and we adopt the same convention for the lines. Notice that the BE mass, which gives a rough indication for the final stellar mass, can decrease by up to a factor of 10, given that a sufficient flux of low-energy CRs is present.

fragmentation occurs and the BE mass is relevant, at least to zeroth order, given that star formation is too complex to allow reliable predictions from simple one-zone models such as considered here (e.g. Larson 2003).

Bearing this caveat in mind, we find that, with a sufficiently strong CR flux present, the gas density at which the 'loitering phase' occurs is increased by a factor of $\sim 10-100$, and the corresponding temperature decreased by a factor of 2 to 3. Evaluating Equ. (6.37) shows that the BE mass thus decreases by an order of magnitude down to around $10\,\mathrm{M}_{\odot}$. This is the mass scale of what has been termed 'Pop II.5' stars (e.g. Mackey et al. 2003; Johnson and Bromm

2006). This decrease in fragmentation scale occurs for CR ionization rates greater than $\sim 10^{-19}$ s^{-1}. A sufficiently large flux of low-energy CRs could thus have facilitated the fragmentation and collapse of primordial minihalo gas into Pop II.5 stars. Again, we emphasize the somewhat speculative nature of our argument regarding stellar mass scales. However, the general trend suggested here, that the presence of CRs in the early Universe tends to enable lower mass star formation, might well survive closer scrutiny with numerical simulations.

6.4 Summary and Discussion

We have investigated the effect of CRs on the thermal and chemical evolution of primordial gas clouds in two important sites for Pop III star formation: minihaloes and higher-mass haloes undergoing strong virialization shocks. We show that the presence of CRs has a negligible impact on the evolution in the latter case, since the primordial gas is able to cool to the CMB floor even without the help of CR ionization, and the direct CR heating is also unimportant unless extremely high star formation rates are assumed. Thus, the thermal and chemical evolution of haloes corresponding to the first dwarf galaxies is rather robust, and the CR emission from the deaths of previously formed Pop III stars will not initiate any feedback in these star formation sites. The impact of CRs on gas in minihaloes, which would typically have formed before the more massive dwarf systems, could have been much more pronounced, given a sufficiently low ϵ_{min} and Pop III star formation rates that are not too low. In each case, the effect of direct CR heating is weaker than the indirect molecular cooling that follows from the increased ionization due to CRs. The additional molecular cooling induced by the CRs allows the gas in a minihalo to cool to lower temperatures. For CR ionization rates above a critical value of $\sim 10^{-19}\ \mathrm{s}^{-1}$, we find that the mass scale of metal-free stars might be reduced to $\sim 10\,\mathrm{M}_\odot$, corresponding to what has been termed 'Pop II.5'.

If CRs did indeed facilitate Pop II.5 star formation in $z = 20$ minihaloes, the subsequent production of CRs would likely have been significantly reduced. Only one Pop III star is expected to form per minihalo, and it is plausible that with CRs present only one Pop II.5 star would be able to form in a given minihalo, as feedback effects of this first star may dissipate so much of the minihalo's remaining gas that no other stars can form in the same halo. A single Pop II.5 star per minihalo would imply no increase in the global number density of stars relative to the case of one Pop III star per minihalo. If Pop II.5 stars ever formed they would all die as lower explosion-energy CCSN. These stars would have lifetimes around 10^7 yr, not significantly longer than for the $\sim 100\,\mathrm{M}_\odot$ stars expected to form in minihaloes when CRs are unimportant, so Pop II.5 stars would still generate CRs almost instantaneously. However, their contribution to the CR energy density would be an order of magnitude less than that from a PISN due to the reduced explosion energy. This reduction in overall CR flux might be sufficient to prevent further CR-induced Pop II.5 star formation in minihaloes. Stars formed slightly later could then again be classical Pop III stars which would quickly restore a high level of CR energy density. The overall impact of CRs in the early Universe is thus difficult to determine, owing to the intricate feedback between star formation and CR production. We conclude, however, that CRs could significantly influence primordial star formation, and it will be important to further explore their role with more sophisticated numerical simulations.

Chapter 7

Outlook

Our understanding of the early universe and the first stars has grown rapidly over just the last several years. The picture of lone, highly massive Pop III stars has now expanded to include disk formation with possible co-formation of low-mass companion Pop III stars. A build-up of a cosmic ray background may also lead to population of relatively small primordial stars. Though results of various simulations still point to a top-heavy IMF, the range of possible Pop III masses is probably much larger than initially thought. Overall, as computational power and numerical simulations continue to improve, we are finding that the physical processes necessary to describe Pop III star formation are becoming increasingly similar those describing star formation in our own Milky Way. Disk formation, fragmentation, and stellar rotation are important to consider when studying star formation not only at $z = 0$, but at all redshifts.

In **Chapter 2**, we investigated the formation of metal-free, Pop III, stars within a minihalo at $z \simeq 20$ with a numerical simulation starting from cosmological initial conditions. Beginning from $z = 100$, we followed the collapsing gas in the center of the minihalo up to number densities of $10^{12}\,\mathrm{cm}^{-3}$. This allowed us to study the accretion onto the initial protostellar hydrostatic core, which we represent as a growing sink particle, in improved physical detail. A disk-like configuration assembles around the first protostar, and eventually a small multiple system forms, dominated by a binary with masses $\sim 40\,\mathrm{M}_{\odot}$ and $\sim 10\,\mathrm{M}_{\odot}$. If Pop III stars were to form typically in binaries or small multiples, this would have crucial consequences for the observational signature of the first stars, such as the nucleosynthetic pattern of the SNe they produce, and the gravitational-wave emission from possible Pop III black-hole binaries.

In **Chapter 3**, we examined the growth of metal-free, Pop III stars under radiative feedback. Using the sink particle method within a cosmological simulation, we modeled the effect of LW radiation emitted by the protostar, and employed a ray-tracing scheme to follow the growth of the surrounding H II region. We again find that a disk assembles around the first protostar, and that radiative feedback will not prevent further fragmentation of the disk to form multiple Pop III stars. The resuling heating and ionization of the gas leads to a shutoff of accretion once the main sink has grown to 15 $\mathrm{M}_{\odot}$ while the second sink has grown to 5 $\mathrm{M}_{\odot}$. There is little further accretion or fragmentation afterwards, indicating the most likely outcome is a massive Pop III binary. If Pop III stars were typically unable to grow to more than a few tens of solar masses, this would have important consequences for the occurence of pair-instability supernovae in the early universe as well as the Pop III chemical signature in the oldest stars observable today.

In **Chapter 4** we employed a cosmological simulation to estimate the rotation speed of Pop III stars within a minihalo. Again using sink particles, we measured the velocities and angular momenta of all particles that fall onto these protostellar regions. This allowed us to record the angular momentum of the sinks and estimate the rotational velocity of the Pop III stars expected to form within them. We find that there is sufficient angular momentum to yield rapidly rotating stars ($\gtrsim 1000$ km s^{-1}, or near break-up speeds). This indicates that Pop III stars likely experienced strong rotational mixing, impacting their structure and nucleosynthetic yields. A subset of them was also likely to result in hypernova explosions, and possibly GRBs.

In **Chapter 5**, we evaluated how the recently discovered supersonic relative velocity between the baryons and dark matter will affect the thermal and density evolution of the first gas clouds at $z \lesssim 50$. We find that the typical streaming velocities will have little effect on the gas evolution. Once the collapse begins, the subsequent evolution of the gas will be nearly indistinguishable from the case of no streaming, and star formation will still proceed in the same way, with no change in the characteristic Pop III stellar masses. Reionization is expected to be dominated by luminous sources that form within DM halos of masses $\gtrsim 10^8 M_\odot$, for which the effect of streaming should be negligible.

In **Chapter 6**, we explored the implications of a possible CR background generated during the first SNe explosions that end the brief lives of massive Pop III stars. CRs are expected to propagate away from SNe much faster than the metals produced at the same site. We show that a CR background could have significantly influenced the cooling and collapse of primordial gas clouds in minihalos around redshifts of $z \sim 15 - 20$, provided the CR flux was sufficient. The presence of CRs could indirectly enhance the molecular cooling in these regions, and we estimate that the resulting lower temperatures in these minihalos would yield a characteristic stellar mass as low as $\sim 10\,\mathrm{M}_\odot$.

Future work will aim to accomodate this developing picture of Pop III star formation in simulations of first galaxy formation. The metallicity and radiation produced by the first stars, and thus the environment in which future generations of stars formed within the first galaxies, depends crucially on the

Pop III IMF. Our predictions of the nature of the first galaxies will thus become increasingly detailed, and comparing these predictions with observations provided by instruments such as *JWST* and the Extremely Large Telescopes will be an exciting task for the future.

Stellar and dwarf archaeology will also continue to reveal more about metallicity production in the early universe, placing tighter constraints on primordial star formation. With large-scale surveys such as the *Sloan Extension for Galactic Understanding*, we will gain more knowledge of the chemical abundance patterns within stars residing in the local universe. Finding a PISN chemical signature within the oldest stars today may eventually provide strong evidence that some Pop III stars indeed reached very high masses. In the other extreme, the possibility remains for a truly metal-free star to be discovered in our own Milky Way or nearby dwarfs, observationally confirming the existence of a low-mass end of the Pop III IMF.

Stellar abundance observations are also becoming sufficiently detailed to place constraints on Pop III rotation. Observations presented by Chiappini et al. (2011) have recently found chemical signatures of rapidly rotating massive stars, which may have been Pop III. Rotation may furthermore facilitate Pop III gamma-ray bursts, and could someday be detected by the current *Swift* satellite and future instruments such as *JANUS* and *EXIST*, providing a more direct probe into the high-redshift universe.

In short, much work is left to be done on Pop III stars and the early universe. This work will strive to the ultimate goal of understanding how the universe came to its present state. Every step in this work will add to an increasingly clear picture of how the Dark Ages ended, how the first structures formed, and even how our own Galaxy was assembled. It is an exciting time to be part of an area of scientific research that is moving forward so rapidly, continuing to add pieces to the puzzle of how the universe evolved.

Bibliography

Abbasi, R. U., Abu-Zayyad, T., Allen, M., Amman, J. F., Archbold, G., Belov, K., Belz, J. W., Ben Zvi, S. Y., Bergman, D. R., Blake, S. A., and et al. (2008). First Observation of the Greisen-Zatsepin-Kuzmin Suppression. *Phys. Rev. Letters*, 100(10):101101–+.

Abel, T., Anninos, P., Zhang, Y., and Norman, M. L. (1997). Modeling primordial gas in numerical cosmology. *New. Astron.*, 2:181–207.

Abel, T., Bryan, G. L., and Norman, M. L. (2002). The Formation of the First Star in the Universe. *Sci.*, 295:93–98.

Ahn, K. and Shapiro, P. R. (2007). Does radiative feedback by the first stars promote or prevent second generation star formation? *MNRAS*, 375:881–908.

Alvarez, M. A., Bromm, V., and Shapiro, P. R. (2006). The H II Region of the First Star. *ApJ*, 639:621–632.

Asplund, M., Lambert, D. L., Nissen, P. E., Primas, F., and Smith, V. V. (2006). Lithium Isotopic Abundances in Metal-poor Halo Stars. *ApJ*, 644:229–259.

Balbus, S. A. and Hawley, J. F. (1991). A powerful local shear instability in weakly magnetized disks. I - Linear analysis. II - Nonlinear evolution. *ApJ*, 376:214–233.

Barkana, R. and Loeb, A. (2001). In the beginning: the first sources of light and the reionization of the universe. *Phys.Rep.*, 349:125–238.

Barnes, J. and Efstathiou, G. (1987). Angular momentum from tidal torques. *ApJ*, 319:575–600.

Bate, M. R., Bonnell, I. A., and Price, N. M. (1995). Modelling accretion in protobinary systems. *MNRAS*, 277:362–376.

Bate, M. R. and Burkert, A. (1997). Resolution requirements for smoothed particle hydrodynamics calculations with self-gravity. *MNRAS*, 288:1060–1072.

Beers, T. C. and Christlieb, N. (2005). The Discovery and Analysis of Very Metal-Poor Stars in the Galaxy. *ARA&A*, 43:531–580.

Belczynski, K., Bulik, T., Heger, A., and Fryer, C. (2007). The Lack of Gamma-Ray Bursts from Population III Binaries. *ApJ*, 664:986–999.

Belczynski, K., Bulik, T., and Rudak, B. (2004). The First Stellar Binary Black Holes: The Strongest Gravitational Wave Burst Sources. *ApJ*, 608:L45–L48.

Bell, A. R. (1978a). The acceleration of cosmic rays in shock fronts. I. *MNRAS*, 182:147–156.

Bell, A. R. (1978b). The acceleration of cosmic rays in shock fronts. II. *MNRAS*, 182:443–455.

Bell, A. R. and Lucek, S. G. (2001). Cosmic ray acceleration to very high energy through the non-linear amplification by cosmic rays of the seed magnetic field. *MNRAS*, 321:433–438.

Berezinskii, V. S. and Grigor'eva, S. I. (1988). A bump in the ultra-high energy cosmic ray spectrum. *A&A*, 199:1–12.

Beuther, H., Walsh, A. J., and Longmore, S. N. (2009). Hot High-Mass Accretion Disk Candidates. *ApJS*, 184:366–386.

Blandford, R. and Eichler, D. (1987). Particle acceleration at astrophysical shocks: A theory of cosmic ray origin. *Phys. Rep.*, 154:1–75.

Bodenheimer, P. (1995). Angular Momentum Evolution of Young Stars and Disks. *ARA&A*, 33:199–238.

Bond, J. R., Arnett, W. D., and Carr, B. J. (1984). The evolution and fate of Very Massive Objects. *ApJ*, 280:825–847.

Boss, A. P. (1999). Collapse and Fragmentation of Molecular Cloud Cores. VI. Slowly Rotating Magnetic Clouds. *ApJ*, 520:744–750.

Boss, A. P. and Myhill, E. A. (1995). Collapse and Fragmentation of Molecular Cloud Cores. III. Initial Differential Rotation. *ApJ*, 451:218–+.

Bromm, V., Coppi, P. S., and Larson, R. B. (1999). Forming the First Stars in the Universe: The Fragmentation of Primordial Gas. *ApJ*, 527:L5–L8.

Bromm, V., Coppi, P. S., and Larson, R. B. (2002). The Formation of the First Stars. I. The Primordial Star-forming Cloud. *ApJ*, 564:23–51.

Bromm, V., Ferrara, A., Coppi, P. S., and Larson, R. B. (2001a). The fragmentation of pre-enriched primordial objects. *MNRAS*, 328:969–976.

Bromm, V., Ferrara, A., Coppi, P. S., and Larson, R. B. (2001b). The fragmentation of pre-enriched primordial objects. *MNRAS*, 328:969–976.

Bromm, V., Kudritzki, R. P., and Loeb, A. (2001c). Generic Spectrum and Ionization Efficiency of a Heavy Initial Mass Function for the First Stars. *ApJ*, 552:464–472.

Bromm, V. and Larson, R. B. (2004). The First Stars. *ARA&A*, 42:79–118.

Bromm, V. and Loeb, A. (2002). The Expected Redshift Distribution of Gamma-Ray Bursts. *ApJ*, 575:111–116.

Bromm, V. and Loeb, A. (2003). The formation of the first low-mass stars from gas with low carbon and oxygen abundances. *Nature*, 425:812–814.

Bromm, V. and Loeb, A. (2004). Accretion onto a primordial protostar. *New Astron.*, 9:353–364.

Bromm, V. and Loeb, A. (2006). High-Redshift Gamma-Ray Bursts from Population III Progenitors. *ApJ*, 642:382–388.

Bromm, V., Yoshida, N., and Hernquist, L. (2003). The First Supernova Explosions in the Universe. *ApJ*, 596:L135–L138.

Bromm, V., Yoshida, N., Hernquist, L., and McKee, C. F. (2009). The Formation of the First Stars and Galaxies. *Nature*, 459:49–54.

Caselli, P., Benson, P. J., Myers, P. C., and Tafalla, M. (2002). Dense Cores in Dark Clouds. XIV. $N_2H^+(1-0)$ Maps of Dense Cloud Cores. *ApJ*, 572:238–263.

Cesaroni, R., Galli, D., Lodato, G., Walmsley, C. M., and Zhang, Q. (2007). Disks Around Young O-B (Proto)Stars: Observations and Theory. *Protostars and Planets V*, pages 197–212.

Cesaroni, R., Galli, D., Lodato, G., Walmsley, M., and Zhang, Q. (2006). The critical role of disks in the formation of high-mass stars. *Nature*, 444:703–706.

Chiappini, C., Frischknecht, U., Meynet, G., Hirschi, R., Barbuy, B., Pignatari, M., Decressin, T., and Maeder, A. (2011). Imprints of fast-rotating massive stars in the Galactic Bulge. *Nature*, 472:454–457.

Christlieb, N., Bessell, M. S., Beers, T. C., Gustafsson, B., Korn, A., Barklem, P. S., Karlsson, T., Mizuno-Wiedner, M., and Rossi, S. (2002). A stellar relic from the early Milky Way. *Nature*, 419:904–906.

Ciardi, B. and Ferrara, A. (2005). The First Cosmic Structures and Their Effects. *Space Sci. Rev.*, 116:625–705.

Clark, P. C., Glover, S. C. O., and Klessen, R. S. (2008). The First Stellar Cluster. *ApJ*, 672:757–764.

Clark, P. C., Glover, S. C. O., Klessen, R. S., and Bromm, V. (2011a). Gravitational fragmentation in turbulent primordial gas and the initial mass function of Population III stars. *ApJ*, 727:110–+.

Clark, P. C., Glover, S. C. O., Smith, R. J., Greif, T. H., Klessen, R. S., and Bromm, V. (2011b). The Formation and Fragmentation of Disks Around Primordial Protostars. *Sci*, 331:1040–.

Clarke, C. J. and Bromm, V. (2003). The characteristic stellar mass as a function of redshift. *MNRAS*, 343:1224–1230.

Daigne, F., Olive, K. A., Silk, J., Stoehr, F., and Vangioni, E. (2006). Hierarchical Growth and Cosmic Star Formation: Enrichment, Outflows, and Supernova Rates. *ApJ*, 647:773–786.

Dalal, N., Pen, U., and Seljak, U. (2010). Large-scale BAO signatures of the smallest galaxies. *JCAP*, 11:7–+.

de Gouveia Dal Pino, E. M. and Lazarian, A. (2001). Constraints on the Acceleration of Ultra-High-Energy Cosmic Rays in Accretion-induced Collapse Pulsars. *ApJ*, 560:358–364.

De Marco, D. (2005). Propagation of UHECRs. *Proccedings of Rencontres de Moriond: Very High Energy Phenomena in the Universe, preprint (arXiv: 0506412).*

Dicke, R. H., Peebles, P. J. E., Roll, P. G., and Wilkinson, D. T. (1965). Cosmic Black-Body Radiation. *ApJ*, 142:414–419.

Draine, B. T. and Bertoldi, F. (1996). Structure of Stationary Photodissociation Fronts. *ApJ*, 468:269–+.

Duquennoy, A. and Mayor, M. (1991). Multiplicity among solar-type stars in the solar neighbourhood. II - Distribution of the orbital elements in an unbiased sample. *A&A*, 248:485–524.

Eisenstein, D. J. and Hut, P. (1998). HOP: A New Group-Finding Algorithm for N-Body Simulations. *ApJ*, 498:137–+.

Ekström, S., Meynet, G., Chiappini, C., Hirschi, R., and Maeder, A. (2008a). Effects of rotation on the evolution of primordial stars. *A&A*, 489:685–698.

Ekström, S., Meynet, G., Maeder, A., and Barblan, F. (2008b). Evolution towards the critical limit and the origin of Be stars. *A&A*, 478:467–485.

Field, G. B. (1995). Is the Dynamo Theory of the Galactic Magnetic Field Wrong? In A. Ferrara, C. F. McKee, C. Heiles, & P. R. Shapiro, editor, *The Physics of the Interstellar Medium and Intergalactic Medium*, volume 80 of *Astronomical Society of the Pacific Conference Series*, pages 1–+.

Frebel, A., Aoki, W., Christlieb, N., Ando, H., Asplund, M., Barklem, P. S., Beers, T. C., Eriksson, K., Fechner, C., Fujimoto, M. Y., Honda, S., Kajino, T., Minezaki, T., Nomoto, K., Norris, J. E., and Ryan, S. G. (2005). Nucleosynthetic signatures of the first stars. *Nature*, 434:871–873.

Frebel, A. and Bromm, V. (2010). Dwarf archaeology: Probing the first enrichment events with low-luminosity galaxies. *MNRAS, submitted (arXiv: 1010.1261).*

Frebel, A., Johnson, J. L., and Bromm, V. (2007). Probing the formation of the first low-mass stars with stellar archaeology. *MNRAS*, 380:L40–L44.

Frebel, A., Johnson, J. L., and Bromm, V. (2009). The minimum stellar metallicity observable in the Galaxy. *MNRAS*, 392:L50–L54.

Fryer, C. L., Woosley, S. E., and Hartmann, D. H. (1999). Formation Rates of Black Hole Accretion Disk Gamma-Ray Bursts. *ApJ*, 526:152–177.

Galván-Madrid, R., Peters, T., Keto, E. R., Mac Low, M.-M., Banerjee, R., and Klessen, R. S. (2011). Time variability in simulated ultracompact and hypercompact H II regions. *MNRAS, in press.*

Gao, L., White, S. D. M., Jenkins, A., Frenk, C. S., and Springel, V. (2005). Early structure in ΛCDM. *MNRAS*, 363:379–392.

Ginzburg, V. L. and Syrovatskii, S. I. (1969). *The origin of cosmic rays*. Gordon and Breach, New York.

Glover, S. (2005). The Formation Of The First Stars In The Universe. *Space Sci. Rev.*, 117:445–508.

Glover, S. C. O. and Abel, T. (2008). Uncertainties in H2 and HD chemistry and cooling and their role in early structure formation. *MNRAS*, 388:1627–1651.

Gnedin, N. Y., Ferrara, A., and Zweibel, E. G. (2000). Generation of the Primordial Magnetic Fields during Cosmological Reionization. *ApJ*, 539:505–516.

Goodman, A. A., Benson, P. J., Fuller, G. A., and Myers, P. C. (1993). Dense cores in dark clouds. VIII - Velocity gradients. *ApJ*, 406:528–547.

Gou, L. J., Mészáros, P., Abel, T., and Zhang, B. (2004). Detectability of Long Gamma-Ray Burst Afterglows from Very High Redshifts. *ApJ*, 604:508–520.

Greif, T., Springel, V., White, S., Glover, S., Clark, P., Smith, R., Klessen, R., and Bromm, V. (2011). Simulations on a Moving Mesh: The Clustered Formation of Population III Protostars. *ApJ*, 737:75–+.

Greif, T. H. and Bromm, V. (2006). Two populations of metal-free stars in the early Universe. *MNRAS*, 373:128–138.

Greif, T. H., Glover, S. C. O., Bromm, V., and Klessen, R. S. (2010). The First Galaxies: Chemical Enrichment, Mixing, and Star Formation. *ApJ*, 716:510–520.

Greif, T. H., Johnson, J. L., Bromm, V., and Klessen, R. S. (2007). The First Supernova Explosions: Energetics, Feedback, and Chemical Enrichment. *ApJ*, 670:1–14.

Greif, T. H., Johnson, J. L., Klessen, R. S., and Bromm, V. (2008). The first galaxies: assembly, cooling and the onset of turbulence. *MNRAS*, 387:1021–1036.

Greif, T. H., Johnson, J. L., Klessen, R. S., and Bromm, V. (2009). The observational signature of the first HII regions. *MNRAS*, 399:639–649.

Greisen, K. (1966). End to the Cosmic-Ray Spectrum? *Phys. Rev. Let.*, 16:748–750.

Haiman, Z., Thoul, A. A., and Loeb, A. (1996). Cosmological Formation of Low-Mass Objects. *ApJ*, 464:523–+.

Heger, A., Fryer, C. L., Woosley, S. E., Langer, N., and Hartmann, D. H. (2003). How Massive Single Stars End Their Life. *ApJ*, 591:288–300.

Heger, A. and Langer, N. (2000). Presupernova Evolution of Rotating Massive Stars. II. Evolution of the Surface Properties. *ApJ*, 544:1016–1035.

Heger, A. and Woosley, S. E. (2002). The Nucleosynthetic Signature of Population III. *ApJ*, 567:532–543.

Heger, A., Woosley, S. E., and Spruit, H. C. (2005). Presupernova Evolution of Differentially Rotating Massive Stars Including Magnetic Fields. *ApJ*, 626:350–363.

Hosokawa, T., Yorke, H. W., and Omukai, K. (2010). Evolution of Massive Protostars Via Disk Accretion. *ApJ*, 721:478–492.

Huang, W. and Gies, D. R. (2008). Stellar Rotation in Field and Cluster B Stars. *ApJ*, 683:1045–1051.

Hubble, E. (1929). A Relation between Distance and Radial Velocity among Extra-Galactic Nebulae. *PNAS*, 15:168–173.

Hunter, C. (1977). The collapse of unstable isothermal spheres. *ApJ*, 218:834–845.

Ichiki, K., Takahashi, K., Ohno, H., Hanayama, H., and Sugiyama, N. (2006). Cosmological Magnetic Field: A Fossil of Density Perturbations in the Early Universe. *Sci.*, 311:827–829.

Izzard, R. G., Ramirez-Ruiz, E., and Tout, C. A. (2004). Formation rates of core-collapse supernovae and gamma-ray bursts. *MNRAS*, 348:1215–1228.

Jang-Condell, H. and Hernquist, L. (2001). First Structure Formation: A Simulation of Small-Scale Structure at High Redshift. *ApJ*, 548:68–78.

Jappsen, A. and Klessen, R. S. (2004). Protostellar angular momentum evolution during gravoturbulent fragmentation. *A&A*, 423:1–12.

Johnson, J. L. and Bromm, V. (2006). The cooling of shock-compressed primordial gas. *MNRAS*, 366:247–256.

Johnson, J. L., Greif, T. H., and Bromm, V. (2007). Local Radiative Feedback in the Formation of the First Protogalaxies. *ApJ*, 665:85–95.

Johnson, J. L., Greif, T. H., Bromm, V., Klessen, R. S., and Ippolito, J. (2009). The first galaxies: signatures of the initial starburst. *MNRAS*, 399:37–47.

Johnson, J. L. and Khochfar, S. (2011). Suppression of accretion on to low-mass Population III stars. *MNRAS*, 413:1184–1191.

Karlsson, T., Johnson, J. L., and Bromm, V. (2008). Uncovering the Chemical Signature of the First Stars in the Universe. *ApJ*, 679:6–16.

Kashlinsky, A. and Rees, M. J. (1983). Formation of population III stars and pregalactic evolution. *MNRAS*, 205:955–971.

Keto, E. (2007). The Formation of Massive Stars: Accretion, Disks, and the Development of Hypercompact H II Regions. *ApJ*, 666:976–981.

Kitayama, T., Yoshida, N., Susa, H., and Umemura, M. (2004). The Structure and Evolution of Early Cosmological H II Regions. *ApJ*, 613:631–645.

Koenigl, A. (1991). Disk accretion onto magnetic T Tauri stars. *ApJ*, 370:L39–L43.

Kratter, K. M. and Matzner, C. D. (2006). Fragmentation of massive protostellar discs. *MNRAS*, 373:1563–1576.

Kratter, K. M., Matzner, C. D., Krumholz, M. R., and Klein, R. I. (2010). On the Role of Disks in the Formation of Stellar Systems: A Numerical Parameter Study of Rapid Accretion. *ApJ*, 708:1585–1597.

Kratter, K. M. and Murray-Clay, R. A. (2011). Fragment Production and Survival in Irradiated Disks: A Comprehensive Cooling Criterion. *ApJ, accepted, arXiv: 1107.0728.*

Kraus, S., Hofmann, K., Menten, K. M., Schertl, D., Weigelt, G., Wyrowski, F., Meilland, A., Perraut, K., Petrov, R., Robbe-Dubois, S., Schilke, P., and Testi, L. (2010). A hot compact dust disk around a massive young stellar object. *Nature*, 466:339–342.

Kronberg, P. P., Lesch, H., and Hopp, U. (1999). Magnetization of the Intergalactic Medium by Primeval Galaxies. *ApJ*, 511:56–64.

Krumholz, M. R., Klein, R. I., and McKee, C. F. (2007). Radiation-Hydrodynamic Simulations of Collapse and Fragmentation in Massive Protostellar Cores. *ApJ*, 656:959–979.

Krumholz, M. R., Klein, R. I., McKee, C. F., Offner, S. S. R., and Cunningham, A. J. (2009). The Formation of Massive Star Systems by Accretion. *Sci.*, 323:754–.

Kudritzki, R. P. (2002). Line-driven Winds, Ionizing Fluxes, and Ultraviolet Spectra of Hot Stars at Extremely Low Metallicity. I. Very Massive O Stars. *ApJ*, 577:389–408.

Kuiper, R., Klahr, H., Beuther, H., and Henning, T. (2011). Three-dimensional Simulation of Massive Star Formation in the Disk Accretion Scenario. *ApJ*, 732:20–+.

Lacey, C. and Cole, S. (1993). Merger rates in hierarchical models of galaxy formation. *MNRAS*, 262:627–649.

Lagage, P. O. and Cesarsky, C. J. (1983). The maximum energy of cosmic rays accelerated by supernova shocks. *A&A*, 125:249–257.

Larson, R. B. (1969). Numerical calculations of the dynamics of collapsing proto-star. *MNRAS*, 145:271–+.

Larson, R. B. (1998). Early star formation and the evolution of the stellar initial mass function in galaxies. *MNRAS*, 301:569–581.

Larson, R. B. (2003). The physics of star formation. *Rep. Prog. Phys.*, 66:1651–1697.

Lee, C., Brown, G. E., and Wijers, R. A. M. J. (2002). Discovery of a Black Hole Mass-Period Correlation in Soft X-Ray Transients and Its Implication for Gamma-Ray Burst and Hypernova Mechanisms. *ApJ*, 575:996–1006.

Lee, W. H. and Ramirez-Ruiz, E. (2006). Accretion Modes in Collapsars: Prospects for Gamma-Ray Burst Production. *ApJ*, 641:961–971.

Lodato, G. and Rice, W. K. M. (2005). Testing the locality of transport in self-gravitating accretion discs - II. The massive disc case. *MNRAS*, 358:1489–1500.

Loeb, A. (2010). *How Did the First Stars and Galaxies Form?* Princeton University Press, Princeton.

Longair, M. S. (1994). *High energy astrophysics. Vol.2: Stars, the galaxy and the interstellar medium.* Cambridge University Press, Cambridge.

Machida, M. N., Omukai, K., Matsumoto, T., and Inutsuka, S. (2008). Conditions for the Formation of First-Star Binaries. *ApJ*, 677:813–827.

Machida, M. N., Omukai, K., Matsumoto, T., and Inutsuka, S.-i. (2006). The First Jets in the Universe: Protostellar Jets from the First Stars. *ApJ*, 647:L1–L4.

Mackey, J., Bromm, V., and Hernquist, L. (2003). Three Epochs of Star Formation in the High-Redshift Universe. *ApJ*, 586:1–11.

Madau, P., Ferrara, A., and Rees, M. J. (2001). Early Metal Enrichment of the Intergalactic Medium by Pregalactic Outflows. *ApJ*, 555:92–105.

Madau, P. and Rees, M. J. (2001). Massive Black Holes as Population III Remnants. *ApJ*, 551:L27–L30.

Maeder, A. (1987). Evidences for a bifurcation in massive star evolution. The ON-blue stragglers. *A&A*, 178:159–169.

Maeder, A. and Meynet, G. (2000). The Evolution of Rotating Stars. *ARA&A*, 38:143–190.

Maio, U., Koopmans, L. V. E., and Ciardi, B. (2010). The impact of primordial supersonic flows on early structure formation, reionization, and the lowest-mass dwarf galaxies. *MNRAS, submitted (arXiv: 1011.4006).*

Maki, H. and Susa, H. (2007). Dissipation of Magnetic Flux in Primordial Star Formation: From Run-away Phase to Mass-Accretion Phase. *PASJ*, 59:787–797.

Martel, H., Evans, II, N. J., and Shapiro, P. R. (2006). Fragmentation and Evolution of Molecular Clouds. I. Algorithm and First Results. *ApJS*, 163:122–144.

Matt, S. and Pudritz, R. E. (2005). Accretion-powered Stellar Winds as a Solution to the Stellar Angular Momentum Problem. *ApJ*, 632:L135–L138.

McDowell, M. R. C. (1961). On the formation of H2 in H I regions. *The Observatory*, 81:240–243.

McKee, C. F. and Ostriker, E. C. (2007). Theory of Star Formation. *ARA&A*, 45:565–687.

McKee, C. F. and Tan, J. C. (2002). Massive star formation in 100,000 years from turbulent and pressurized molecular clouds. *Nature*, 416:59–61.

McKee, C. F. and Tan, J. C. (2008). The Formation of the First Stars. II. Radiative Feedback Processes and Implications for the Initial Mass Function. *ApJ*, 681:771–797.

Miralda-Escudé, J. (2003). The Dark Age of the Universe. *Sci.*, 300:1904–1909.

Mori, M., Ferrara, A., and Madau, P. (2002). Early Metal Enrichment by Pregalactic Outflows. II. Three-dimensional Simulations of Blow-Away. *ApJ*, 571:40–55.

Muñoz, J. A. and Loeb, A. (2011). Constraining the Minimum Mass of High-redshift Galaxies and their Contribution to the Ionization State of the Intergalactic Medium. *ApJ*, 729:99–+.

Naoz, S. and Bromberg, O. (2007). An observational limit on the earliest gamma-ray bursts. *MNRAS*, 380:757–762.

Narayan, R. and Yi, I. (1994). Advection-dominated accretion: A self-similar solution. *ApJ*, 428:L13–L16.

Navarro, J. F. and White, S. D. M. (1994). Simulations of dissipative galaxy formation in hierarchically clustering universes-2. Dynamics of the baryonic component in galactic haloes. *MNRAS*, 267:401–412.

Nomoto, K., Maeda, K., Umeda, H., Ohkubo, T., Deng, J., and Mazzali, P. (2003). Nucleosynthesis in Black-Hole-Forming Supernovae and Extremely Metal-Poor Stars. *Prog. Theor. Phys. Suppl.*, 151:44–53.

Norman, M. L., O'Shea, B. W., and Paschos, P. (2004). Did Massive Primordial Stars Preenrich the Lyα Forest? *ApJ*, 601:L115–L118.

Nugis, T. and Lamers, H. J. G. L. M. (2000). Mass-loss rates of Wolf-Rayet stars as a function of stellar parameters. *A&A*, 360:227–244.

Omukai, K. (2000). Protostellar Collapse with Various Metallicities. *ApJ*, 534:809–824.

Omukai, K. and Inutsuka, S.-i. (2002). An upper limit on the mass of a primordial star due to the formation of an Hii region: the effect of ionizing radiation force. *MNRAS*, 332:59–64.

Omukai, K. and Nishi, R. (1998). Formation of Primordial Protostars. *ApJ*, 508:141–150.

Omukai, K. and Palla, F. (2003). Formation of the First Stars by Accretion. *ApJ*, 589:677–687.

O'Shea, B. W., Abel, T., Whalen, D., and Norman, M. L. (2005). Forming a Primordial Star in a Relic H II Region. *ApJ*, 628:L5–L8.

Osterbrock, D. E. and Ferland, G. J. (2006). *Astrophysics of gaseous nebulae and active galactic nuclei.* University Science Books, Sausalito, CA.

Palla, F., Salpeter, E. E., and Stahler, S. W. (1983). Primordial star formation - The role of molecular hydrogen. *ApJ*, 271:632–641.

Papaloizou, J. C. B. and Lin, D. N. C. (1995). Theory Of Accretion Disks I: Angular Momentum Transport Processes. *ARA&A*, 33:505–540.

Pawlik, A. H., Milosavljević, M., and Bromm, V. (2011). The First Galaxies: Assembly of Disks and Prospects for Direct Detection. *ApJ*, 731:54–+.

Penston, M. V. (1969). Dynamics of self-gravitating gaseous spheres-III. Analytical results in the free-fall of isothermal cases. *MNRAS*, 144:425–+.

Penzias, A. A. and Wilson, R. W. (1965). A Measurement of Excess Antenna Temperature at 4080 Mc/s. *ApJ*, 142:419–421.

Peters, T., Banerjee, R., Klessen, R. S., Mac Low, M.-M., Galván-Madrid, R., and Keto, E. R. (2010). H II Regions: Witnesses to Massive Star Formation. *ApJ*, 711:1017–1028.

Petrovic, J., Langer, N., Yoon, S., and Heger, A. (2005). Which massive stars are gamma-ray burst progenitors? *A&A*, 435:247–259.

Pringle, J. E. (1981). Accretion discs in astrophysics. *ARA&A*, 19:137–162.

Rees, M. J. (2006). Origin of cosmic magnetic fields. *AN*, 327:395–+.

Rees, M. J. and Ostriker, J. P. (1977). Cooling, dynamics and fragmentation of massive gas clouds - Clues to the masses and radii of galaxies and clusters. *MNRAS*, 179:541–559.

Ripamonti, E., Haardt, F., Ferrara, A., and Colpi, M. (2002). Radiation from the first forming stars. *MNRAS*, 334:401–418.

Rollinde, E., Vangioni, E., and Olive, K. (2005). Cosmological Cosmic Rays and the Observed ^{6}Li Plateau in Metal-poor Halo Stars. *ApJ*, 627:666–673.

Rollinde, E., Vangioni, E., and Olive, K. A. (2006). Population III Generated Cosmic Rays and the Production of ^{6}Li. *ApJ*, 651:658–666.

Ruderman, M. A. (1974). Possible Consequences of Nearby Supernova Explosions for Atmospheric Ozone and Terrestrial Life. *Sci.*, 184:1079–1081.

Saigo, K., Matsumoto, T., and Umemura, M. (2004). The Formation of Population III Binaries. *ApJ*, 615:L65–L68.

Salvaterra, R., Della Valle, M., Campana, S., Chincarini, G., Covino, S., D'Avanzo, P., Fernández-Soto, A., and Guidorzi, C. e. a. (2009). GRB090423 at a redshift of z˜8.1. *Nature*, 461:1258–1260.

Schaller, G., Schaerer, D., Meynet, G., and Maeder, A. (1992). New grids of stellar models from 0.8 to 120 solar masses at Z = 0.020 and Z = 0.001. *A&AS*, 96:269–331.

Schleicher, D. R. G., Banerjee, R., Sur, S., Arshakian, T. G., Klessen, R. S., Beck, R., and Spaans, M. (2010). Small-scale dynamo action during the formation of the first stars and galaxies. I. The ideal MHD limit. *A&A*, 522:A115+.

Schlickeiser, R. (2002). *Cosmic Ray Astrophysics*. Astronomy and Astrophysics Library; Physics and Astronomy Online Library, Berlin.

Schneider, R., Ferrara, A., Natarajan, P., and Omukai, K. (2002). First Stars, Very Massive Black Holes, and Metals. *ApJ*, 571:30–39.

Schneider, R., Omukai, K., Inoue, A. K., and Ferrara, A. (2006). Fragmentation of star-forming clouds enriched with the first dust. *MNRAS*, 369:1437–1444.

Sesana, A., Haardt, F., Madau, P., and Volonteri, M. (2005). The Gravitational Wave Signal from Massive Black Hole Binaries and Its Contribution to the LISA Data Stream. *ApJ*, 623:23–30.

Shakura, N. I. and Sunyaev, R. A. (1973). Black holes in binary systems. Observational appearance. *A&A*, 24:337–355.

Shapiro, P. R. and Kang, H. (1987). Hydrogen molecules and the radiative cooling of pregalactic shocks. *ApJ*, 318:32–65.

Shchekinov, Y. A. and Vasiliev, E. O. (2004). Primordial star formation triggered by UV photons from UHECR. *A&A*, 419:19–23.

Shu, F., Najita, J., Ostriker, E., Wilkin, F., Ruden, S., and Lizano, S. (1994). Magnetocentrifugally driven flows from young stars and disks. 1: A generalized model. *ApJ*, 429:781–796.

Shu, F. H. (1977). Self-similar collapse of isothermal spheres and star formation. *ApJ*, 214:488–497.

Shu, F. H., Lizano, S., Galli, D., Cantó, J., and Laughlin, G. (2002). Self-similar Champagne Flows in H II Regions. *ApJ*, 580:969–979.

Shull, J. M. and van Steenberg, M. E. (1985). X-ray secondary heating and ionization in quasar emission-line clouds. *ApJ*, 298:268–274.

Silk, J. and Langer, M. (2006). On the first generation of stars. *MNRAS*, 371:444–450.

Simon, M., Ghez, A. M., Leinert, C., Cassar, L., Chen, W. P., Howell, R. R., Jameson, R. F., Matthews, K., Neugebauer, G., and Richichi, A. (1995). A lunar occultation and direct imaging survey of multiplicity in the Ophiuchus and Taurus star-forming regions. *ApJ*, 443:625–637.

Smith, B. D. and Sigurdsson, S. (2007). The Transition from the First Stars to the Second Stars in the Early Universe. *ApJ*, 661:L5–L8.

Smith, R. J., Glover, S. C. O., Clark, P. C., Greif, T., and Klessen, R. S. (2011). The effects of accretion luminosity upon fragmentation in the early universe. *MNRAS*, 414:3633–3644.

Sokasian, A., Yoshida, N., Abel, T., Hernquist, L., and Springel, V. (2004). Cosmic reionization by stellar sources: population III stars. *MNRAS*, 350:47–65.

Spitzer, L. (1978). *Physical Processes in the Interstellar Medium*. Wiley, New York.

Spitzer, Jr., L. and Scott, E. H. (1969). Heating of H i Regions by Energetic Particles. II. Interaction Between Secondaries and Thermal Electrons. *ApJ*, 158:161–+.

Spitzer, Jr., L. and Tomasko, M. G. (1968). Heating of H i Regions by Energetic Particles. *ApJ*, 152:971–+.

Springel, V. (2005). The cosmological simulation code GADGET-2. *MNRAS*, 364:1105–1134.

Springel, V. and Hernquist, L. (2002). Cosmological smoothed particle hydrodynamics simulations: the entropy equation. *MNRAS*, 333:649–664.

Springel, V., Yoshida, N., and White, S. D. M. (2001). GADGET: a code for collisionless and gasdynamical cosmological simulations. *New Astron.*, 6:79–117.

Spruit, H. C. (2002). Dynamo action by differential rotation in a stably stratified stellar interior. *A&A*, 381:923–932.

Stacy, A., Bromm, V., and Loeb, A. (2011). Rotation speed of the first stars. *MNRAS*, 413:543–553.

Stacy, A., Greif, T. H., and Bromm, V. (2010). The first stars: formation of binaries and small multiple systems. *MNRAS*, 403:45–60.

Stahler, S. W., Palla, F., and Salpeter, E. E. (1986). Primordial stellar evolution - The protostar phase. *ApJ*, 302:590–605.

Suda, T., Aikawa, M., Machida, M. N., Fujimoto, M. Y., and Iben, I. J. (2004). Is HE 0107-5240 A Primordial Star? The Characteristics of Extremely Metal-Poor Carbon-Rich Stars. *ApJ*, 611:476–493.

Suwa, Y. and Ioka, K. (2010). Can Gamma-Ray Burst Jets Break Out the First Stars? *arXiv:1009.6001.*

Tan, J. C. and Blackman, E. G. (2004). Protostellar Disk Dynamos and Hydromagnetic Outflows in Primordial Star Formation. *ApJ*, 603:401–413.

Tan, J. C. and McKee, C. F. (2004). The Formation of the First Stars. I. Mass Infall Rates, Accretion Disk Structure, and Protostellar Evolution. *ApJ*, 603:383–400.

Tanvir, N. R., Fox, D. B., Levan, A. J., Berger, E., Wiersema, K., Fynbo, J. P. U., Cucchiara, A., Krühler, T., Gehrels, N., Bloom, J. S., and Greiner, J. e. a. (2009). A γ-ray burst at a redshift of z˜8.2. *Nature*, 461:1254–1257.

Tegmark, M., Silk, J., Rees, M. J., Blanchard, A., Abel, T., and Palla, F. (1997). How Small Were the First Cosmological Objects? *ApJ*, 474:1–+.

Tormen, G., Bouchet, F. R., and White, S. D. M. (1997). The structure and dynamical evolution of dark matter haloes. *MNRAS*, 286:865–884.

Tornatore, L., Ferrara, A., and Schneider, R. (2007). Population III stars: hidden or disappeared? *MNRAS*, 382:945–950.

Torres, D. F., Boldt, E., Hamilton, T., and Loewenstein, M. (2002). Nearby quasar remnants and ultrahigh-energy cosmic rays. *Phys. Rev. D*, 66(2):023001–+.

Trac, H. and Gnedin, N. Y. (2009). Computer Simulations of Cosmic Reionization. *(arXiv: 0906.4348)*.

Trenti, M. and Stiavelli, M. (2009). Formation Rates of Population III Stars and Chemical Enrichment of Halos during the Reionization Era. *ApJ*, 694:879–892.

Tseliakhovich, D., Barkana, R., and Hirata, C. (2010). Suppression and Spatial Variation of Early Galaxies and Minihalos. *(arXiv: 1012.2574)*.

Tseliakhovich, D. and Hirata, C. (2010). Relative velocity of dark matter and baryonic fluids and the formation of the first structures. *Phys. Rev. D*, 82(8):083520–+.

Tumlinson, J. (2006). Chemical Evolution in Hierarchical Models of Cosmic Structure. I. Constraints on the Early Stellar Initial Mass Function. *ApJ*, 641:1–20.

Tumlinson, J. (2007). Carbon-enhanced Hyper-Metal-poor Stars and the Stellar IMF at Low Metallicity. *ApJ*, 665:1361–1370.

Tumlinson, J., Venkatesan, A., and Shull, J. M. (2004). Nucleosynthesis, Reionization, and the Mass Function of the First Stars. *ApJ*, 612:602–614.

Turk, M. J., Abel, T., and O'Shea, B. (2009). The Formation of Population III Binaries from Cosmological Initial Conditions. *Sci.*, 325:601–.

Ulrich, R. K. (1976). An infall model for the T Tauri phenomenon. *ApJ*, 210:377–391.

van der Laan, H. (1962). Intense shell sources of radio emission. *MNRAS*, 124:179–+.

Vasiliev, E. O. and Shchekinov, Y. A. (2006). The influence of ultrahigh-energy cosmic rays on star formation in the early Universe. *Astron. Rep.*, 50:778–784.

Venkatesan, A. and Truran, J. W. (2003). The Ionizing Efficiency of the First Stars. *ApJ*, 594:L1–L4.

Wada, K. and Venkatesan, A. (2003). Feedback from the First Supernovae in Protogalaxies: The Fate of the Generated Metals. *ApJ*, 591:38–42.

Waxman, E. (2001). High-Energy Particles from γ-Ray Bursts. In M. Lemoine & G. Sigl, editor, *Physics and Astrophysics of Ultra-High-Energy Cosmic*

Rays, volume 576 of *Lecture Notes in Physics, Berlin Springer Verlag*, pages 122–+.

Webber, W. R. (1998). A New Estimate of the Local Interstellar Energy Density and Ionization Rate of Galactic Cosmic Cosmic Rays. *ApJ*, 506:329–334.

Whalen, D., Abel, T., and Norman, M. L. (2004). Radiation Hydrodynamic Evolution of Primordial H II Regions. *ApJ*, 610:14–22.

White, S. D. M. and Rees, M. J. (1978). Core condensation in heavy halos - A two-stage theory for galaxy formation and clustering. *MNRAS*, 183:341–358.

Widrow, L. M. (2002). Origin of galactic and extragalactic magnetic fields. *Rev. Mod. Phys.*, 74:775–823.

Wise, J. H. and Abel, T. (2008). Resolving the Formation of Protogalaxies. III. Feedback from the First Stars. *ApJ*, 685:40–56.

Wolcott-Green, J. and Haiman, Z. (2011). Suppression of HD cooling in protogalactic gas clouds by Lyman-Werner radiation. *MNRAS*, 412:2603–2616.

Wolcott-Green, J., Haiman, Z., and Bryan, G. L. (2011). Photodissociation of H2 in Protogalaxies: Modeling Self-Shielding in 3D Simulations. *MNRAS, submitted (arXiv: 1106.3523)*.

Wolff, S. C., Strom, S. E., Cunha, K., Daflon, S., Olsen, K., and Dror, D. (2008). Rotational Velocities for Early-Type Stars in the Young Large Magellanic Cloud Cluster R136: Further Study of the Relationship Between Rotation Speed and Density in Star-Forming Regions. *AJ*, 136:1049–1060.

Woosley, S. E. (1993). Gamma-ray bursts from stellar mass accretion disks around black holes. *ApJ*, 405:273–277.

Woosley, S. E. and Bloom, J. S. (2006). The Supernova Gamma-Ray Burst Connection. *ARA&A*, 44:507–556.

Woosley, S. E. and Heger, A. (2006). The Progenitor Stars of Gamma-Ray Bursts. *ApJ*, 637:914–921.

Wyithe, J. S. B. and Loeb, A. (2003). Low-Frequency Gravitational Waves from Massive Black Hole Binaries: Predictions for LISA and Pulsar Timing Arrays. *ApJ*, 590:691–706.

Xu, H., O'Shea, B. W., Collins, D. C., Norman, M. L., Li, H., and Li, S. (2008). The Biermann Battery in Cosmological MHD Simulations of Population III Star Formation. *ApJ*, 688:L57–L60.

Yamada, M. and Nishi, R. (1998). Fragmentation of a Shock-Compressed Sheet of Primordial Gas. *ApJ*, 505:148–158.

Yoon, S. and Langer, N. (2005). Evolution of rapidly rotating metal-poor massive stars towards gamma-ray bursts. *A&A*, 443:643–648.

Yoshida, N., Abel, T., Hernquist, L., and Sugiyama, N. (2003). Simulations of Early Structure Formation: Primordial Gas Clouds. *ApJ*, 592:645–663.

Yoshida, N., Omukai, K., and Hernquist, L. (2008). Protostar formation in the early Universe. *Sci.*, 321:669–671.

Yoshida, N., Omukai, K., Hernquist, L., and Abel, T. (2006). Formation of Primordial Stars in a ΛCDM Universe. *ApJ*, 652:6–25.

Zatsepin, G. T. and Kuz'min, V. A. (1966). Upper Limit of the Spectrum of Cosmic Rays. *JETPL*, 4:78–+.

Zeldovich, Y. B. (1970). Gravitational instability: An approximate theory for large density perturbations. *A&A*, 5:84–89.

Zhang, W., Woosley, S. E., and Heger, A. (2004). The Propagation and Eruption of Relativistic Jets from the Stellar Progenitors of Gamma-Ray Bursts. *ApJ*, 608:365–377.

Zinnecker, H. and Yorke, H. W. (2007). Toward Understanding Massive Star Formation. *ARA&A*, 45:481–563.

Zweibel, E. G. (2003). Cosmic-Ray History and Its Implications for Galactic Magnetic Fields. *ApJ*, 587:625–637.

Vita

Athena Ranice Stacy was born in Jonesboro, Arkansas on June 6 of 1983, the daughter of Dr. J. W. Stacy and Nan Stacy. She graduated from Jonesboro High School in 2001, and soon after moved to Texas. In May of 2005 she earned a Bachelor of Science degree in Physics from Rice University. In August of 2005 she began graduate school in the Astronomy Department of the University of Texas at Austin, and she has been studying the nature of the first stars and galaxies ever since.

Permanent address: 3009 Speedway #2
Austin, Texas 78705

This dissertation was typeset with LaTeX[†] by the author.

[†] LaTeX is a document preparation system developed by Leslie Lamport as a special version of Donald Knuth's TeX Program.